Electrical Properties of Single-Walled Carbon Nanotube Networks Produced by Langmuir-Blodgett Deposition

by

Mark Kieran Massey
St. Aidan's College

A Thesis presented for the degree of
Doctor of Philisophy

Centre for Molecular and Nanoscale Electronics
School of Engineering and Computing Sciences
Durham University
November 2013

Electrical Properties of Single-Walled Carbon Nanotube Networks Produced by Langmuir-Blodgett Deposition

M. K. Massey

Abstract

This thesis investigates the use of the Langmuir-Blodgett (LB) deposition technique as a means for building up ultra-thin networks of single-walled carbon nanotubes (SWCNTs) on various substrates. Transfer from a water subphase is successfully demonstrated for a range of SWCNTs and the electrical properties of the networks are discussed in detail. In contrast to the majority of literature on LB networks of SWCNTs, transfer is completed without the addition of surfactants to the nanotube material. However, and as expected, improved deposition is achieved when SWCNTs are functionalised (through thermal oxidation) with carboxylic acid groups, decreasing their hydrophobicity.

In-plane electrical data reveal preferential alignment of the nanotubes along the direction of dipping. Comprehensive studies of the current dependence on temperature and the field dependence of conductivity are presented for sorted metallic and semiconducting nanotubes in an attempt to reveal the dominant conduction mechanisms. For metallic nanotubes, typical metallic conductivity is observed with an increasing resistance with increasing temperature. The metallic nanotube temperature coefficient of resistance is $10^{-3}\,\mathrm{K}^{-1}$. At high electric field strengths ($>10^{6}\,\mathrm{V/m}$), conduction in semiconducting SWCNT networks is dominated by the Poole-Frenkel effect.

Transistor structures are presented with SWCNTs as the active semiconducting layer. The best device shows p-type depletion mode behaviour with an on/off ratio of around 8 and a carrier mobility of $\sim 0.3\,\mathrm{cm}^2/\mathrm{Vs}$.

Contents

List of Figures

List of Tables

Declaration

I hereby declare that the work carried out in this thesis has not been previously submitted for any degree and is not currently being submitted in candidature for any other degree.

Signed.....

M. K. Massey

Acknowledgements

I would like to express my gratitude to everyone who has helped me over the course of this project. My sincerest gratitude is extended to both of my academic supervisors: Prof. Michael C. Petty and Dr Christopher Pearson. Without their continuing guidance, support, teaching and encouragement I would not have been able to achieve so much over the past few years.

I am also extremely grateful to Dr Mark Rosamond for the hours he spent working on the submicron electrode arrays. I also thank Mark for his seemingly endless amounts of advice and stimulating discussions relating to this work.

I would also like to acknowledge all of the members of academic staff, and support staff in the School of Engineering and Computing Sciences who have in some way been involved over the course of the project, be it helping in the cleanrooms or providing advice on areas of the research. In particular I must thank Dr Christopher Pearson again for his help while performing experimental work in the cleanroom, his depth of experimental knowledge and experience is unrivalled by anyone I have ever met. I would also like to thank Dr Dagou Zeze for many useful discussions and help in writing papers.

I wish to thank all of the postgraduate students I have worked with during my time in Durham, you have helped make what has been a very challenging period of life, enjoyable at the same time. I would also like to acknowledge all past and present members of the Durham University Badminton Squad, it is safe to say that you as a club played a huge part in my time in Durham.

Finally, I would like to thank my family for supporting and encouraging me throughout my time at university. I thank my grandparents for their generosity in financially supporting me, in particular though the first year of the PhD. Special

thanks must go to my parents, Judith and David. They have always encouraged me to aim high and have made many sacrifices to allow me to succeed, I will always be indebted to them.

Chapter 1

Introduction, Aims and Vision

1.0.1 Introduction

Carbon nanotubes (CNTs) are generating enormous interest as a potential new material for applications in electronics. The unique mechanical, electrical and optical properties of carbon nanotubes offer numerous advantages over traditional semiconductor materials, particularly in the emerging field of plastic electronics where flexibility is a key property. For example, thin films of CNTs may be useful as transparent conducting electrodes or as the active layer in chemical sensors or thin film transistors. Although carbon nanotubes are seen as an attractive alternative to current electronic materials, first a means must be found to produce CNTs in the form of ultra-thin (nanometre scale) films. Such films can be deposited by direct growth methods, however solution based processing techniques are favoured. The lower temperature processes not only provide reduced energy costs, but also allow coating onto a variety of flexible (e.g. plastic) substrates [1].

The work presented here will focus on the Langmuir-Blodgett (LB) deposition technique as a simple and elegant means of building up multilayer architectures of CNTs. Carbon nanotubes are not inherently amphiphilic so do not naturally

lend themselves to LB deposition. Despite this, there are reports of successful LB deposition [2, 3, 4, 5]. Often, nanotubes are dispersed with amphiphilic polymers in organic solvents to improve dispersion [6] or are chemically modified to improve their solubility [7]. Here, the majority of work is carried out with undiluted and unmodified nanotubes with the aim of retaining the inherent electrical properties of the starting material. The optimisation of the LB process is explored in detail along with the morphology and optical properties of the CNT LB networks. For successful integration of carbon nanotubes into electronic devices, the electrical behaviour is of great interest. Single walled carbon nanotubes (SWCNTs) can either be metallic or semiconducting, with their individual electronic properties depending on the diameter and chirality of the nanotube. The conductivity in two-dimensional networks of unsorted SWCNTs (i.e. a mixture of metallic and semiconducting types) as well as sorted metallic and semiconducting SWCNT networks are analysed in detail in this work.

The thesis is divided into chapters with the following content. Chapter 2 gives an overview of carbon nanotubes including their synthesis, separation, physical properties and their current applications in electronics. Chapter 3 introduces the Langmuir-Blodgett deposition technique along with other common thin film fabrication techniques. Methods of forming thin films of carbon nanotubes including direct growth and solution based methods are discussed. The three main conduction mechanisms explored in this work are introduced in Chapter 4 as well as an overview of the literature on the electrical properties of carbon nanotube films. The operation of thin film transistors (TFTs) is also outlined to aid in the discussion of CNT FET devices later in the thesis. Chapter 5 contains all of the experimental details for this work.

The results are organised in four chapters. Chapter 6 focuses on isotherms and Langmuir-Blodgett deposition of the various materials used. In Chapter 7, the morphology and optical properties of the LB produced nanotube networks

are presented. This leads on to Chapter 8 where the networks are electrically characterised. First, the formation of contacts is explored, then the conductivity mechanisms at work in the networks are discussed. The final results chapter (Chapter 9) introduces various FET structures and discusses the initial results obtained.

Finally, Chapter 10 provides the conclusions drawn from this work and also makes suggestions for further investigations.

1.0.2 Aims and Vision

The aim of this work is to investigate the use of the Langmuir-Blodgett technique as a alternative method for creating thin networks of carbon nanotubes without the need for additional surfactant or chemical modification of the CNTs. By not introducing additional impurities into the starting material it is hoped that networks retaining the inherent electrical properties of the nanotubes can be produced. The electrical properties of the networks will be explored and by using unsorted, sorted semiconducting and sorted metallic nanotubes differences in the conduction processes will be discussed. Langmuir-Blodgett deposition will be explored as an alternative method for creating the carbon nanotube active layer in thin film transistors.

References

[1] L. Hu, D. S. Hecht, and G. Grüner, "Carbon nanotube thin films: Fabrication, properties and applications," *Chem. Rev.*, vol. 110, no. 10, pp. 5790–5844, 2010.

[2] Y. Kim, N. Minami, W. Zhu, S. Kazoui, R. Azumi, and M. Matsumoto, "Langmuir-Blodgett films of single-wall carbon nanotubes: Layer-by-layer deposition and in-plane orientation," *Jpn. J. Appl. Phys.*, vol. 42, pp. 7629–7634, 2003.

[3] G. Giancane, A. Ruland, V. Sgobba, D. Manno, A. Serra, G. M. Farinola, O. H. Omar, D. M. Guldi, and L. Valli, "Aligning single-walled carbon nanotubes by means of Langmuir-Blodgett film deposition: Optical, morphological, and photoelectrochemical studies," *Adv. Func. Mat.*, vol. 20, no. 15, pp. 2481–2488, 2010.

[4] M. K. Massey, C. Pearson, D. A. Zeze, B. Mendis, and M. C. Petty, "The electrical and optical properties of orientated Langmuir-Blodgett films of single-walled carbon nanotubes," *Carbon*, vol. 49, pp. 2424–2430, 2011.

[5] M. K. Massey, M. C. Rosamond, C. Pearson, D. A. Zeze, and M. C. Petty, "Electrical behavior of Langmuir-Blodgett networks of sorted metallic and semiconducting single-walled carbon nanotubes," *Langmuir*, vol. 28, no. 43, pp. 15385–15391, 2012.

[6] Y. Guo, N. Minami, S. Kazaoui, J. Peng, M. Yoshida, and T. Miyashita, "Multilayer LB films of single-wall carbon nanotubes," *Physica B*, vol. 323, pp. 235–236, 2002.

[7] J.-H. Lee, W.-S. Kang, B.-S. Choi, S.-W. Choi, and J.-H. Kim, "Fabrication of carbon nanotube AFM probes using the Langmuir-Blodgett technique," *Ultramicroscopy*, vol. 108, no. 10, pp. 1163 – 1167, 2008. Proceedings of the Ninth International Conference on Scanning Probe Micrososcopy, Sensors and Nanostructures.

Chapter 2

Carbon Nanotubes

2.1 Introduction

This chapter will outline the properties of carbon nanotubes and describe their potential use as a new material in electronic applications. The discussion will include their discovery, production, purification, separation and solution preparation. The basic mechanical, optical and electronic properties of CNTs will then be described. The current applications of nanotubes in devices including thin film conductors, chemical sensors and thin film transistors will be reviewed, with a focus on the latter.

2.2 Historical Background

It is widely accepted that the discovery of carbon nanotubes (CNTs) was by Sumio Iijima in 1991 [1]. Although other groups indicated discoveries as early as 1952 [2]. Iijima demonstrated an arc-discharge evaporation method for producing "graphitic carbon needles" with diameters ranging from 4 nm to 30 nm. This created a much bigger impact in the scientific community. Figure 2.1(a) shows the first electron micrographs of multi-walled CNTs produced by Iijima. Research into carbon nanotubes has increased markedly since Iijima's first observations. These are now seen as a promising alternative to current electronic materials.

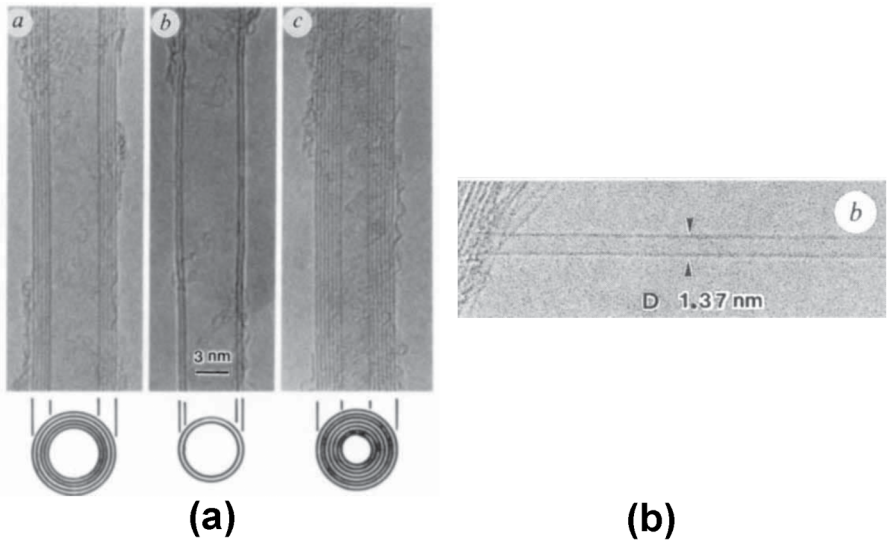

Figure 2.1: *Electron micrographs of microtubules of (a) multi-walled graphitic carbon produced by Iijima [1] and (b) single-walled carbon nanotubes [3].*

The discovery of single-walled carbon nanotubes (SWCNTs) was reported in Nature during June 1993 in two papers, one by Iijima and Ichihashi [3] and the other by Bethune et al. [4]. Figure 2.1(b) shows the first electron micrograph of a SWCNT with a diameter of 1.37 nm.

2.3 Structure

The simplest way to think of a carbon nanotube is as a single graphene sheet rolled up to form a cylinder (single-walled carbon nanotube) or multiple graphene sheets rolled up in concentric cylinders (multi-walled carbon nanotube). Examples are shown in Figure 2.2. The majority of work discussed in the following chapters refers to single-walled carbon nanotubes (SWCNTs), so this is what this section will focus on. Typical SWCNTs have a diameter of around 1.2 nm and lengths between 1 µm to 20 µm. Because of this high aspect ratio (potentially in excess of 1,000,000:1) SWCNTs are sometimes classed as one dimensional objects.

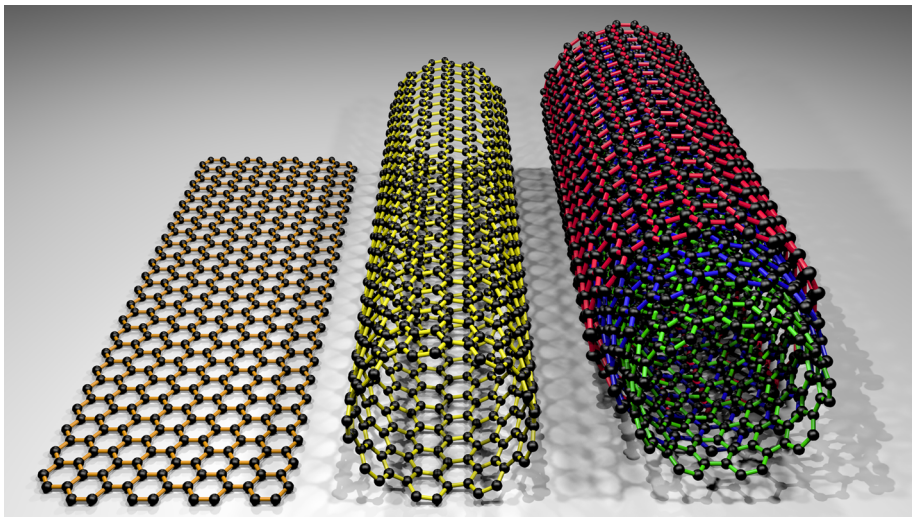

Figure 2.2: *A three dimensional representation (from left to right) of a graphene sheet, single-walled carbon nanotube and multi-walled carbon nanotube.*

The electronic properties of a SWCNT, either metallic or semiconducting, depend on the structure of the nanotube. The way the graphene sheet is wrapped to form a single-walled nanotube can be represented by a pair of indices (n,m). These integers represent the number of unit vectors along two directions in the crystal lattice of graphene. The two directions represent the zigzag nanotubes (where m = 0) and the armchair nanotubes (where n = m). Any vectors between these are classed as chiral nanotubes. All armchair nanotubes are metallic in behaviour, all other nanotubes are metallic if (2n + m) or (n - m) is a multiple of 3. Figure 2.3 shows the zigzag and

armchair vectors (red lines) and all of the possible vectors between, with metallic nanotubes highlighted in blue and semiconducting nanotubes highlighted in green. As can be seen in Figure 2.3, approximately one third of the nanotubes are metallic, with the remainder being semiconducting [5]. Because of this, all as-produced single-walled carbon nanotubes contain a mixture of both types of tubes and need to be separated if specific electronic properties are required. The exact ratio of metallic to semiconducting tubes can vary depending on the growth process and/or conditions used.

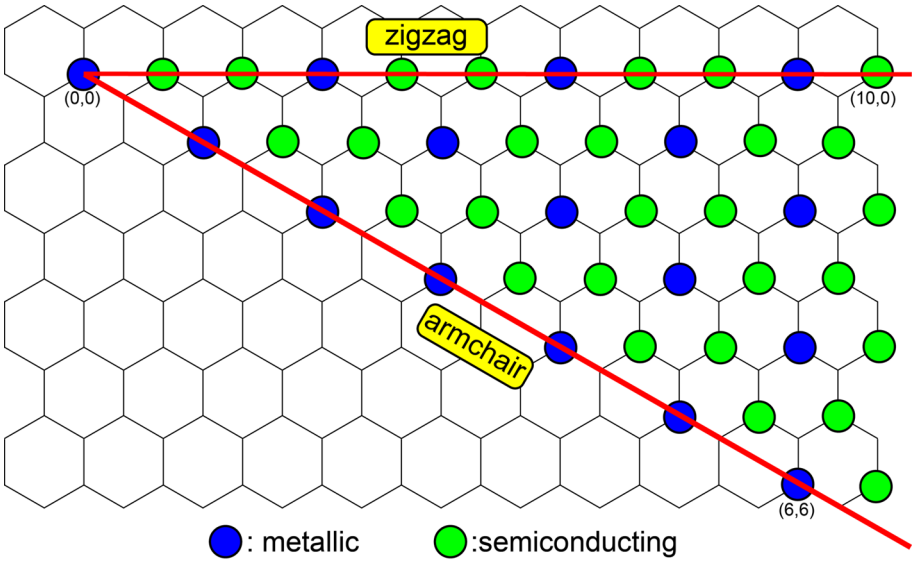

Figure 2.3: *Representation of the chiral vectors for carbon nanotubes, adapted from [5]*

2.4 Synthesis

Carbon nanotubes can be produced following three main methods: arc-discharge [4, 6, 7], laser ablation [8] and chemical vapour deposition [9, 10, 11]. Each method has benefits as well as drawbacks with regard to purity, volume, cost and speed of production. The production method will vary depending on the required application. For example, the use of nanotubes as a composite material for adding strength

requires large volumes without the need for high purity. In contrast, for electronic applications, the control on diameter, length and purity are far more important.

2.4.1 Arc Discharge

Arc discharge and laser ablation both involve the condensation of hot gaseous carbon atoms generated when solid carbon is evaporated. These were the initial methods for producing relatively large amounts of material (grams) [6, 8]. A metal catalyst is used in the arc-discharge system to grow single-walled carbon nanotubes [4]. Under optimised conditions, these processes produce nanotubes with the highest possible crystallinity due to the high temperatures involved (2000 °C to 3000 °C). A downside to these processes is the large amount of graphitic and amorphous carbon produced in parallel to the nanotubes [12]. Therefore, a cleaning process is necessary before the nanotubes can be used. The purified nanotubes are typically dispersed in solvents and then solution processed to form random networks, making reproducible device fabrication challenging.

2.4.2 Chemical Vapour Deposition

Chemical vapour deposition (CVD) involves the decomposition of a gaseous compound of carbon with metallic nanoparticles as the catalyst. These nanoparticles function as nucleation sites for the growth of carbon nanotubes and can either be introduced in the gas phase or patterned onto substrates. The resulting carbon from the decomposition is absorbed on the catalyst particle and is released in the form of a nanotube when the concentration exceeds the maximum solubility. The growth of a nanotube starts with a hemisphere of carbon atoms as an end cap, this then grows in length as a cylinder of carbon atoms. Growth temperatures for CVD are in the range of 400 °C to 1000 °C, significantly lower than that for laser ablation or arc

discharge. It is believed that CVD nanotubes have a higher density of defects due to the lower temperatures involved, compared with the arc discharge process. Despite the greater likelihood of defects, this has become the most widely utilised method for the commercial production of SWCNTs as it is easily scaled for industry [13]. A further advantage is that, under the correct conditions, no unwanted graphitic material is produced, so additional purification steps are avoided. Both SWCNTs and MWCNTs can be produced by using CVD methods, with the advantage of increased control over the morphology and structure of the nanotubes. As well as powders of tangled nanotubes, separated individual tubes can be grown on flat substrates or across trenches for use in nanoscale electronics [14, 15]. If the catalyst is patterned across the substrate, then a layer of patterned nanotubes can be grown on the surface. This has been demonstrated on a 6 inch silicon wafer with MWCNTs at 700 °C using acetylene as the source gas and a 5 nm thick patterned layer of iron as the catalyst [16]. There are several variations on the technique, including: methane CVD, HiPCO, CO CVD, alcohol CVD and PECVD (plasma-enhanced CVD) [13].

HiPCO

The high-pressure catalytic decomposition of carbon monoxide (HiPCO) process is a variation on CVD and uses high pressure CO as the carbon source. The catalysts for growth are formed in the gas phase from a volatile organometallic precursor introduced into the reactor. The first SWCNTs produced by HiPCO were by Dai et al. in 1996 [9].

Figure 2.4 shows a simplified schematic diagram of the HiPCO reactor used by Smalley's research group at Rice University [17]. This consists of a thin-walled quartz tube surrounded by heating elements inside a thick-walled outer cylinder. Carbon monoxide flows through the quartz tube, with a small amount of $Fe(CO)_5$. The products of the $Fe(CO)_5$ thermal decomposition react to produce small iron

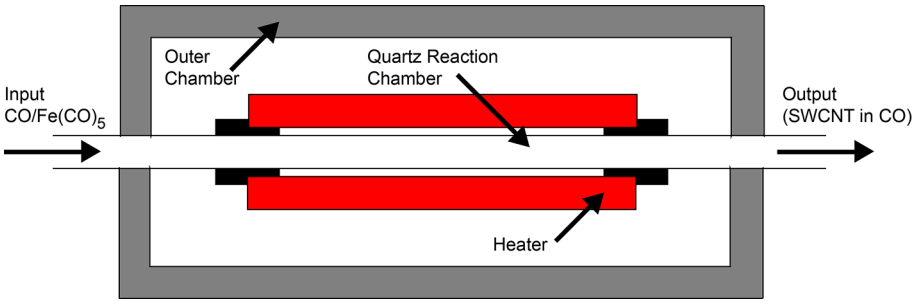

Figure 2.4: *Simplified diagram of HiPCO CNT production, adapted from [17].*

particles in the gas. These particles then act as nucleation sites for SWCNTs. Carbon is produced by CO disproportionation (Boudard reaction):

$$CO + CO \rightarrow C(s) + CO_2 \tag{2.1}$$

2.5 Carbon Nanotube Separation

The ability to separate carbon nanotubes into semiconducting and metallic types is of great importance for many applications. For example, field effect transistors with a large number of metallic nanotubes forming a conducting pathway can lead to devices with very poor characteristics [18]. To optimise the conductivity of thin film transparent conductors, the use of pure metallic nanotubes is highly desirable.

There are several reported methods of separating metallic from semiconducting nanotubes. This can either be done during growth [19, 20], during solution preparation [21], during deposition [22, 16] or as a post process step, for example by electrical annealing [23].

2.5.1 Separation during Growth

The ideal solution for the separation of nanotubes based on their electronic properties would be to manipulate directly and selectively grow a specific diameter

or chirality of nanotube. The diameter of nanotubes is reported to be controllable by varying the temperature [24], pressure [25, 26], carbon feedstock [27] and catalyst material [28, 29], and/or size [30]. Although the majority of work on selective growth focuses on the diameter of the grown nanotubes, there are some reports of semiconductor enrichment (nearly 90 % semiconducting) during CVD growth [19] and 65 $\pm$2 % metallic enrichment with pentanol as the carbon feedstock [20]. Despite these reports, a reliable method of growing nanotubes with purities similar to that obtained by sorting material, either during or before device fabrication, has proved unachievable to date.

2.5.2 Separation using Ultracentrifugation

Ultracentrifugation can be used to sort SWCNTs according to their sedimentation coefficient in a constant density medium. This coefficient depends on several parameters (including buoyant density and molecular weight), so SWCNTs sorted by conventional ultracentrifugation are not sorted by specific diameters or lengths, instead a combination of both [31]. An alternative is density gradient ultracentrifugation (DGU), in which the constant density medium is replaced by an intentionally formed density gradient in the centrifuge tube. The SWCNTs to be sorted are then added to the tube and sediment through the gradient until they reach their isopycnic points (where their density matches the density of the gradient). This allows SWCNTs to be sorted exclusively by their buoyant density (mass to volume ratio), proportional to the surface-to-volume ratio for a cylinder which is inversely proportional to the diameter. Since DGU occurs in an aqueous solution and SWCNTs are highly hydrophobic, surfactants must be used to disperse the SWCNTs. The actual buoyant density of the nanotubes will then depend on the geometry of the nanotube as well as the thickness and hydration of the surfactant coating [32]. If a surfactant is chosen that uniformly and identically encapsulates all

of the SWCNTs then the buoyant density is only a function of SWCNT diameter.

Density gradient ultracentrifugation can be used to sort carbon nanotubes beyond simple geometry. For example, if a surfactant, or combination of surfactants is chosen that encapsulates SWCNTs based on their electronic structure then the nanotubes can be sorted into semiconducting and metallic types. Using the appropriate combinations of surfactants enables tunability in the sorting of SWCNTs. The DGU approach was first used to sort SWCNT-DNA hybrids by diameter [33]. However, this had several disadvantages such as irreversible wrapping, high cost and the inability to disperse large diameter (>1.2 nm) SWCNTs. Work then focused on surfactant based encapsulation of SWCNTs for DGU [21]. Figure 2.5 shows an example of DGU, used to separate sodium cholate encapsulated SWCNTs. Visually, the separation is apparent from the formation of coloured bands indicating the fractions of different diameter SWCNTs. Bundles, aggregates and insoluble material sediment lower in the gradient. Purities approaching 99 % have been reported following the iterative application of DGU [31].

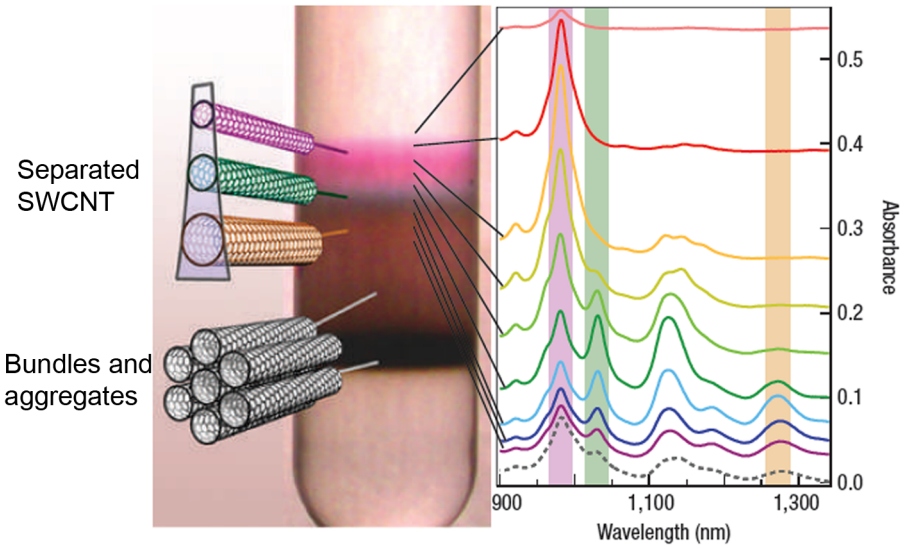

Figure 2.5: *Sodium cholate encapsulated SWCNTs separated by DGU. Visually the separation is evident from the coloured bands. The spectra indicate SWCNTs of increasing diameter. Taken from [21].*

The sorted SWCNTs used in this work were separated by DGU; the semiconducting

material was 98 % pure and the metallic 95 % pure. This purity refers to the relative semiconducting and metallic content, respectively.

2.5.3 Separation during Deposition

Carbon nanotubes can also be sorted during deposition and device fabrication. Two methods that will be discussed here are "electrophoteric separation" and "selective deposition".

Electrophoteric separation sorts SWCNTs according to their relative mobility through a gel or a solution when a direct current electric field is applied [34, 35]. A second approach is to use an alternating electric current; this process is known as dielectrophoresis. When subjected to an electric field, SWCNTs develop an induced dipole moment. The induced dipole moment allows movement and alignment of the nanotubes by designing an appropriately inhomogeneous electric field. Due to differences in the dielectric constant of metallic and semiconducting nanotubes they can be effectively sorted by electronic type [22]. Figure 2.6(a) shows a typical experimental setup used by Krupke et al. [22] and (b) shows alignment of nanotubes during their work. A drop of SWCNTs suspended in solution is placed on the microelectrode array and an AC electric field is applied. The metallic nanotubes

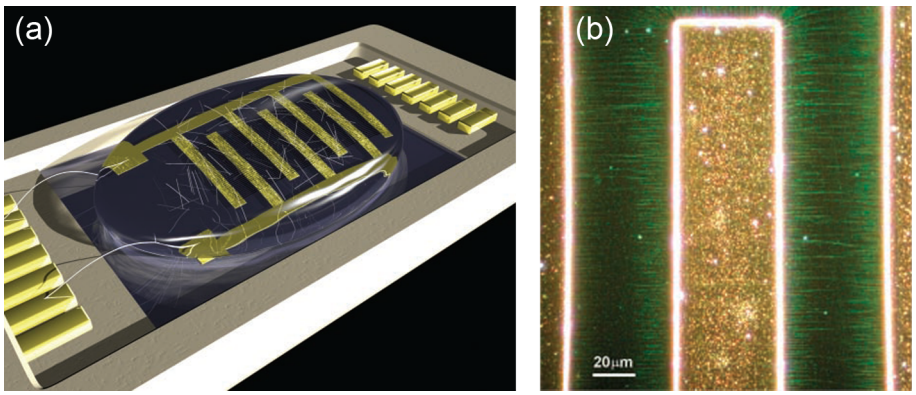

Figure 2.6: *(a) Typical microelectrode array used for dielectrophoresis (b) dark-field microscope image following dielectrophoresis, taken from [22].*

are then selectively deposited on the substrate between the electrodes. At the same time, the metallic nanotubes are aligned to the electric field. Although successful, an obvious downside to dielectrophoresis on electrode arrays is the limited throughput (for example Krupke et al. only isolated 100 pg of metallic SWCNTs).

Selective deposition from solution involves the functionalisation of a substrate with species that bind selectively to either metallic or semiconducting nanotubes. Work by Papadimitrakopoulos showed selective absorption of aminosilanes towards semiconducting SWCNTs [36]. Other work has shown that aromatic molecules (such as phenyl-terminated silane) bind selectively to metallic SWCNTs [37]. Bao et al. demonstrated that the tube density of either metallic or semiconducting nanotubes could be substantially modulated by the surface chemistry through functionalising the surface either with amine-terminated or phenyl-terminated silane [38].

2.5.4 Post Processing Step

The final method of nanotube "sorting" to be discussed is a post processing step, carried out after the nanotube network has been deposited or grown. This often involves selective destruction of those SWCNTs with undesirable properties for the chosen application, such as removing metallic nanotubes in a field effect transistor.

Selective oxidation of SWCNTs by annealing in an oxygen rich atmosphere has been shown to remove nanotubes with small diameters and high chiral angles [39, 40]. Etching of metallic SWCNTs with diameters less than 1.1 nm by a gas-phase reaction has been demonstrated with fluorine gas followed by annealing [41]. Laser irradiation in hydrogen peroxide selectively oxidises semiconducting SWCNTs [42], whereas in air metallic nanotubes are oxidised [43].

An alternative to selective destruction is controlled SWCNT breakdown with high current flow. Collins et al. successfully demonstrated the electrical annealing of

SWCNT bundles to remove metallic tubes, thus improving the characteristics of their FET devices [23].

2.6 Carbon Nanotube Properties

There are significant challenges in modelling and measuring the mechanical, electrical and optical properties of carbon nanotubes due to the nano-scale dimensions involved. These challenges include a lack of micromechanical characterisation techniques for direct measurements, limitations on specimen size, uncertainty involved with measurements made indirectly and difficult control over nanotube preparation techniques such as "bundling" during growth. There are a number of reports involving theoretical calculations, as well as experimental observations of nanotube properties. These fundamental properties will be discussed within this section.

2.6.1 Mechanical Properties

Experimental and theoretical studies have revealed that carbon nanotubes possess remarkable mechanical properties. Treacy et al. were the first to investigate the elastic modulus of individual multi-walled nanotubes (MWCNT) by measuring the amplitude of their intrinsic thermal vibrations with a transmission electron microscope (TEM). The average value of elastic modulus reported was 1.8 TPa [44]. This is very high in comparison to standard mild steel which has a Young's modulus of $\sim$200 GPa. The stiffness and strength of individual isolated MWCNTs have been measured with an atomic force microscope (AFM) by Wong et al. [45]. A value of 1.26 TPa was obtained for the elastic modulus and the average bending strength was (14.2 ± 8.0) GPa. As noted before, single-walled carbon nanotubes tend to exist in

bundles or ropes so measurement of individual nanotubes is difficult. The properties of bundles of SWCNTs have been measured with an AFM by Salvetat et al. [46], reporting elastic modulus of the order of 1 TPa and shear modulus of the order of 1 GPa. These authors also report a low intertube shear stiffness compared to MWCNT, suggesting that intertube cohesion would need to be improved if SWCNT ropes were to be used in high-performance composite materials. Tensile loading of MWCNTs and SWCNTs has been investigated by the same group, with nanotubes being attached between two opposing AFM tips and loaded under tension. Multi-walled nanotubes showed failure in the outermost tube through pulling out of the inner nanotubes. Tensile strengths of the outermost layer were calculated between 11 GPa to 63 GPa and the elastic modulus ranged from 270 GPa to 95 GPa [47]. The group also report a similar investigation of SWCNT ropes where they make the assumption that only the outermost tubes in the rope carried the load during the experiment [48]. This gave tensile strengths of 13 GPa to 52 GPa and average elastic moduli of 320 GPa to 1470 GPa. Lower values of tensile strength and modulus of 3.6 GPa and 450 GPa, respectively were reported by Xie et al. [49]. They suggested that the lower values of strength and stiffness could be the result of defects introduced during growth of the CVD nanotubes.

2.6.2 Optical Properties

The optical properties of carbon nanotubes can refer to processes such as absorption, photoluminescence and Raman scattering. Experimentally obtained optical data can reveal much information about the structure of nanotubes, including the diameter, chirality and electronic type.

Optical absorption spectroscopy measures the absorption of electromagnetic radiation in a sample. Energy is absorbed due to the interaction of radiation with the sample and is a function of the wavelength of the radiation. The intensity of

light passing through an absorbing medium decreases exponentially according to the Beer-Lambert law,

$$I(l) = I_0 e^{(-\alpha L c)} \tag{2.2}$$

where I_0 is the intensity of the incident light, α is the absorption coefficient, L is the optical path length and c is the concentration of an absorbing species in the material. If the ratio of the transmitted intensity is measured in relation to the incident intensity then the absorbance at a given wavelength is given by,

$$A = -ln\frac{I}{I_0} \tag{2.3}$$

Transitions between the valence and conduction bands dominate the optical response of SWCNTs. Momentum conservation only allows transition pairs of singularities

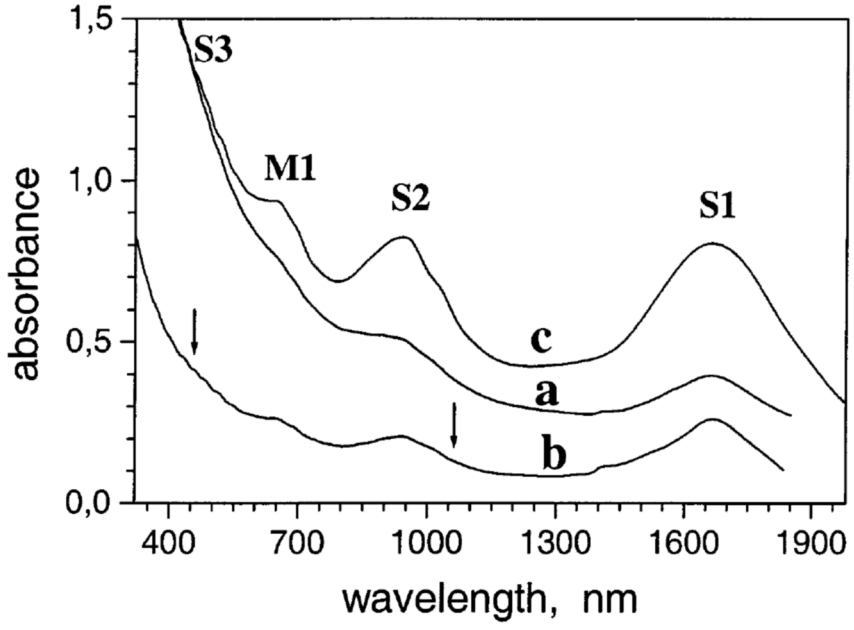

Figure 2.7: *Optical absorption spectra for SWCNTs. (a) and (b) show the SWCNTs in solution before and after centrifugation, respectively; (c) is for a free-standing nanotube film, taken from [50].*

that are symmetrically placed with respect to the Fermi level, these transitions are labelled E_{ii} (i = 1,2,3...). This means light is absorbed when it is in resonance with the E_{ii} values for the (n, m) nanotubes in a sample [51]. The optical absorption spectra show broad features due to the mixture of nanotubes with many different (n, m) species. Figure 2.7 shows a set of typical absorption spectra for bulk SWCNTs. There are three broad absorption peaks labelled S1 and S2 for the first and second semiconducting transitions (E_{11}^S and E_{22}^S) and M1 for the first metallic transition (E_{11}^M). The absorption spectra can be used to evaluate the average diameter in a sample, the energy of the optical transition in a SWCNT is inversely proportional to the diameter.

2.6.3 Electronic Properties

As discussed in Section 2.3, the wrapping angle (or chirality) has a strong influence on the specific electronic properties of a carbon nanotube. The diameter of the nanotube also has a strong impact on the electrical properties. The band gap of a semiconducting nanotube is inversely proportional to the diameter and is approximately 0.8 eV for a nanotube with diameter of 1 nm [52]. This is comparable to that of silicon, making SWCNTs of interest for transistor and diode applications [53]. Single-walled nanotubes typically have diameters between 0.7 nm to 2 nm, although diameters as great as 5 nm and as small as 0.4 nm have been observed [52]. The curvature of nanotubes (especially at small diameters) can lead to distortion of the bonds, so even a nanotube satisfying (2n + m) or (n - m) being a multiple of 3 can result in a small band gap metallic CNT if the curvature is great enough [53]. This effect is only important at very small diameters, for example a semimetallic nanotube with a diameter of ∼1 nm would have a band gap of just 40 meV (compared with 0.8 eV for a true semiconducting nanotube). Only nanotubes with n = m can be considered true metallic CNTs due to their special symmetry [54]. Metallic

SWCNTs have been shown to exhibit ballistic conductivity over distances of several micrometers depending on the tube quality. Their very high reported conductance shows promise for use as interconnects in traditional silicon and also molecular based electronics [54].

Oxygen and Water Doping of Carbon Nanotubes

Carbon nanotubes have excellent molecule adsorption properties due to their size, large surface area and hollow nature. This makes them ideal candidates for use in sensing applications, with exposure to air or oxygen being reported to dramatically influence the nanotubes' electrical resistance [55]. Exposure to water is also reported to affect the electrical properties of nanotube films, in particular an increase in resistance of approximately 4 % is noted for films exposed to water vapours [56]. Many nanotube suspensions involve dispersal in aqueous suspensions using surfactants, the sonication process can cause inadvertent doping due to the in-situ formation of molecular oxygen [57]. Although this work does not involve the suspension of nanotubes in aqueous solution, the effects of doping should still be considered due to the nature of the subphase used for LB deposition (water). It should be noted that even with the annealing step following deposition and using a vacuum environment for electrical measurements it is possible that some residual water/oxygen could influence the resistance.

2.7 Carbon Nanotube Devices

Prominent applications involving thin films of CNTs are as transparent conducting electrodes, as the active layer in field effect transistors and in sensing applications [58]. This section will explore these three main applications and the progress that

has been made in integrating CNTs successfully into electronic devices. It will also outline the areas which need improvement and how this work is related to advances in device fabrication.

2.7.1 Transparent Conductors

Transparent, conducting electrodes are essential for many optoelectronic device applications such as: solar cells, organic light emitting diodes, flat panel displays and touch panels [58]. Significant research has been undertaken on transparent conducting oxides (TCOs) to perfect these materials with high conductivity and high optical transparency. Indium tin oxide (ITO) is one of the dominant materials used in the market. However, from a manufacturing point of view it does have limitations. The cost of indium, a rare earth element, has fluctuated dramatically over the past few years. Therefore, alternatives to indium based conductors are highly sought after. Production methods for TCOs are also costly, since high vacuum equipment and high temperatures are usually involved. Due to the high temperature, deposition onto flexible plastic substrates is difficult, so incorporation into flexible electronics is problematic.

Transparent and conducting thin films can be built from conducting polymers, and offer several fabrication advantages over traditional TCOs. The main advantage is the ability to use solution based coating techniques so a range of plastic substrates can be used. One of the most successful materials is poly(3,4-ethylenedioxythiophene) poly(styrenesulfonate) (PEDOT:PSS). Various types of devices, including OLEDs, OFETs and photovoltaics, have been fabricated with PEDOT:PSS as the electrodes [59]. Unfortunately, the sheet resistance of PEDOT:PSS ($200\,\Omega/\square$ at 80 % transmittance) falls well above that of traditional ITO films (typically $18\,\Omega/\square$ at 95 % transmittance) [58].

Carbon nanotubes offer advantages over traditional TCOs and conducting polymers.

Not only can CNTs be deposited by solution processing but they also offer enhanced electronic properties when compared with conducting polymers. Sheet resistances as low as 30 Ω/□ at 70 % transmittance [60] have been reported. Figure 2.8 shows an 80 nm thick CNT film on a sapphire substrate.

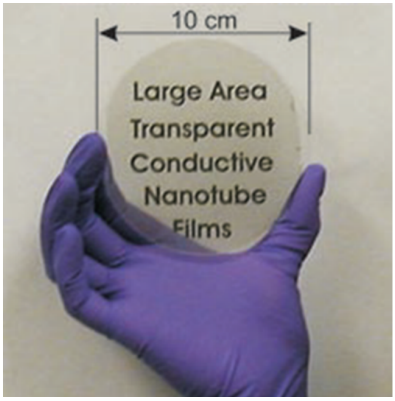

Figure 2.8: *80 nm thick CNT film on a sapphire substrate, taken from [60].*

Carbon nanotube films exhibit good mechanical strength along with relatively easy patterning, allowing incorporation into flexible electronic devices [61]. Studies of CNT networks (both theoretical and experimental) have shown the work function to be in the range 4.5 eV to 5.2 eV [62, 63]. These high work functions meet the requirements for anodes in several types of photonic devices such as organic light-emitting diodes and solar cells [58].

2.7.2 Field Effect Transistors

Carbon nanotube based field effect transistors (FETs) operate following the same basic principles as silicon based transistors. By applying an electric field to the gate the number of charge carriers can be modulated in the CNT network, thus dramatically increasing the conductivity through the channel. Devices can either be "bottom gated" (Figure 2.9(a)) where the CNT network is deposited on top of the dielectric (typically SiO_2) or "top gated" (Figure 2.9(b)) with organic dielectrics, such as PMMA. Top gating has the advantage of increasing the coupling between

the gate and conducting channel, thus increasing the gate effect. However, if the surface of the CNT film is too rough then short circuits occur between the source or drain and the gate.

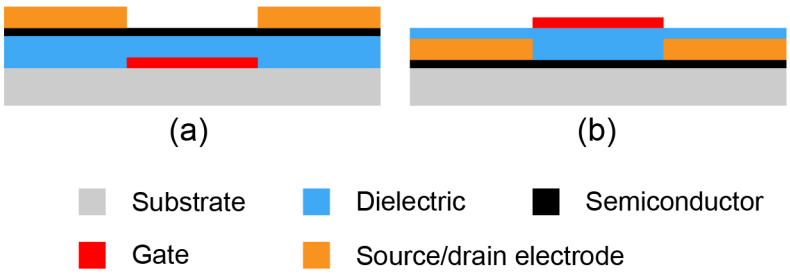

Figure 2.9: *Electrode layout for (a) bottom and (b) top gated thin film transistors.*

The density of CNT networks plays an important role in determining the device properties, particularly the on/off ratio, due to possible shorting by metallic nanotubes. For example, transistors made with unsorted nanotubes (typically containing 1/3 metallic and 2/3 semiconducting nanotubes) can often display metallic behaviour instead of the desired semiconducting behaviour [18] due to shorting of the channel by metallic nanotube conducting paths between the source/drain electrodes. The threshold voltage and on/off ratio of multiple tube CNTFETs can be tuned by selectively "burning" nanotubes with an electrical annealing step [64]. Each nanotube in the CNTFET will have a different threshold voltage (V_T), which provides a distribution of threshold voltages with all nanotubes contributing to the overall threshold voltage. To set a desired V_T for the CNTFET, the CNTs with a V_T more positive than the desired V_T need to be electrically burnt. The gate voltage is set to the desired V_T, turning off and protecting all CNTs with a more negative V_T. Nanotubes with V_T more positive than the gate voltage remain on and susceptible to electrical breakdown when the source/drain voltage is swept to sufficiently high voltages. A similar process can be applied to improve the on/off ratio by selectively burning off metallic and high leakage semiconducting nanotubes [64]. Another method to limit the conducting pathways

formed by metallic nanotubes in mixed CNT films is discussed by Rogers at al. [65]. Here, fine lines were cut into the networks along the direction of transport with widths designed to reduce the probability of metallic pathways without reducing the effective mobility of the network.

An alternative to post processing methods is to sort the carbon nanotubes before or during device fabrication. Methods of CNT separation are discussed in more detail in Section 2.5. Bao et al. have reported TFTs with an average on/off ratio greater than 10^5 by a selective deposition process. Here amine terminated silane is used to treat the substrate, causing semiconducting nanotubes to show greater adhesion during spin coating [38]. Zhou et al. report wafer-scale fabrication of CNTFETs from sorted semiconducting nanotubes with a high yield (>98 %) and on/off ratios of $>10^4$ were achieved [66].

Table 2.1 gives an overview of reported nanotube based thin film transistors over the last few years. Important fabrication details are highlighted, such as the CNT material and deposition method, the electrode material and dielectric used and the dimensions of the active channel. The semiconductor behaviour as well as three key electrical characteristics of the devices are presented: on/off ratio, threshold voltage and mobility.

Mobilities as high as $10^6\,\mathrm{cm}^2/\mathrm{Vs}$ have been reported for individual tube/individual bundle devices, with slightly lower values of up to $10^5\,\mathrm{cm}^2/\mathrm{Vs}$ for random network based devices. The majority of reported devices show p-type semiconducting behaviour, with n-type behaviour only being observed in the cases where the nanotubes have been doped, for example with potassium. All devices use source drain electrodes fabricated from either gold, titanium or palladium as they are known to produce reliable Ohmic contacts to carbon nanotubes. The channel dimensions vary greatly, from 300 nm to 100 µm depending on the type of network being exploited (i.e. either individual tubes or random networks).

Author/Date	Nanotube Material	Source/ drain	Dielectric	P/N-type Behaviour	Width/ Length Ratio	On/Off Ratio	Mobility	Threshold Voltage	Notes	Ref.
Wang et al. (2010)	Spray coated network containing a mixture of electronic types	Gold	70 nm TiO_x	P-type	2 mm/ 100 µm	500	6.7 cm^2/Vs	−0.88 V	The use of TiO_x dielectric may be influencing the results, no data for the structure without SWCNT are shown.	[67]
Unalan et al. (2006)	Filtration formed network consisting of a mixture of electronic types	Gold	100 nm SiO_2	P-type	0.1 mm / 20 µm	-	0.03 cm^2/Vs	-	Study on the percolation effects in SWCNT transistors.	[68]
Radosavljevic et al. (2004)	-	Titanium	5 nm SiO_2	N-type after potassium doping	- / 300 nm	-	-	−1.3 V to 0.5 V	Demonstrates doping of nanotubes to form n-type devices.	[69]
Chen et al. (2011)	Individual tube drop dispensed from organic solution, semiconducting devices selected.	Gold	250 nm SiO_2	P-type	- / <500 nm	-	-	-	Self assembly used to connect just one SWCNT to the source/ drain improving device performance.	[70]
Wang et al. (2010)	Spin coated from solution with low concentration so individual nanotubes on the device	Gold	300 nm SiO_2	P-type	- / 2.72 µm	10^6	3456 cm^2/Vs	-	Although good results, only 8 of 50 devices showed semiconducting behaviour.	[18]

continued . . .

. . . continued

Author/Date	Nanotube Material	Source/ drain	Dielectric	P/N-type Behaviour	Width/ Length Ratio	On/Off Ratio	Mobility	Threshold Voltage	Notes	Ref.
Lin et al. (2009)	CVD grown horizontally aligned multi-tube bundles of mixed electronic type.	Palladium	50 nm SiO_2	P-type	- / 2 µm	5×10^3 – 5×10^5	-	2.4 V - 3.6 V	Electrical "burning" of tubes used to improve the on/off ratio	[64]
Wang et al. (2009)	Self assembly of 95% pure semiconducting nanotubes to form a network	Palladium	50 nm SiO_2	P-type	- / 4 µm - 10 µm	$<10 \times 10^4$	52 cm^2/Vs	∼4 V	Functionalised surface during self assembly attracts nanotubes forming very reliable, high performance FET devices.	[66]
Le Mieux et al. (2008)	Spin coated network on functionalised substrates from mixed nanotube solutions	Gold	300 nm SiO_2	P-type	- / 2 µm	9×10^5	6 cm^2/Vs	-	Amine terminated substrates showed preferential adhesion of semiconducting nanotubes, phenyl terminated favoured metallic.	[38]
Artukovic et al. (2005)	Spray coated network of mixed nanotubes.	Gold	1.5 µm Parylene N	P-type	- / -	100	1 cm^2/Vs	-	Gate made from a dense network of CNTs.	[71]
Chen et al. (2006)	Two overlapping bundles of carbon nanotubes for interchangeable gate and source/drain.	Titanium	100 nm Si_3N_4	P-type and N-type	- / <50 nm	1000	-	-	Two tier device with top/bottom CNT bundle behaving in a P-type/N-type manner.	[72]

continued . . .

. . . continued

Author/Date	**Nanotube Material**	**Source/ drain**	**Dielectric**	**P/N-type Behaviour**	**Width/ Length Ratio**	**On/Off Ratio**	**Mobility**	**Threshold Voltage**	**Notes**	**Ref.**
Han et al. (2010)	Aligned CNT arrays transferred as single or multi CNT channels.	Palladium	4.4 nm HfO_2	Dependant on doping	- / 230 nm	10^6	-	0.6 V	Wafer scale (8 inch) production of high quality transistors.	[73]
Mizutani et al. (2010)	Plasma enhanced CVD of networks with preferential growth of semiconducting nanotubes	Gold	SiO_2/ HfO_2	P-type	- / 10 µm	10^5	6 cm^2/Vs	-	Working 4-bit decoder with 88 CNT FETs	[74]

Table 2.1: *A review of the key properties of several carbon nanotube thin film transistors reported in the literature.*

2.7.3 Chemical Sensors

There is significant interest in using nanoscale materials for sensing applications. In particular, individual carbon nanotubes could be exploited in light, chemical and biological sensing applications. A major advantage of nanomaterial based sensors is their small size and high sensitivity due to the large surface area. They also can be used for electronic sensing, rather than optical, which makes signal processing easier to perform. The diameter of SWCNTs is similar to the diameter of DNA (∼1 nm) and 10 times smaller than an average protein molecule. Figure 2.10 shows a comparison between the size of various electronic technologies in relation to biological species.

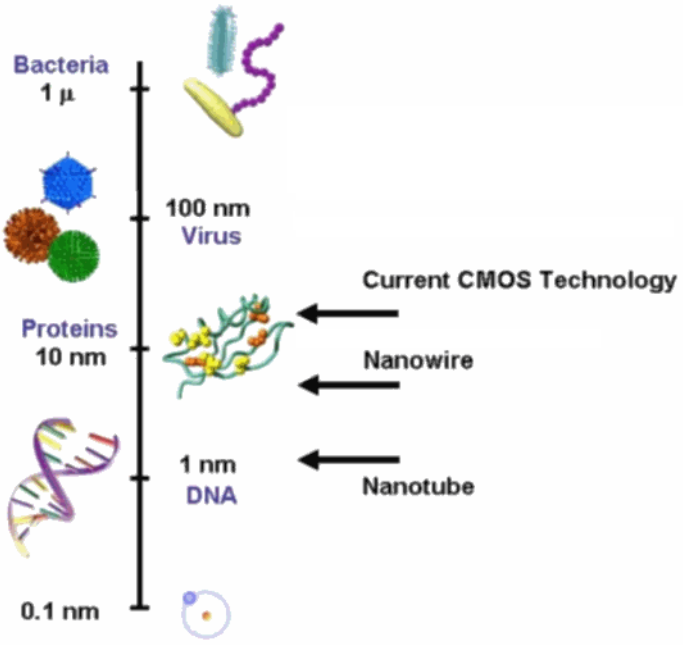

Figure 2.10: *Comparison of electronic technologies and the size of biological species, taken from [75].*

To achieve good sensitivity, the size of the detector in relation to the target is important when designing sensors. SWCNTs not only offer very small absorption sites (comparable to that of many biological cells) but they also offer high sensitivity as the carbon atoms at the surface can all act as such sites [58]. Many processes, particularly biological ones, involve electrostatic interactions and charge transfer. These can be directly monitored using CNTs, simplifying the processing of data.

There are many reports of gas sensing using carbon nanotubes. An early publication by Dai et al. reported a significant change in resistance of individual semiconducting SWCNTs when exposed to NO_2 or NH_3 [76]. The authors reported fast responses and a substantially higher sensitivity than that of existing solid state sensors at room temperature. Doping and functionalisation of the nanotubes can improve sensitivity and allow a wide range of gases to be detected [77].

2.8 Conclusions

This chapter has introduced single-walled carbon nanotubes as cylinders of rolled up graphene sheets. The electronic type of the nanotube has been shown to depend on the diameter and wrapping angle (chirality) of the graphene sheet. It is possible to have metallic and semiconducting nanotubes, with as produced nanotubes theoretically containing approximately one third metallic and two thirds semiconducting nanotubes. Two methods of carbon nanotube synthesis were introduced: arc discharge and chemical vapour deposition, with advantages and disadvantages noted for both methods. The separation of carbon nanotubes is important for obtaining optimum electronic properties in devices. Some selectivity in the growth has been demonstrated, however post-growth separation is favoured with greater purities of either semiconducting or metallic nanotubes reported. Density gradient ultracentrifugation has produced very high purities of sorted SWCNTs (up to 99 % semiconducting). Post processing techniques are also investigated, including selective destruction and controlled breakdown using high current flow. These methods yield some good results but are less favoured for commercialisation. The remarkable mechanical, optical and electronic properties of carbon nanotubes are briefly described. Mechanically, nanotubes have higher tensile strengths than steel and electrically exhibit greater conductivity than most metals. The band gap of a semiconducting nanotube is dependant on the nanotube diameter, around 0.8 eV for a typical tube, comparable to that of silicon. Carbon nanotubes have shown promise as an alternative material in many electronic devices. Transparent conductors showing sheet resistances as low as $30\,\Omega/\square$ at 70 % transmittance have been reported. Field effect transistors have been produced with on/off ratios up to 10^6 Chemical sensing devices with carbon nanotubes have also been demonstrated.

References

[1] S. Iijima, "Helical microtubules of graphitic carbon," *Nature*, vol. 354, pp. 56–58, 1991.

[2] M. Monthioux and V. L. Kuznetsov, "Who should be given the credit for the discovery of carbon nanotubes?," *Carbon*, vol. 44, pp. 1621–1623, 2006.

[3] S. Iijima and T. Ichihashi, "Single-shell carbon nanotubes of 1 nm diameter," *Nature*, vol. 363, pp. 603–605, 1993.

[4] D. S. Bethune, C. H. Kiang, M. S. D. Vries, G. Gorman, R. Savoy, J. Vazquez, and R. Beyers, "Cobalt-catalysed growth of carbon nanotubes with single-atomic-layer walls," *Nature*, vol. 363, pp. 605–607, 1993.

[5] R. Saito, G. Dresselhaus, and M. S. Dresselhaus, *Physical properties of carbon nanotubes*. Imperial College Press, 1998.

[6] T. W. Ebbesen and P. M. Ajayan, "Large scale synthesis of carbon nanotubes," *Nature*, vol. 358, pp. 220–222, 1992.

[7] C. Journet, W. K. Maser, P. Bernier, A. Loiseau, M. L. de la Chapelle, S. Lefrant, P. Deniard, R. Lee, and J. E. Fischer, "Large-scale production of single-walled carbon nanotubes by the electric-arc technique," *Nature*, vol. 388, pp. 756–758, 1997.

[8] A. Thess, R. Lee, P. Nikolaev, H. Dai, P. Petit, J. Robert, C. Xu, Y. H. Lee, S. G. Kim, A. G. Rinzler, D. T. Colbert, G. E. Scuseria, D. Tomanek, J. E. Fischer, and R. E. Smalley, "Crystalline ropes of metallic carbon nanotubes," *Science*, vol. 273, pp. 483–487, 1996.

[9] H. Dai, A. G. Rinzler, P. Nikolaev, A. Thess, D. T. Colbert, and R. E. Smalley, "Single-wall nanotubes produced by metal-catalyzed disproportionation of carbon monoxide," *Chemical Physics Letters*, vol. 260, no. 34, pp. 471 – 475, 1996.

[10] J. H. Hafner, M. J. Bronikowski, B. R. Azamian, P. Nikolaev, A. G. Rinzler, D. T. Colbert, K. A. Smith, and R. E. Smalley, "Catalytic growth of single-wall carbon nanotubes from metal particles," *Chemical Physics Letters*, vol. 296, no. 12, pp. 195 – 202, 1998.

[11] A. M. Cassell, J. A. Raymakers, J. Kong, and H. Dai, "Large scale CVD synthesis of single-walled carbon nanotubes," *J. Phys. Chem. B*, vol. 103, pp. 6484–6492, 1999.

[12] H. Dai, "Carbon nanotubes: Synthesis, integration and properties," *Acc. Chem. Res.*, vol. 35, pp. 1035–1044, 2002.

[13] E. Joselevich, H. Dai, J. Liu, K. Hata, and A. H. Windle, "Carbon nanotube synthesis and organization," in *Carbon Nanotubes*, vol. 111 of *Topics in Applied Physics*, pp. 101–164, Springer Berlin Heidelberg, 2008.

[14] J. Kong, H. T. Soh, A. M. Cassell, C. F. Quate, and H. Dai, "Synthesis of individual single-walled carbon nanotubes on patterned silicon wafers," *Nature*, vol. 395, pp. 878–881, 1998.

[15] H. Dai, J. Kong, C. Zhou, N. Franklin, T. Tombler, A. Cassell, S. Fan, and M. Chapline, "Controlled chemical routes to nanotube architectures, physics, and devices," *The Journal of Physical Chemistry B*, vol. 103, no. 51, pp. 11246–11255, 1999.

[16] G. S. Duesberg, A. P. Graham, F. Kreupl, M. Liebau, R. Seidel, E. Unger, and W. Hoenlein, "Ways towards the scaleable integration of carbon nanotubes into silicon based technology," *Diamond and Rel. Mater.*, vol. 13, pp. 354–361, 2004.

[17] M. J. Bronikowski, P. A. Willis, D. T. Colbert, K. A. Smith, and R. E. Smalley, "Gas-phase production of carbon single-walled nanotubes from carbon monoxide via the HiPCO process: a parametric study," vol. 19, pp. 1800–1805, AVS, 2001.

[18] H. Wang, J. Luo, A. Robertson, Y. Ito, W. Yan, V. Lang, M. Zaka, F. Schäffel, M. H. Rümmeli, G. A. D. Briggs, and J. H. Warner, "High-performance field effect transistors from solution processed carbon nanotubes," *ACS Nano.*, vol. 4, no. 11, pp. 6659–6664, 2010.

[19] Y. Li, D. Mann, M. Rolandi, W. Kim, A. Ural, S. Hung, A. Javey, J. Cao, D. Wang, E. Yenilmez, Q. Wang, J. F. Gibbons, Y. Nishi, and H. Dai, "Preferential growth of semiconducting single-walled carbon nanotubes by a plasma enhanced CVD method," *Nano Lett.*, vol. 4, no. 2, pp. 317–321, 2004.

[20] Y. Wang, Y. Liu, X. Li, L. Cao, D. Wei, H. Zhang, D. Shi, G. Yu, H. Kajiura, and Y. Li, "Direct enrichment of metallic single-walled carbon nanotubes induced by the different molecular composition of monohydroxy alcohol homologues," *Small*, vol. 3, pp. 1486–1490, 2007.

[21] M. S. Arnold, A. A. Green, J. F. Hulvat, S. I. Stupp, and M. C. Hersam, "Sorting carbon nanotubes by electronic structure using density differentiation," *Nature Nanotech.*, vol. 1, pp. 60–65, 2006.

[22] R. Krupke, F. Hennrich, and H. V. Löhneysen, "Separation of metallic from semiconducting single-walled carbon nanotubes," *Science*, vol. 301, pp. 344–347, 2010.

[23] P. G. Collins, M. S. Arnold, and P. Avouris, "Engineering carbon nanotubes and nanotube circuits using electrical breakdown," *Science*, vol. 292, pp. 706–709, 2001.

[24] S. Bandow and S. Asaka, "Effect of the growth temperature on the diameter distribution and chirality of single-wall carbon nanotubes," *Phys. Rev. Lett.*, vol. 80, no. 17, pp. 3779–3782, 1998.

[25] T. Hiraoka, S. Bandow, H. Shinohara, and S. Iijima, "Control on the diameter of single-walled carbon nanotubes by changing the pressure in floating catalyst CVD," *Carbon*, vol. 44, pp. 1853–1859, 2006.

[26] B. Wang, L. Wei, L. Yao, L.-J. Li, Y. Yang, and Y. Chen, "Pressure-induced single-walled carbon nanotube (n,m) selectivity on Co - Mo catalysts," *J. Phys. Chem. C*, vol. 111, pp. 14612–14616, 2007.

[27] B. Wang, C. H. P. Poa, L. Wei, L.-J. Li, Y. Yang, and Y. Chen, "(n,m) selectivity of single-walled carbon nanotubes by different carbon precursors on Co -Mo catalysts," *J. Am. Chem. Soc.*, vol. 129, pp. 9014–9019, 2007.

[28] X. Li, X. Tu, S. Zaric, K. Welsher, W. S. Seo, W. Zhao, and H. Dai, "Selective synthesis combined with chemical separation of single-walled carbon nanotubes for chirality selection," *J. Am. Chem. Soc.*, vol. 129, pp. 15770–15771, 2007.

[29] S. M. Bachilo, L. Balzano, J. E. Herrera, F. Pompeo, D. E. Resasco, and R. B. Weisman, "Narrow (n,m)-distribution of single-walled carbon nanotubes grown using a solid support catalyst," *J. Am. Chem. Soc.*, vol. 125, pp. 11186–11187, 2003.

[30] S. B. Sinnot, R. Andrews, D. Qian, A. M. Rao, Z. Mao, E. C. Dickey, and F. Derbyshire, "Model of carbon nanotube growth through chemical vapour deposition," *Chem. Phys. Lett.*, vol. 315, pp. 25–30, 1999.

[31] M. C. Hersam, "Progress towards monodisperse single-walled carbon nanotubes," *Nature Nanotech.*, vol. 3, pp. 387–394, 2008.

[32] A. A. Green and M. C. Hersam, "Ultracentrifugation of single-walled nanotubes," *Mater. Today*, vol. 10, no. 12, pp. 59–60, 2007.

[33] M. S. Arnold, S. L. Stupp, and M. C. Hersam, "Enrichment of single-walled carbon nanotubes by diameter in density gradients," *Nano Lett.*, vol. 5, no. 4, pp. 713–718, 2005.

[34] D. A. Heller, R. M. Mayrhofer, S. Baik, Y. V. Grinkova, M. L. Ushery, and M. S. Strano, "Concomitant length and diameter separation of single-walled carbon nanotubes," *J. Am. Chem. Soc.*, vol. 126, pp. 14567–14573, 2004.

[35] A. A. Vetcher, S. Srinivasan, I. A. Vetcher, S. M. Abramov, M. Kozlov, R. H. Baughman, and S. D. Levene, "Fractionation of SWNT/nucleic acid complexes by agarose gel electrophoresis," *Nanotechnology*, vol. 17, no. 16, p. 4263, 2006.

[36] D. Chattopadhyay, I. Galeska, and F. Papadimitrakopoulos, "A route for bulk separation of semiconducting from metallic single-wall carbon nanotubes," *J. Am. Chem. Soc.*, vol. 125, no. 11, pp. 3370–3375, 2003.

[37] A. Nish, J.-Y. Hwang, J. Doig, and R. J. Nicholas, "Highly selective dispersion of single-walled carbon nanotubes using aromatic polymers," *Nat. Nanotechnol.*, vol. 2, pp. 640–646, 2007.

[38] M. C. LeMieux, M. Roberts, S. Barman, Y. W. Jin, J. M. Kim, and Z. Bao, "Self-sorted, aligned nanotube networks for thin-film transistors," *Science*, vol. 321, pp. 101–104, 2008.

[39] S. Nagasawa, M. Yudasaka, K. Hirahara, T. Ichihashi, and S. Iijima, "Effect of oxidation on single-wall carbon nanotubes," *Chemical Physics Letters*, vol. 328, no. 46, pp. 374 – 380, 2000.

[40] Y. Miyata, T. Kawai, Y. Miyamoto, K. Yanagi, Y. Maniwa, and H. Kataura, "Chirality-dependent combustion of single-walled carbon nanotubes," *The Journal of Physical Chemistry C*, vol. 111, no. 27, pp. 9671–9677, 2007.

[41] C.-M. Yang, K. H. An, J. S. Park, K. A. Park, S. C. Lim, S.-H. Cho, Y. S. Lee, W. Park, C. Y. Park, and Y. H. Lee, "Preferential etching of metallic single-walled carbon nanotubes with small diameter by fluorine gas," *Phys. Rev. B*, vol. 73, p. 075419, Feb 2006.

[42] M. Yudasaka, M. Zhang, and S. Iijima, "Diameter-selective removal of single-wall carbon nanotubes through light-assisted oxidation," *Chemical Physics Letters*, vol. 374, no. 12, pp. 132 – 136, 2003.

[43] Y. Zhang, Y. Zhang, X. Xian, J. Zhang, and Z. Liu, "Sorting out semiconducting single-walled carbon nanotube arrays by preferential destruction of metallic tubes using xenon-lamp irradiation," *The Journal of Physical Chemistry C*, vol. 112, no. 10, pp. 3849–3856, 2008.

[44] M. M. J. Treacy, T. W. Ebbesen, and J. M. Gibson, "Exceptionally high Young's modulus observed for individual carbon nanotubes," *Nature*, vol. 381, pp. 678–680, 1996.

[45] E. W. Wong, P. E. Sheehan, and C. M. Lieber, "Nanobeam mechanics: Elasticity, strength and toughness of nanorods and nanotubes," *Science*, vol. 277, pp. 1971–1975, 1999.

[46] J.-P. Salvetat, G. A. D. Briggs, J.-M. Bonard, R. R. Basca, A. J. Kulik, T. Stöckli, N. A. Burnham, and L. Forró, "Elastic and shear moduli of single-walled carbon nanotube ropes," *Phys. Rev. Lett.*, vol. 82, no. 5, pp. 944–947, 1999.

[47] M.-F. Yu, O. Lourie, M. J. Dyer, K. Moloni, T. F. Kelly, and R. S. Ruoff, "Strength and breaking mechanism of multiwalled carbon nanotubes under tensile load," *Science*, vol. 287, no. 5453, pp. 637–640, 2000.

[48] M.-F. Yu, B. S. Files, S. Arepalli, and R. S. Ruoff, "Tensile loading of ropes of single wall carbon nanotubes and their mechanical properties," *Phys. Rev. Lett.*, vol. 84, pp. 5552–5555, Jun 2000.

[49] Y. Xie, J. Lu, P. Yan, X. Jiang, and Y. Qian, "A safe low temperature route to nanocrystalline transition metal arsenides," *Chemistry Letters*, vol. 29, no. 2, pp. 114–115, 2000.

[50] S. Lebedkin, F. Hennrich, T. Skipa, and M. M. Kappes, "Near-infrared photoluminescence of single-walled carbon nanotubes prepared by the laser vaporization method," *J. Phys. Chem. B*, vol. 107, pp. 1949–1956, 2003.

[51] Y. Tian, *Optical properties of single-walled carbon nanotubes and nanobuds.* PhD thesis, Aalto University, 6 2012.

[52] A. P. Graham, G. S. Duesberg, W. Hoenlein, F. Kreupl, M. Liebau, R. Martin, B. Rajasekharan, W. Pamler, R. Seidel, W. Steinhoegl, and E. Unger, "How do carbon nanotubes fit into the semiconductor roadmap?," *Appl. Phys. A*, vol. 80, pp. 1141–1151, 2005.

[53] O. Brand, G. K. Fedder, C. Hierold, J. G. Korvink, and O. Tabata, *Carbon Nanotube Devices: Properties, modeling, integration and applications.* Wiley-VCH, 2008.

[54] M. P. Anantram and F. Léonard, "Physics of carbon nanotube electronic devices," *Rep. Prog. Phys.*, vol. 69, pp. 507–561, 2006.

[55] P. G. Collins, K. Bradley, M. Ishigami, and A. Zettl, "Extreme oxygen sensitivity of electronic properties of carbon nanotubes," *Science*, vol. 287, pp. 1801–1804, 2000.

[56] H. E. Romero, G. U. Sumanasekera, S. Kishore, and P. C. Eklund, "Effects of adsorption of alcohol and water on the electrical transport of carbon nanotube bundles," *J. Phys. Condens. Matter*, vol. 16, pp. 1939–1949, 2004.

[57] K. R. Moonoosawmy and P. Kruse, "Cause and consequence of carbon nanotube doping in water and aqueous media," *J. Am. Chem. Soc.*, vol. 132, pp. 1572–1577, 2010.

[58] L. Hu, D. S. Hecht, and G. Grüner, "Carbon nanotube thin films: Fabrication, properties and applications," *Chem. Rev.*, vol. 110, no. 10, pp. 5790–5844, 2010.

[59] S. Kirchmeyer and K. Reuter, "Scientific importance, properties and growing applications of poly(3,4-ethylenedioxythiophene)," *J. Mater. Chem.*, vol. 15, pp. 2077–2088, 2005.

[60] Z. Wu, Z. Chen, X. Du, J. M. Logan, J. Sippel, M. Nikolou, K. Kamaras, J. R. Reynolds, D. B. Tanner, A. F. Hebard, and A. G. Rinzler, "Transparent, conductive carbon nanotube films," *Science*, vol. 305, pp. 1273–1276, 2004.

[61] D. Sun, M. Y. Timmermans, Y. Tian, A. G. Nasilbulin, E. L. Kauppinen, S. Kishimoto, T. Mizuntani, and Y. Ohno, "Flexible high-performance carbon nanotube integrated circuits," *Nature Nanotech.*, vol. 6, pp. 156–161, 2009.

[62] S. Suzuki, C. Bower, Y. Watanabe, and O. Zhou, "Work functions and valence band states of pristine and Cs-intercalated single-walled carbon nanotube bundles," *Appl. Phys. Lett.*, vol. 76, no. 26, pp. 4007–4009, 2000.

[63] J. Li, L. Hu, J. Liu, L. Wang, T. J. Marks, and G. Grüner, "Indium tin oxide modified transparent nanotube thin films as effective anodes for flexible organic light-emitting diodes," *Appl. Phys. Lett.*, vol. 93, no. 8, p. 083306, 2008.

[64] A. Lin, N. Patil, K. Ryu, A. Badmaev, L. G. D. Arco, C. Zhou, S. Mitra, and H.-S. P. Wong, "Threshold voltage and on-off ratio tuning for multiple-tube carbon nanotubes FETs," *IEEE Trans. on Nanotech.*, vol. 8, no. 1, pp. 4–9, 2009.

[65] Q. Cao, H. Kim, N. Pimparkar, J. P. Kulkarni, C. Wang, M. Shim, K. Roy, M. A. Alam, and J. A. Rodgers, "Medium-scale carbon nanotube thin-film integrated circuits on flexible plastic substrates," *Nature*, vol. 454, pp. 495–500, 2008.

[66] C. Wang, J. Zhang, K. Ryu, A. Badmaev, L. G. D. Arco, and C. Zhou, "Wafer-scale fabrication of separated carbon nanotube thin-film transistors for display applications," *Nano Lett.*, vol. 9, no. 12, pp. 4285–4291, 2009.

[67] K. Shin, H. Jeon, C. E. Park, H. Y. Kim, G. L. Cho, and J. H. Han, "A low voltage operational single-walled carbon nanotube thin-film transistor containing a high capacitance gate dielectric layer produced by layer-by-layer deposition," *Organic Electronics*, vol. 11, pp. 1403–1407, 2010.

[68] H. E. Unalan, G. Fanchini, A. Kanwal, A. D. Pasquier, and M. Chhowalla, "Design criteria for transparent single-wall carbon nanotube thin-film transistors," *Nano Lett.*, vol. 6, no. 4, pp. 677–682, 2006.

[69] M. Radosavljevic, A. Appenzeller, P. Avouris, and J. Knoch, "High performance of potassium n-doped carbon nanotube field-effect transistors," *Applied Physics Letters*, vol. 84, no. 18, pp. 3693–3695, 2004.

[70] K. Chen, S. A. McGill, and P. Xiong, "Carbon nanotube field-effect transistors with molecular interface," *Appl. Phys. Lett.*, vol. 98, pp. 123110–3, 2011.

[71] E. Artukovic, M. Kaempgen, D. S. Hecht, S. Roth, and G. Grüner, "Transparent and flexible carbon nanotube transistors," *Nano Lett.*, vol. 5, no. 4, pp. 757–760, 2005.

[72] B. H. Chen, H. C. Lin, T. Y. Huang, J. H. Wei, H. H. Wang, M. J. Tsai, and T. S. Chao, "Complementary carbon nanotube gated carbon nanotube thin-film transistor," *Appl. Phys. Lett.*, vol. 88, p. 093502, 2006.

[73] S. Han, J. Chang, A. D. Franklin, A. A. Bol, R. Loesing, D. Guo, G. S. Tulevski, W. Haensch, and Z. Chen, "Wafer scale fabrication of carbon nanotube FETs with embedded poly-gates," *IEEE*, 2010.

[74] T. Mizutani, Y. Okigawa, Y. Ono, S. Kishimoto, and Y. Ohno, "Medium scale integrated circuits using nanotube thin film transistors," *Appl. Phys. Exp.*, vol. 3, p. 115101, 2010.

[75] G. Grüner, "Carbon nanotube transistors for biosensing applications," *Analytical and Bioanalytical Chemistry*, vol. 384, no. 2, pp. 322–335, 2006.

[76] J. Kong, N. R. Franklin, C. Zhou, M. G. Chapline, S. Peng, K. Cho, and H. Dai, "Nanotube molecular wires as chemical sensors," *Science*, vol. 287, no. 5453, pp. 622–625, 2000.

[77] E. Llobert, "Gas sensors using carbon nanomaterials: A review," *Sensors and Actuators B*, vol. 179, pp. 32–45, 2012.

Chapter 3

Thin Film Deposition

3.1 Introduction

This chapter will introduce the Langmuir-Blodgett (LB) method for depositing thin film architectures of organic materials. It begins with a brief history of the technique. This is then followed by the principles of monolayer formation using arachidic acid as an example material. Phase changes observed in the floating layer are explained and finally the transfer of material to a solid substrate is discussed. There is then an overview of other thin film deposition techniques. Where applicable, the relevance of these to the deposition of carbon nanotubes is discussed. Current methods of depositing carbon nanotubes are described, including direct growth and solution processing techniques. Finally, a brief review of Langmuir-Blodgett deposition of carbon nanotubes is presented, outlining the difficulties encountered by others.

3.2 Langmuir-Blodgett Deposition

3.2.1 Historical Background

If certain organic materials are spread (usually via a solvent) onto the surface of an aqueous subphase, they will spread out to form a one-molecule thick film. An early example of this was observed when Benjamin Franklin dropped a teaspoon of oil onto the surface of a pond in London some time around 1770. A century later, Lord Rayleigh quantified this observation with films of olive oil on a water surface; he estimated that such films were between 1 nm to 2 nm in thickness. Agnes Pockels showed that the area of the film could be controlled with barriers and observed that the surface tension was affected by contamination of the water. With Lord Rayleigh's help, Pockels published several papers in Nature documenting this technique and showing the first pressure-area isotherms, which are now so familiar in monolayer research [1, 2, 3]. This work by Pockels encouraged Langmuir to continue the research.

Irving Langmuir was born on January 31, 1881 in Brooklyn, New York. Throughout his career he made many notable contributions in thermionic emission and electrical discharge in gases. In 1912 he discovered that the addition of nitrogen and argon in an electric light bulb protected the tungsten wires from deterioration. These achievements were overshadowed by his research in surface chemistry, for which he was awarded the Nobel Prize in Chemistry in 1932.

Katharine Blodgett worked with Langmuir on the transfer of fatty acid monolayers from water surfaces to solid substrates. This was first formally reported in 1935 [4]. Built up monolayer assemblies are now referred to as Langmuir-Blodgett films. Floating monolayers are referred to as Langmuir films [5].

3.2.2 Equipment

Figure 3.1 shows a three dimensional diagram of the major components of a Langmuir-Blodgett trough. The main part is a shallow trough, in the centre is a deeper well to allow substrates to be passed through the air/water interface by use of the central dipping arm. The two barriers can move to the left and right and are used to compress the monolayer film, generating an increase in surface pressure. The surface pressure is measured using a Wilhelmy plate attached to a microbalance. The plate is held in the water and experiences a downward force due to gravity and surface tension, and buoyancy due to displaced water.

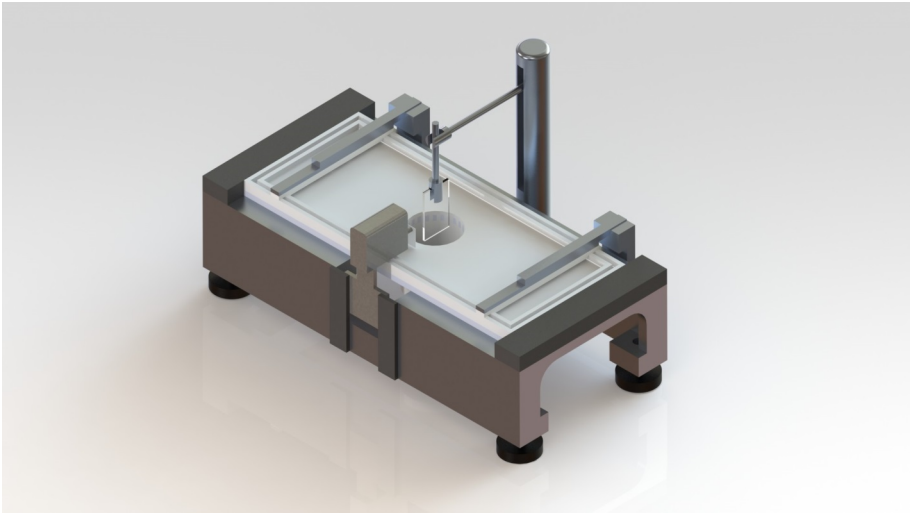

Figure 3.1: *Three dimensional diagram showing the major components of a Langmuir-Blodgett trough.*

3.2.3 Film Transfer

The Langmuir-Blodgett (LB) technique is a simple and elegant means of transferring organic monolayers onto solid substrates. When certain organic materials are added to the surface of a liquid, a layer is formed at the interface between two different materials. This is usually between a gaseous and liquid phase, but it can be at the interface between two different liquid phases [6]. Figure 3.2 shows an arachidic acid

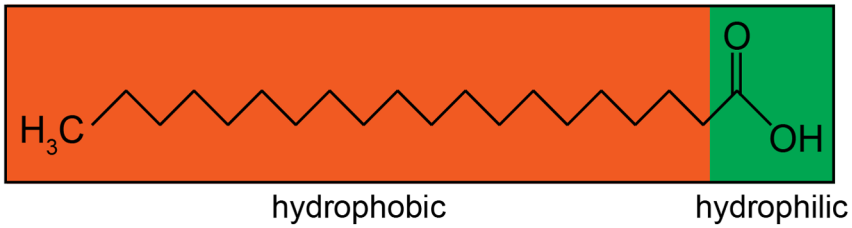

Figure 3.2: *Arachidic acid molecule ($C_{20}H_{40}O_2$) showing the hydrophilic head and hydrophobic tail.*

molecule ($C_{20}H_{40}O_2$), a classical material used for LB film formation and deposition. The molecule consists of two main parts, a hydrophobic tail and a hydrophilic head. When a solution of these molecules is distributed dropwise onto the water surface, the solvent evaporates and the amphiphilic molecules align themselves as the hydrophilic head is attracted to the water surface. Figure 3.3(a) shows the molecules after they have been spread and the solvent has evaporated; they are relatively unorganised. To produce a uniform film, the barriers are moved towards each other to force the molecules closer together (Figure 3.3(b)). This causes them to pack very tightly together.

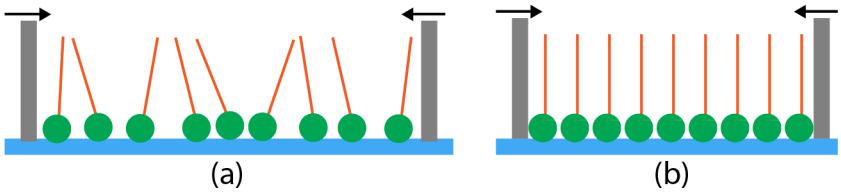

Figure 3.3: *Diagram of a monolayer of arachidic acid on a water subphase, (a) shows the barriers apart and (b) shows the barriers compressed. Adapted from [6].*

A surface pressure versus area isotherm is used to provide information about phase changes of a floating monolayer on a subphase. These are recorded at constant temperature and are generally just referred to as isotherms. Figure 3.4 shows the typical shape of one of these isotherms. Initially, the molecules are spread far apart with little order, this is referred to as the gaseous phase (region A on the graph). When the monolayer is compressed, this causes the molecules to move closer together

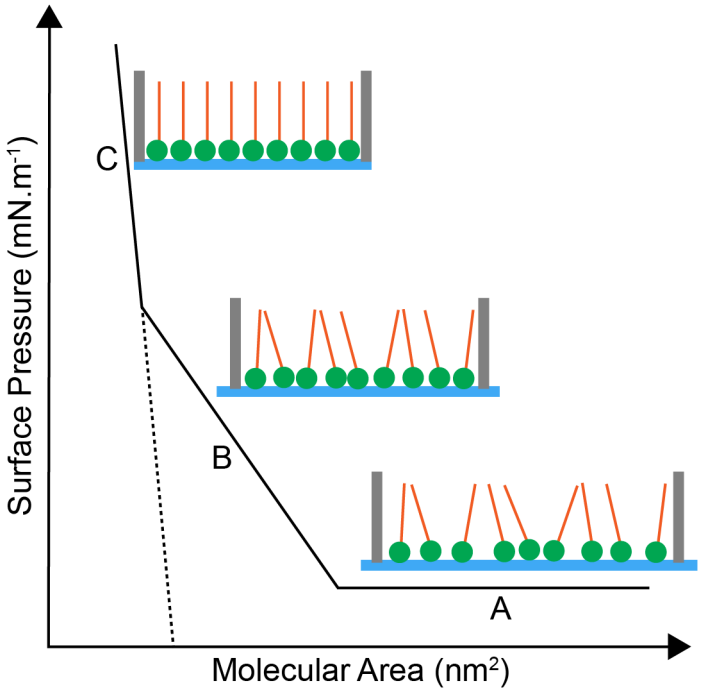

Figure 3.4: *Typical shape of a surface pressure versus molecular area isotherm for a fatty acid, showing gaseous (A), expanded (B) and condensed (C) regions. Adapted from [6].*

and to interact with each other, represented by region B on the graph. This is known as the expanded phase. With further compression, the molecules pack more tightly and the condensed phase (region C) is entered. In this phase, the molecules are packed closely with the hydrophilic group in contact with the water. This graph shows a simplified isotherm, there can be multiple expanded and condensed phases for some materials.

Langmuir-Blodgett deposition is usually performed when the monolayer is in the condensed phase region, Figure 3.5(a) shows the molecules tightly packed on the surface of water. The monolayer is held at a constant pressure and a substrate is lowered through the monolayer into the subphase. When this is withdrawn, (Figure 3.5(b)) a monolayer is transferred to the substrate. On each subsequent pass through the air-water interface, a further monomolecular layer is picked up (Figure 3.5(c)) and a multilayer molecular film is built up on the substrate (Figure 3.5(d)). This allows for very precise control over the thickness of the film.

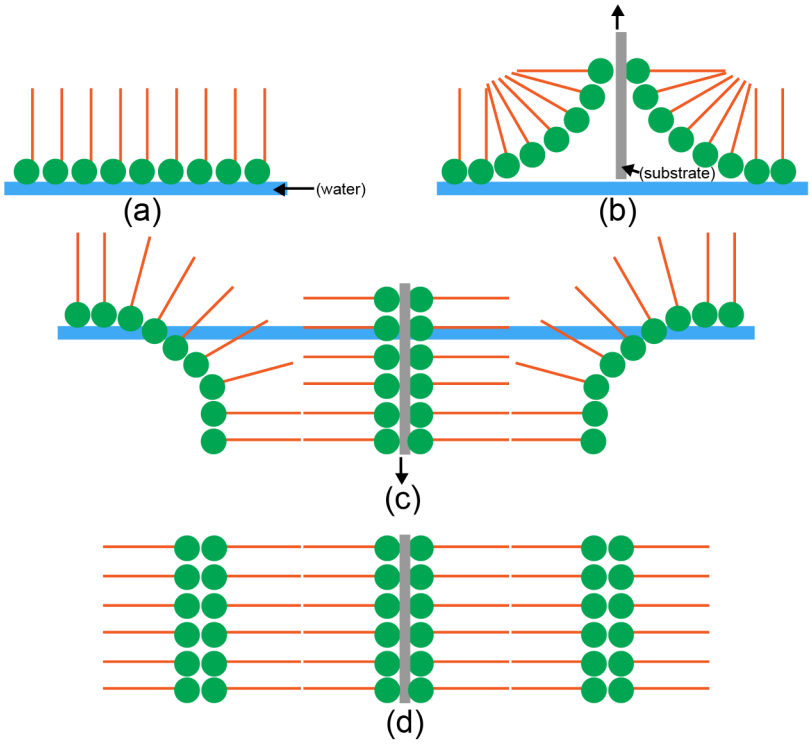

Figure 3.5: *Diagram showing (Y-type) LB deposition with (a) showing the monolayer, (b) substrate withdrawn through the monolayer, (c) substrate lowered through the monolayer and (d) substrate with molecules stacked tail to tail and head to head. Adapted from [6].*

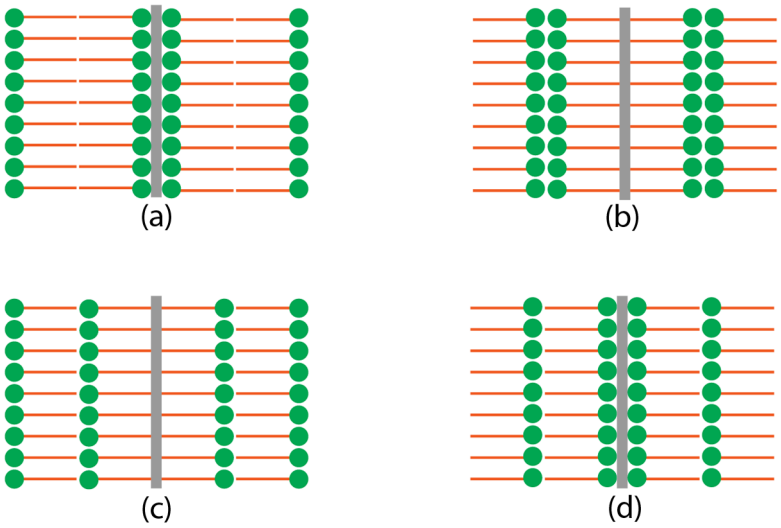

Figure 3.6: *Stacking of molecules for (a) Y-type deposition on a hydrophilic substrate, (b) Y-type deposition on a hydrophobic substrate, (c) X-type deposition and (d) Z-type deposition. Adapted from [6].*

Figure 3.6 illustrates the different types of LB deposition possible. Diagrams (a) and (b) both depict Y-type deposition on hydrophilic and hydrophobic substrates, respectively. This occurs when the first layer is picked up on the first upstroke (hydrophilic) or downstroke (hydrophobic) through the air/water interface. A layer is then picked up on each subsequent traverse through the air/water interface. The molecules stack in a tail-to-tail and head-to-head manner. X-type deposition occurs when the monolayer is transferred to the substrate on the downstroke only, resulting in the tails attaching to the substrate and then subsequent layers attaching head-to-tail (c). Z-type deposition occurs on the upstroke only (d), with the heads attaching to the substrate and then subsequent layers attaching tail-to-head.

The quality of film transfer can be characterised by referring to the deposition (or transfer) ratio, τ, given by [5]

$$\tau = A_L/A_S \tag{3.1}$$

where A_L is the decrease in area occupied by the monolayer on the subphase surface and A_S is the coated area of the substrate. Ideal film transfer would have a transfer ratio of 1, i.e. the decrease in area of the monolayer is equal to the area of the substrate coated. It should be noted that this is an apparent transfer ratio because it is not known whether the transferred film has completely deposited on the substrate. Some material may be lost from the monolayer through evaporation or collapse into the subphase.

3.3 Other Thin Film Deposition Techniques

This section will briefly outline other common thin film deposition techniques. A selection of these will be used for the fabrication of electrodes and devices; the application to the deposition of nanotubes will also be discussed where appropriate.

3.3.1 Chemical Self-Assembly

When an appropriate substrate is immersed into a solution of the desired material, a monomolecular layer is formed on the substrate surface. The most widely known examples of self-assembly are organosilicon compounds on hydroxylated surfaces (SiO_2, Al_2O_3 and glass etc.) and alkanethiols on gold, silver and copper. Self-assembly occurs because of the strong interactions between the head group of the material being deposited and the surface of the substrate. Multilayer films can be built up using chemical treatments between each monolayer deposition step to give the subsequent layers a suitable surface to assemble on. Self-assembly has been shown by Wang et al. [7] to be a successful means of depositing thin films of SWCNTs as the active layer in field effect transistor devices. By using specific surface treatments, semiconducting nanotubes can be selectively deposited on the substrate [8].

3.3.2 Electrostatic Layer-by-layer Assembly

Layer-by-layer (LbL) deposition is a thin film fabrication technique in which layers of oppositely charged materials are deposited on substrates. Polyelectrolytes (PEs) are polymers consisting of a macro-ion (a macromolecule carrying covalently bound anionic or cationic groups) and a low molecular weight counter ion to retain electroneutrality. The material to be deposited is wrapped in two different polyelectrolytes, one positively charged and the other negatively charged. A schematic diagram of the LbL deposition process is shown in Figure 3.7. Deposition is performed by alternately immersing a suitably charged substrate in polyanion and polycation solutions. The substrate is washed in water between each immersion step to remove excess polyelectrolyte.

A wide range of substrates can be used with LbL deposition, with few restrictions on size or shape. The only requirement is that the surface must possess

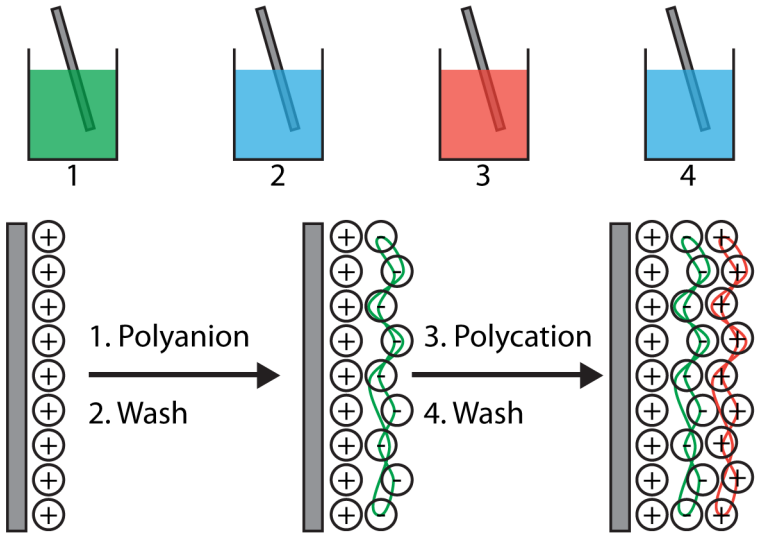

Figure 3.7: *Schematic diagram of LbL deposition showing a positively charged substrate picking up a negatively charged layer, then a positively charged layer. Adapted from [9].*

an electric charge. This can be applied either by chemical treatment (such as aminosilanisation), through plasma treatment or with the deposition of an amphiphilic monolayer using the Langmuir-Blodgett (LB) method. Metal substrates can also be used; these usually have a slight negative charge. Other advantages of LbL deposition include: (a) a wide range of substances can be deposited; (b) a wide range of solvents can be used; and (c) surface properties can be tailored to achieve desired structures and properties.

3.3.3 Spin-Coating

Spin-coating is widely used by the microelectronics industry for depositing layers of photoresist films, generally polymers on silicon wafers. Figure 3.8 shows the steps involved in this procedure. First, an excess amount of solution is dispensed onto the substrate (a), this is then rotated at a low number of revolutions per minute (rpm) to spread the material on the surface (b). Next, the substrate is spun at a speed of several thousand rpm (c) to spread the solution outwards, reducing the film

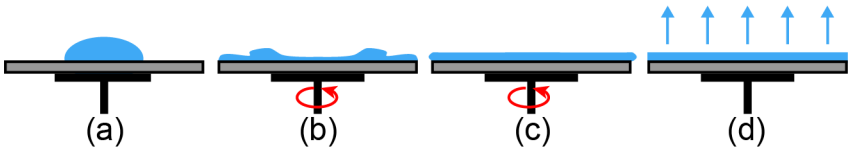

Figure 3.8: *Schematic diagram showing spin-coating, adapted from [10].*

thickness. Finally the film is heated to evaporate the solvent leaving a thin film of uniform thickness (d).

The initial volume of fluid dispensed has very little effect on the final film thickness. The viscosity of the fluid and final spin speed are also important parameters which determine the film thickness. An increase in spin speed or decrease in fluid viscosity decreases the film thickness; the relationship between the thickness dependence on the final spin speed usually follows an inverse power-law. The thickness of the film, d, can be expressed by

$$d = \left(\frac{\eta}{4\pi\rho\omega^2}\right)^{\frac{1}{2}} t^{-\frac{1}{2}} \tag{3.2}$$

where, η is the solution viscosity coefficient, ρ is its density, ω is the angular velocity of spinning and t is the spinning time [10]. If very thin films are desired, the dilute solutions used often lead to pinholes in the final film. Organic molecules can be successfully deposited by spin coating, including various conducting polymers, dyes and certain phthalocyanine materials.

3.3.4 Inkjet Printing

There is a requirement in microelectronics to pattern devices over large areas. The development of inkjet printing offers a simple route to patterning many solution based materials, including nanoparticles, conducting polymers, metals and ceramics

[11]. There are several different inkjet printing technologies. Continuous inkjet printing involves a jet of ink passing through an orifice with a region under the influence of an external electric field. The drops can be deflected on to a substrate as desired to create a pattern. Drop-on-demand printers achieve droplet ejection with either thermal (bubble-jet) or piezoelectric modes of operation. Schematic diagrams of both are shown in Figure 3.9. Piezoelectric technology is favoured because it applies no thermal load to the inks. Inkjet printing offers a greater level of control over the patterning of materials compared to other solution based techniques, such as spin coating or drop casting [12]. Inkjet printing is a room temperature solution based process, ideal for depositing materials onto plastic substrates.

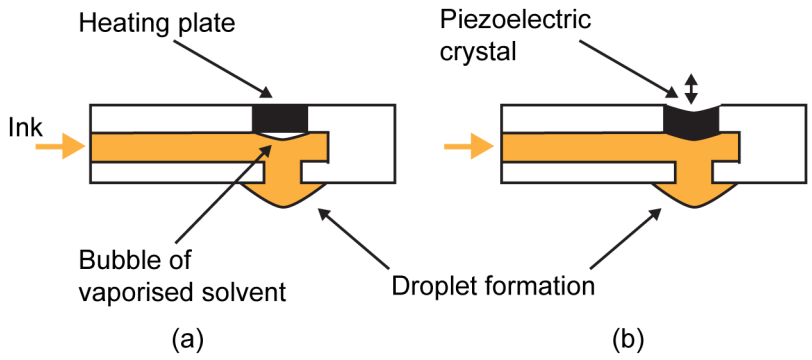

Figure 3.9: *Schematics of (a) thermal and (b) piezoelectric operated print heads, adapted from [10].*

The size of the nozzle is typically between 20 µm to 70 µm, giving droplet sizes of between 4 pl to 180 pl, with some printers being able to produce droplets as small as 1 pl. For successful printing, the properties of the ink must be matched to the specific printer; the ink viscosity and surface tension are key parameters. The surface tension must be high enough to hold the ink in the nozzle without dripping, but the viscosity must be low enough to allow quick refilling. Clogging of the nozzle can be a significant issue with this method of thin film deposition, particularly when materials such as carbon nanotubes are used.

3.3.5 Solution Casting

Solution casting, or drop dispensing allows for very quick deposition of material on a substrate. The chosen material is dissolved in a suitable solvent and then spread dropwise on a substrate from a suitable syringe. As the solvent evaporates, the material is left behind on the substrate. This forms relatively thick films and can yield satisfactory results with minimum equipment requirements.

3.4 Carbon Nanotube Deposition Techniques

There are two primary classifications of deposition techniques used for CNT film fabrication, direct growth processes and solution based processes. These will be briefly described below and the advantages and disadvantages of each will be discussed.

3.4.1 Direct Growth

The most common method for direct growth of carbon nanotubes is chemical vapour deposition (CVD), described in Section 2.4. Catalyst nanoparticles on the substrate are used as seeds for CNT growth, allowing for precise control over where the CNTs grow. The CVD method can produce very small quantities of material (submonolayer density) up to macroscopic quantities. Figure 3.10 shows vertically aligned CVD-grown SWCNTs next to a matchstick for scale.

The density is simply controlled by catalyst density and growth time. Compared with a solution based process, direct growth results in individually separated nanotubes with fewer defects and improved contacts between CNTs, leading to highly conductive films [14]. Films grown directly on a substrate may contain

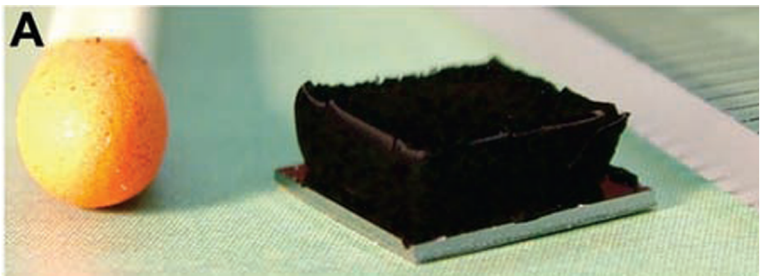

Figure 3.10: *Image showing vertically CVD-grown SWCNTs next to a matchstick head (A) for scale, taken from [13].*

significantly higher amounts of residual catalyst. Using this method leads to difficult density control and the substrates used may not be compatible for device integration. Furthermore, CVD is a high temperature and high vacuum procedure, so does not lend itself to substrates used in the emerging field of plastic electronics.

3.4.2 Solution Processing

Solution based processing has many advantages over direct growth methods for thin film fabrication. It is a low temperature process (typically $<100\,^{\circ}\mathrm{C}$) so is compatible with most plastic substrates. It does not require a high vacuum system, thus significantly reducing costs associated with manufacture, and offers improved up-scaling to mass production with roll-to-roll techniques boasting speeds of up to 300 ft/min [15]. Other solution based processes include: spray coating [16, 17, 18], spin-coating [19], vacuum filtration [20, 21], inkjet printing [22, 23, 24] and Langmuir-Blodgett deposition [25, 26, 27]. Solution preparation is key to successful film fabrication. The purification and dispersion of CNTs in aqueous solutions with the aid of surfactants, or direct dispersion in organic solvents is a common topic of interest in the literature.

Due to their high aspect ratio, CNTs experience large van der Waals forces causing them to aggregate and form large bundles (or ropes) [28]. This presents a major challenge in fabricating thin films from CNT solutions. Separating the tubes by

using covalent chemistries or other harsh treatments (such as oxidation) can lower their electrical conductivity [14]. There are three main categories of dispersion into solution: surfactants as dispersing aids, polymers as dispersing aids and direct dispersion of pristine or functionalised CNTs in organic solvents and water. The dispersion aids are usually removed following film formation due to their insulating nature, however this can prove to be problematic as they can interact strongly with the nanotubes.

Surfactants are the most widely used method of CNT dispersion due to their ability to individualise CNTs at high concentrations. Islam et al. [29] report 63 % individual CNTs at concentrations of 20 mg/ml with sodium dodecylbenzene sulfonate (NaDDBS) as the surfactant. Other commonly used surfactants are Triton X-100 [29] and sodium dodecyl sulfate [30]. Nanotubes can be mixed with polymers in organic solvents to improve dispersion [31]. Dispersions of CNTs can also be made without the use of surfactants in many organic solvents such as methanol, chloroform and dichlorobenzene [32, 14]. Other solvents used such as N-methyl-2-pyrrolidone (NMP) also show good dispersion [33]. The main advantage of dispersing nanotubes without surfactants (or other additives) is to minimise unwanted residue in the deposited films. However, the maximum concentration is more limited than with surfactant based aqueous solutions and effective dispersion can prove to be problematic. Chemical modification, producing thiophenyl-modified SWCNTs [34] or acid refluxed CNTs with carboxylic acid (-COOH) groups produced through an oxidation process [35], can improve solubility in organic solvents. Although dispersion is improved with these approaches, damage is caused to the CNTs through excessive chemical treatment, particularly where oxidising agents are used to functionalise the nanotubes [36].

3.4.3 Langmuir-Blodgett Deposition with Carbon Nanotubes

There are several reports of successful film transfer with CNTs. A variety of methods are used to prepare the CNT solution to aid in dispersion on the water surface. As CNTs are highly hydrophobic, they do not naturally spread on the surface of the water. This is in contrast to classical amphiphilic molecules such as arachidic acid in which the hydrophilic head is attracted to the water surface. However, dispersing CNTs in an amphiphilic polymer to aid in floating layer formation and subsequent film transfer [26, 37] has been reported. In other work, successful LB deposition without the need for a polymer matrix has been investigated. The SWCNTs are chemically solubilised by oxidation to introduce carboxylic acid groups and further reaction with thionyl chloride to introduce acyl chloride groups onto the SWCNTs [25]. Films of up to 100-layers were built up by vertical dipping showing a linear relationship between the optical absorption and the number of layers. The films also showed alignment through polarised light absorbance experiments.

An alternative to dispersing the nanotubes in a polymer or increasing solubility in organic solvents through chemical modification is to suspend the nanotubes in aqueous solution through the use of surfactants. Standard LB techniques require the material to be spread from solution in organic solvents such as chloroform to allow layer formation at the air/water interface. However, aqueous solutions of CNTs can be used if the water soluble tube/surfactant complex is stabilised at the air/water interface through addition of poly(allylamine hydrochloride) to the subphase [38]. Films of pure SWCNTs suspended in chloroform have successfully been transferred to solid substrates through LB deposition [27, 39, 40]. The advantage of preparing films with no additional surfactant, polymer or chemical modification to the SWCNTs is superior electrical properties. Langmuir-Blodgett deposition of films of pure SWCNTs will form the basis of this work.

3.5 Conclusions

The Langmuir-Blodgett deposition technique has been introduced in this chapter as a means of forming multilayer architectures of organic materials. The "classic" example with arachidic acid (an amphiphilic molecule) was discussed. This started with the formation of a floating layer at an air/water interface. The change in order of the molecules on the water surface was highlighted as the floating layer was compressed, showing the gaseous, expanded and condensed regions. Using a film held at a constant pressure in the condensed region, transfer to solid substrates was described with differing types of deposition being noted depending on the hydrophobic nature of the substrate. Other thin film techniques were introduced including self assembly, layer-by-layer, spin coating, inkjet printing and solution casting. The advantages and disadvantages of these techniques have been discussed as well as their relevance to the formation of carbon nanotube thin films. The final section focused on the formation of carbon nanotube thin films, primarily by direct growth and solution processing techniques. Although direct growth allows for greater control of the nanotubes during growth, solution based processes are favoured due to the lower temperatures involved. A short review on the formation of nanotube solutions was presented with the benefits associated with differing routes to suspending nanotubes in solution and the importance of this for reliable device fabrication. Finally, existing reports on the deposition of thin films of carbon nanotubes by LB deposition were discussed. Different methods of solution preparation were described, including surfactant, polymer and fatty acid addition to the material to aid in spreading on the water subphase.

References

[1] A. Pockels *Nature*, vol. 43, p. 437, 1891.

[2] A. Pockels *Nature*, vol. 46, p. 418, 1892.

[3] A. Pockels *Nature*, vol. 48, p. 152, 1893.

[4] K. B. Blodgett *J. Am. Chem. Soc.*, vol. 57, p. 1007, 1935.

[5] G. Roberts, *Langmuir-Blodgett Films*. Plenum Press, 1990.

[6] M. C. Petty, *Langmuir-Blodgett Films – An Introduction*. Cambridge University Press, 1996.

[7] C. Wang, J. Zhang, K. Ryu, A. Badmaev, L. G. D. Arco, and C. Zhou, "Wafer-scale fabrication of separated carbon nanotube thin-film transistors for display applications," *Nano Lett.*, vol. 9, no. 12, pp. 4285–4291, 2009.

[8] M. C. LeMieux, M. Roberts, S. Barman, Y. W. Jin, J. M. Kim, and Z. Bao, "Self-sorted, aligned nanotube networks for thin-film transistors," *Science*, vol. 321, pp. 101–104, 2008.

[9] Surflay Nanotec GmbH, "Layer-by-layer technology," Nov. 2012. `http://www.nanointegris.com/skin/frontend/default/nano/downloads/Carbon%20Nanotubes%20Technical%20Data%20Sheet.pdf`.

[10] M. C. Petty, *Molecular electronics: from principles to practice*. Wiley, 2007.

[11] P. Calvert, "Inkjet printing for materials and devices," *Chemistry of Materials*, vol. 13, no. 10, pp. 3299–3305, 2001.

[12] A. Teichler, J. Perelaer, and U. S. Schubert, "Inkjet printing of organic electronics - comparison of deposition techniques and state-of-the-art developments," *J. Mater. Chem. C.*, vol. 1, pp. 1910–1925, 2013.

[13] K. Hata, D. N. Futaba, K. Mizuno, T. Namai, M. Yumura, and S. Iijima, "Water-assisted highly efficient synthesis of impurity-free single-walled carbon nanotubes," *Science*, vol. 306, pp. 1362–1364, 2004.

[14] L. Hu, D. S. Hecht, and G. Grüner, "Carbon nanotube thin films: Fabrication, properties and applications," *Chem. Rev.*, vol. 110, no. 10, pp. 5790–5844, 2010.

[15] D. S. Hecht, D. Thomas, L. Hu, C. Ladous, T. Lam, Y. Park, G. Irvin, and P. Drzaic, "Carbon-nanotube film on plastic as transparent electrode for resistive touch screens," *Journal of the Society for Information Display*, vol. 17, no. 11, pp. 941–946, 2009.

[16] M. Kaempgen, G. S. Duesberg, and S. Roth, "Transparent carbon nanotube coatings," *Appl. Surf. Sci*, vol. 252, pp. 425–429, 2005.

[17] R. C. Tenent, T. M. Barnes, J. D. Bergeson, A. J. Ferguson, B. To, L. M. Gedvilas, M. J. Heben, and J. L. Blackburn, "Ultrasmooth, large-area, high-uniformity, conductive transparent single-walled-carbon-nanotube films for photovoltaics produced by ultrasonic spraying," *Advanced Materials*, vol. 21, no. 31, pp. 3210–3216, 2009.

[18] K. Shin, H. Jeon, C. E. Park, Y. Kim, H. Cho, G. Lee, and J. H. Han, "A low voltage operational single-walled carbon nanotube thin-film transistor containing a high capacitance gate dielectric layer produced by layer-by-layer deposition," *Organic Electronics*, vol. 11, no. 8, pp. 1403 – 1407, 2010.

[19] S. Manivannan, J. Ryu, H. Lim, M. Nakamoto, J. Jang, and K. Park, "Properties of surface treated transparent conducting single walled carbon nanotube films," *Journal of Materials Science: Materials in Electronics*, vol. 21, pp. 72–77, 2010.

[20] Z. Wu, Z. Chen, X. Du, J. M. Logan, J. Sippel, M. Nikolou, K. Kamaras, J. R. Reynolds, D. B. Tanner, A. F. Hebard, and A. G. Rinzler, "Transparent, conductive carbon nanotube films," *Science*, vol. 305, pp. 1273–1276, 2004.

[21] D. Zhang, K. Ryu, X. Liu, E. Polikarpov, J. Ly, M. E. Thompson, and C. Zhou, "Transparent, conductive, and flexible carbon nanotube films and their application in organic light-emitting diodes," *Nano Lett.*, vol. 6, no. 9, pp. 1880–1886, 2006.

[22] W. Small and M. Panhuis, "Inkjet printing of transparent, electrically conducting single-walled carbon-nanotube composites," *Small*, vol. 3, no. 9, pp. 1500–1503, 2007.

[23] K. Kordás, T. Mustonen, G. Tóth, H. Jantunen, M. Lajunen, C. Soldano, S. Talapatra, S. Kar, R. Vajtai, and P. Ajayan, "Inkjet printing of electrically conductive patterns of carbon nanotubes," *Small*, vol. 2, no. 8-9, pp. 1021–1025, 2006.

[24] H. Okimoto, T. Takenobu, K. Yanagi, Y. Miyata, H. Shimotani, H. Kataura, and Y. Iwasa, "Tunable carbon nanotube thin-film transistors produced exclusively via inkjet printing," *Advanced Materials*, vol. 22, no. 36, pp. 3981–3986, 2010.

[25] Y. Kim, N. Minami, W. Zhu, S. Kazoui, R. Azumi, and M. Matsumoto, "Langmuir-Blodgett films of single-wall carbon nanotubes: Layer-by-layer deposition and in-plane orientation," *Jpn. J. Appl. Phys.*, vol. 42, pp. 7629–7634, 2003.

[26] Y. Guo, N. Minami, S. Kazaoui, J. Peng, M. Yoshida, and T. Miyashita, "Multi-layer LB films of single-wall carbon nanotubes," *Physica B*, vol. 323, pp. 235–236, 2002.

[27] C. Venet, C. Pearson, A. S. Jombert, M. F. Mabrook, D. A. Zeze, and M. C. Petty, "The morphology and electrical conductivity of single-wall carbon nanotube thin films prepared by the Langmuir-Blodgett technique.," *Colloids and Surfaces A*, vol. 354, pp. 113–117, 2010.

[28] L. A. Girifalco, M. Hodak, and R. S. Lee, "Carbon nanotubes, buckyballs, ropes and a universal graphitic potential," *Phys. Rev. B*, vol. 62, no. 19, p. 13104, 2000.

[29] M. F. Islam, E. Rojas, D. M. Bergey, A. T. Johnson, and A. G. Yodh, "High weight fraction surfactant solubilization of single-wall carbon nanotubes in water," *Nano. Lett.*, vol. 3, no. 2, pp. 269–273, 2003.

[30] L. Jiang, L. Gao, and J. Sun, "Production of aqueous colloidal dispersions of carbon nanotubes," *Journal of Colloid and Interface Science*, vol. 260, no. 1, pp. 89 – 94, 2003.

[31] S. L. Hellstrom, H. W. Lee, and Z. Bao, "Polymer-assisted direct deposition of uniform carbon nanotube bundle networks for high performance transparent electrodes," *ACS Nano.*, vol. 3, no. 6, pp. 1423–1430, 2009.

[32] A. Rahy, P. Bajaj, I. H. Musselman, S. H. Hong, Y.-P. Sun, and D. J. Yang, "Coating of carbon nanotubes on flexible substrate and its adhesion study," *Appl. Surf. Sci.*, vol. 255, pp. 7084–7089, 2009.

[33] P. Beecher, P. Servati, A. Rozhin, A. Colli, V. Scardaci, S. Pisana, T. Hasan, A. J. Flewitt, J. Robertson, G. W. Hsieh, F. M. Li, A. Nathan, A. C. Ferrari, and W. I. Milne, "Ink-jet printing of carbon nanotube thin film transistors," *J. Appl. Phys.*, vol. 102, no. 4, p. 043710, 2007.

[34] J.-H. Lee, W.-S. Kang, B.-S. Choi, S.-W. Choi, and J.-H. Kim, "Fabrication of carbon nanotube AFM probes using the Langmuir-Blodgett technique," *Ultramiscroscopy*, vol. 108, pp. 1163–1167, 2008.

[35] A. Suri and K. S. Coleman, "The superiority of air oxidation over liquid-phase oxidative treatment in the purification of carbon nanotubes," *Carbon*, vol. 49, pp. 3031–3038, 2011.

[36] H. Hu, B. Zhao, M. E. Itkis, and R. C. Haddon, "Nitric acid purification of single-walled carbon nanotubes," *J. Phys. Chem. B.*, vol. 107, no. 50, pp. 13838–13842, 2003.

[37] G. Giancane, A. Ruland, V. Sgobba, D. Manno, A. Serra, G. M. Farinola, O. H. Omar, D. M. Guldi, and L. Valli, "Aligning single-walled carbon nanotubes by means of Langmuir-Blodgett film deposition: Optical, morphological, and photo-electrochemical studies," *Adv. Funct. Mater.*, vol. 20, pp. 2481–2488, 2010.

[38] V. Kristic, G. S. Duesberg, J. Muster, M. Burghard, and S. Roth, "Langmuir–Blodgett films of matrix-diluted single-walled carbon nanotubes," *Chemistry of Materials*, vol. 10, no. 9, pp. 2338–2340, 1998.

[39] M. K. Massey, C. Pearson, D. A. Zeze, B. Mendis, and M. C. Petty, "The electrical and optical properties of orientated Langmuir-Blodgett films of single-walled carbon nanotubes," *Carbon*, vol. 49, pp. 2424–2430, 2011.

[40] M. K. Massey, M. C. Rosamond, C. Pearson, D. A. Zeze, and M. C. Petty, "Electrical behavior of Langmuir–Blodgett networks of sorted metallic and semiconducting single-walled carbon nanotubes," *Langmuir*, vol. 28, no. 43, pp. 15385–15391, 2012.

Chapter 4

Electrical Conduction Mechanisms and FET Theory

4.1 Introduction

This Chapter outlines the three important electrical conduction mechanisms applied to thin film SWCNT architectures. For each mechanism: Schottky emission, Poole-Frenkel conduction and variable range hopping, the physical basis of each process is described along with relevant equations. The voltage and temperature dependences of conductivity for each conduction mechanism are then presented. An overview of conductivity in thin films of CNTs is then given showing key results and observations made by others. Finally, the operation of an organic thin film transistor (OTFT) is explained as an introduction to the CNT FETs presented in Chapter 9.

4.2 Conduction Mechanisms

4.2.1 Ohmic Conduction

In classical electrical conductivity theory, electrons in a metal are free to move about as if they are an "electron" gas. In a conductor, such as a metal, the conduction band overlaps with the valence band so there is no band gap and there are many free electrons. Ohm's Law states:

$$V = IR \tag{4.1}$$

where V is the potential difference, I is the current and R is the resistance. In this familiar form, it can be seen that the current is directly proportional to the potential difference.

Ohmic Contacts

When the junction between a metal and a semiconductor does not restrict current flow it is said to be Ohmic. The current is limited by the resistance of the bulk of the semiconductor (i.e. Equation 4.1), rather than by emission of carriers across a potential barrier at the contact. Ohmic contacts will show a near linear current versus voltage characteristic when a bias is applied.

4.2.2 Quantum Mechanical Tunnelling

If the energy of an electron is less than the potential barrier at the interface between a metal and insulator, then classical physics predicts that the electron is reflected and

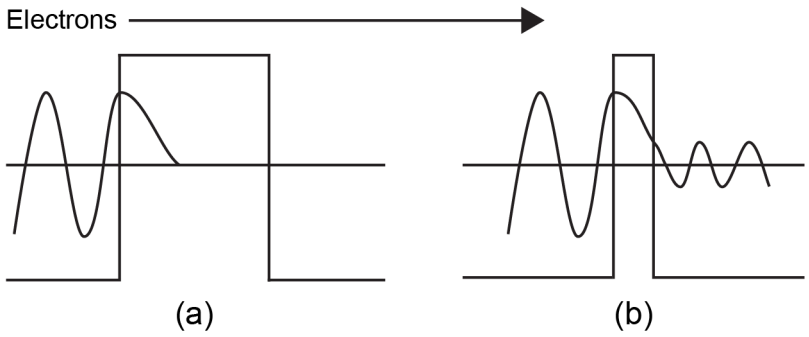

Figure 4.1: *Schematic representation of quantum mechanical tunnelling of an electron wave through (a) a thick barrier and (b) a thin barrier, adapted from [1].*

cannot penetrate the barrier. Quantum mechanics contradicts this view. Because of the wave nature of an electron, it is possible for it to penetrate the forbidden region of the barrier. The wavefunction of an electron decays with increasing depth of penetration from the electrode to insulator interface. With thick barriers, the wave function is zero at the opposite interface, shown in Figure 4.1(a) for a metal-insulator-metal (MIM) structure. The chance of finding an electron at the opposite interface is zero. However, for very thin insulating barriers (<5 nm) the wavefunction has a non-zero value at the opposite interface. There is then a finite probability that an electron can penetrate the insulating barrier and pass from one electrode to the other.

The relationship between current and voltage for tunnelling is complex, and depends on the magnitude of the applied voltage and whether the barrier is symmetric or not. For very low voltages, the tunnelling probability varies exponentially with the barrier thickness. The tunnelling conductivity, σ_t, may be given as

$$\sigma_t = Aexp(-Bd) \tag{4.2}$$

where A and B are constants and d is the thickness of the tunnel barrier [1].

Equation 4.3 shows the temperature dependence of the current density [2]. As can

be seen there is very little temperature dependence of the tunnelling current density.

$$J(V_T) = J(V_0)(1 + 6 \times 10^{-7} T^2) \tag{4.3}$$

4.2.3 Schottky Emission

Schottky emission is a type of thermionic emission which occurs when the potential barrier between a metal and insulator is too thick to permit quantum mechanical tunnelling. The current flowing through the insulator is limited by the rate at which electrons can be thermally excited over the potential barrier into the conduction band of the insulator [3]. This is shown in Figure 4.2, the black line indicating the barrier with no field and the dashed red line illustrating the effect of an applied electric field on the barrier, lowering it by $\Delta\phi$.

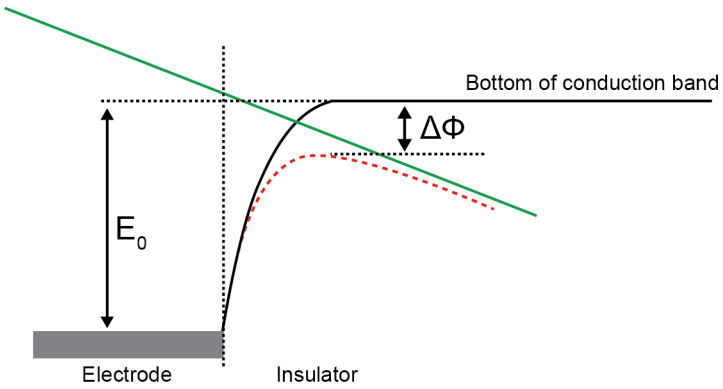

Figure 4.2: *Schottky effect at a neutral contact, where E_0 is the zero field value of E and $\Delta\phi$ shows the lowering of the barrier, adapted from [3].*

For Schottky emission, the voltage dependence of the barrier energy, E is given by the general equation

$$E = E_0 - n\left(\frac{e^3\eta}{4\pi\epsilon_0\epsilon_r d^*}\right)^{\frac{1}{2}} V^{\frac{1}{2}} \tag{4.4}$$

where E_0 is the zero field value of E, d^* is the effective thickness of the film, n and η are parameters based on the type of transport being considered [4]. For Schottky conduction both parameters are unity; however in Poole-Frenkel conduction (see following section) n = 2 with $\eta = 1$ for singly charged traps and $\eta = 2$ for doubly charged trap levels [4]. The permittivity of free space and dielectric constant of the material are given by ϵ_0 and ϵ_r, respectively.

The current I versus voltage V dependence for a metal/insulator dominated by the Schottky effect can be extracted from Equation 4.4 [5]

$$I \propto AT^2 exp\left(-\frac{E_0 - \beta_S V^{\frac{1}{2}}}{kT}\right) \tag{4.5}$$

where A is the Richardson coefficient, T is the temperature, k is the Boltzmann constant and β_S is the Schottky coefficient, given by

$$\beta_S = \left(\frac{e^3}{4\pi\epsilon_0\epsilon_r}\right)^{\frac{1}{2}} \tag{4.6}$$

The following equations show the voltage dependence and temperature dependence if Schottky emission is the dominant conduction mechanism.

Voltage Dependence

If the temperature is fixed, Equation 4.5 may be written as

$$ln[I] \propto V^{\frac{1}{2}} \tag{4.7}$$

Temperature Dependence

At a fixed voltage, the relationship between current and temperature becomes

$$ln\left[\frac{I}{T^2}\right] \propto \frac{1}{kT} \tag{4.8}$$

4.2.4 Poole-Frenkel Conduction

The Poole-Frenkel [6] effect is a bulk trap-regulated, electric field enhanced thermionic emission process [7]. It involves the asymmetric lowering of a Coulombic potential barrier under the influence of an external electric field [3]. This is shown in Figure 4.3; the black lines show the barrier with no applied field, and the dashed red lines show the effect of electric field on the barrier, lowering it by $\Delta\phi$. The gradient of the green line is proportional to the applied field. The energy difference between the donor level and the conduction band is E_d. The electron is thermally excited from the donor level (which is positively charged in the absence of the electron).

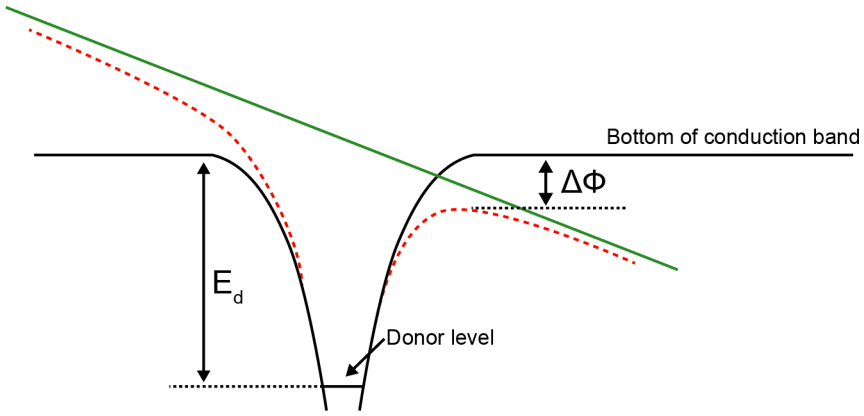

Figure 4.3: *Potential barrier lowering for the Poole-Frenkel effect, adapted from [3].*

In the presence of an electric field, Poole-Frenkel conduction also complies with the general voltage dependence of the energy barrier lowering (Equation 4.4), [5] and may be written as

$$E = E_0 - \left(\frac{e^3\eta}{\pi\epsilon_0\epsilon_r d^*}\right)^{\frac{1}{2}} V^{\frac{1}{2}} = E_0 - \beta_{PF} V^{\frac{1}{2}} \tag{4.9}$$

where β_{PF} is the Poole-Frenkel coefficient

$$\beta_{PF} = 2\beta_S = \left(\frac{e^3}{\pi\epsilon_0\epsilon_r}\right)^{\frac{1}{2}} \tag{4.10}$$

This can be re-written as a current versus voltage dependence

$$I \propto V exp\left(-\frac{E_0 - \beta_{PF}V^{1/2}}{kT}\right) \tag{4.11}$$

Taking this form of the Poole-Frenkel effect (Equation 4.11), it can be tested under the following conditions to see if it dominates conduction.

Voltage Dependence

For a fixed temperature, Equation 4.11 can be written as

$$ln[G] \propto V^{\frac{1}{2}} \tag{4.12}$$

Temperature Dependence

At a fixed voltage, the relationship between the current and temperature becomes

$$ln[I] \propto \frac{1}{kT} \quad \textbf{and} \quad ln[G] \propto \frac{1}{kT} \tag{4.13}$$

Where $G(= I/V)$ is the electrical conductance.

4.2.5 Variable Range Hopping

Variable range hopping (VRH), also known as Mott-VRH, is a mechanism that describes conductivity in disordered systems in the presence of localised states.

Electrons can move between localised states in three ways: they can be thermally activated over the potential barrier, electrons may tunnel through the barrier or can move by a combination of activation and tunnelling. In a disordered solid, the localised states will not be degenerate, so some thermal activation will be required to allow the full state and empty state to resonate, and allow tunnelling. This method of thermally assisted tunnelling is called hopping [1]. Variable range hopping refers to the fact that average hopping distance varies with temperature and is not necessarily to the closest site. The following equation gives the temperature dependence of conduction according to the Mott-VRH model [8]

$$G(T) = G_0 exp\left[-\left(\frac{T_0}{T}\right)^{(\frac{1}{1+d})}\right] \tag{4.14}$$

where G is the conductance at a given temperature, T and G_0 is the conductance at a set temperature, T_0, and d refers to the number of dimensions in which hopping occurs.

4.3 Conductivity Mechanisms in CNT Networks

The following table (Table 4.1) summarises a selection of reports on conductivity in networks as well as isolated single walled carbon nanotubes. Variable range hopping, Poole-Frenkel and tunnelling have all been cited as the dominant conduction mechanism in different SWCNT networks/individual nanotubes. It is common for thick networks of unsorted nanotubes to exhibit metallic conduction. Skákalová et. al. report that for thin films where there are no metallic percolating pathways, variable range hopping becomes dominant. They also report that for individual nanotubes, Schottky contact effects dominate [9].

Jombert et. al. also report metallic conduction for thicker films (where metallic pathways dominate conductivity), however for thinner films they find Poole-Frenkel

conduction dominates [5]. Tunnelling between isolated clusters of nanotubes has been reported for sparse films whose density is below the percolation threshold for conductivity [10, 11].

Author/Date	Network / single tube	Deposition method	Nanotube growth method	Semiconductin Metallic	Contacts	Dominant mechanism	Notes	Ref.
Odom et al. (1998)	Single tube	Spin coated on gold	Laser vaporisation	Mixture, but individual types tested	Tungsten tips	-	STM measurements showing the typical behaviour expected for individual metallic and semiconducting nanotubes	[12]
Ouyang et al. (2001)	Single tube	Spin coated on gold	-	Metallic	Tungsten tips	-	The authors show that "metallic" zigzag and armchair nanotubes are in fact small-gap semiconductors.	[13]
Morgan et al. (2008)	Network of nanotubes	Air-brushing from aqueous solution	HiPCO	Mixture	Interdigitated Cr/Au	3D-VRH	Thin and thick networks of SWCNTs follow Mott's 3D-VRH model. Thin networks follow this mechanism down to lower temperatures as a higher proportion of semiconducting nanotubes will form conducting pathways	[14]
Skákalová et al (2006)	Individual and networks of nanotubes	Dispersed from aqueous solution, brushed for thin networks and vacuum filtration for thick networks.	HiPCO	Mixture	Palladium	VRH for thin networks	Thick films show metallic dominated conductivity, thin films show hopping conductivity as the probability of metallic conducting pathways decreases. Individual nanotubes and very thin networks are dominated by Schottky contact effects at the electrodes.	[9]

continued ...

...continued

Author/Date	Network / single tube	Deposition method	Nanotube growth method	Semiconductin Metallic	Contacts	Dominant mechanism	Notes	Ref.
Perello et al. (2009)	Single nanotubes	Grown in situ, extra nanotubes removed by O_2 plasma etching	CVD	Mixture	Hf/Ti	Poole-Frenkel hopping	Current versus voltage data used to fit to Poole-Frenkel hopping, no low temperature data.	[15]
Jombert et al. (2008)	Network	Layer-by-layer	HiPCO	Mixture	Au	Poole-Frenkel	-	[5]
Palumbo et al. (2006)	Network	Layer-by-layer	Arc discharge	Mixture	Aluminium	Tunnelling	Conductivity in the out-of-plane direction is related to the tunnelling of charge carriers between the nanotubes.	[10]
Bekyarova et al. (2005)	Network	Spray coated on glass	Arc discharge	Mixture	Cr/Ag	Tunnelling	Tunnelling between isolated clusters when the film is below the percolation threshold of conducting pathways.	[11]

Table 4.1: *Summary of literature on conduction mechanisms in CNT thin films.*

4.4 Thin Film Transistors

4.4.1 Structure

A thin film transistor is made up of three parts; an active material (semiconductor), an insulator and three metal electrodes. The semiconductor is in direct contact with two of the electrodes (the source and drain) with the third (gate) electrode being isolated from the semiconductor by the insulator. The structures are built up from thin films of each material using shadow masks or photolithography techniques, depending on the layer order. There are four basic structures: Figure 4.4(a) shows a bottom gate, bottom contact (BGBC) device and (b) shows a bottom gate, top contact (BGTC) device. Figure 4.4(c) shows a top gate, top contact device (TGTC) and (d) shows a top gate, bottom contact (TGBC) device.

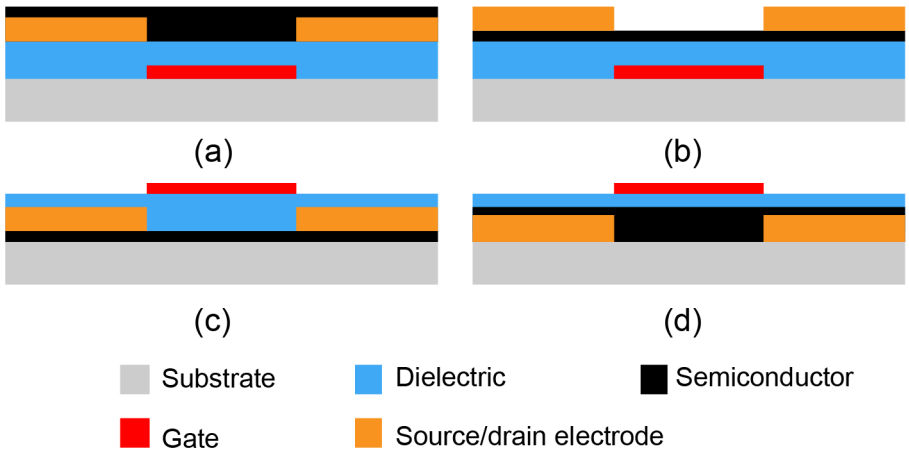

Figure 4.4: *Basic thin film transistor structures showing, (a) BGBC, (b) BGTC, (c) TGTC and (d) TGBC.*

There are advantages and disadvantages for each device structure. A balance has to be made between device performance and the ability to fabricate a device successfully. If BC architectures are used then they can be patterned through photolithography techniques, allowing for better control of the feature size. However, a poorer contact is generally formed to the semiconductor when deposited on top of

the electrodes. If a TC structure is used, then the contacts are usually formed through a shadow mask, with a loss in resolution. However, top contacts are generally found to produce a lower contact resistance to the semiconductor. A TG structure usually aids in generating a greater field effect, however the possibility of short circuits through the dielectric (due to an uneven semiconductor surface) is much higher than with a BG structure.

4.4.2 Operation

Thin film transistors made with SWCNTs as the semiconducting material are generally p-type in behaviour (unless dopants are added). Pentacene is a common p-type material used in organic TFTs, and will be used as the basis for the following discussion. An energy scheme of this semiconductor is given in Figure 4.5 showing the Fermi level of the gold and the frontier orbitals (highest occupied molecular orbital, HOMO, and the lowest unoccupied molecular orbital, LUMO) of pentacene. In a p-type device, negative charges are induced at the source when a positive voltage is applied to the gate. If the LUMO level of the semiconductor (pentacene) is far from the Fermi level of the electrode (gold in this example), there is a substantial energy barrier for electrons, so electron injection is very unlikely. No current passes

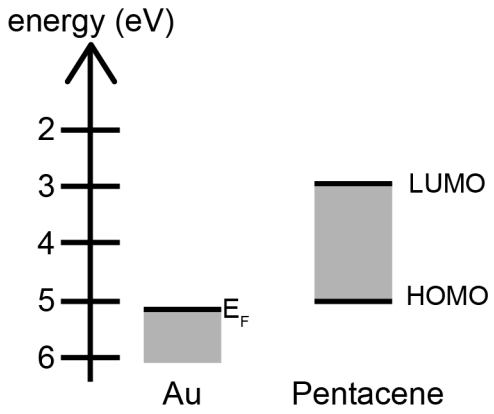

Figure 4.5: *Energy scheme of the gold-pentacene interface, adapted from [16].*

through the semiconductor; any current observed is leakage through the insulator. When a negative gate voltage is applied, holes are easily injected as the Fermi level is close to the HOMO level and the barrier height is low. A conducting channel forms at the semiconductor/insulator interface and current can flow between the source and drain electrodes. An organic semiconductor is said to be n-type when the LUMO level is closer to the Fermi level than the HOMO level.

A thin film transistor operates like a capacitor. When a gate voltage is applied an equal but opposite charge is induced on both sides of the insulator. This forms a conducting channel on the semiconductor side if charge carriers can be injected into the semiconducting material. The conductance of the channel is proportional to the charge, so is also proportional to the gate voltage. The current flowing through the channel follows Ohm's law at low drain voltages, but as it becomes larger the voltage drop at the drain decreases to a point at which it is zero. This occurs when the drain voltage approaches the gate voltage. At this point the channel current becomes independent of the drain bias and the channel is said to be "pinched off".

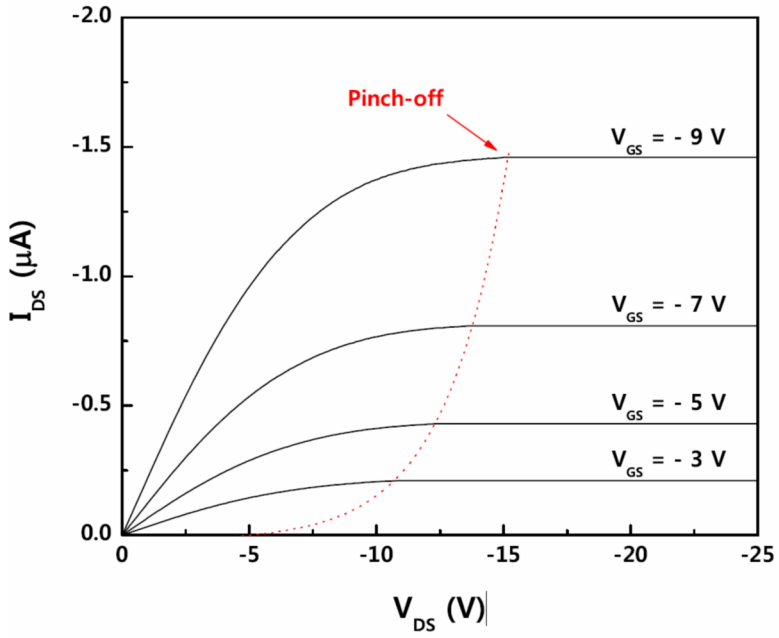

Figure 4.6: *Output characteristics of a typical organic TFT based on p-type material, taken from [17].*

Beyond pinch off the device operates in the saturation region. Figure 4.6 shows the typical output characteristic for a p-type semiconducting based TFT. The gradual transition from the linear to the saturation regime is clearly visible, the point where the channel becomes pinched off is highlighted by the red line.

The linear (I_{Dlin}) and saturation (I_{Dsat})currents can be given by equations 4.15 and 4.16:

$$I_{Dlin} = \frac{W}{L}\mu C_i(V_G - V_T)V_D \tag{4.15}$$

$$I_{Dsat} = \frac{W}{2L}\mu C_i(V_G - V_T)^2 \tag{4.16}$$

where W and L are the channel width and length, C_i is the dielectric capacitance per unit area, V_G and V_D are the gate and drain voltages, and V_T is the threshold voltage (the point at which the conducting channel is "turned on"). These equations assume the mobility is constant and that the electric field along the channel is much lower than that across it.

4.5 Conclusions

This chapter introduced the basics of electrical conductivity, with a brief introduction on Ohmic conduction and the idea of quantum mechanical tunnelling through a thin interface between a metal and insulator. The main conduction mechanisms studied in this work, and indeed the most commonly referenced dominant mechanisms reported for conductivity in carbon nanotubes were introduced: quantum mechanical tunnelling, Schottky emission, Poole-Frenkel hopping and variable range hopping. A brief summary of some key publications highlighted the reported dominant conduction mechanisms and how they apply to differing thickness of films. In general, thick films (where the metallic nanotube content is above the percolation threshold) exhibited metallic conduction, whereas thin films below this threshold tended to show hopping based conduction. Measurements on individual tubes, suggested the presence of a Schottky barrier. The basic operation of an organic thin film transistor with pentacene as the semiconducting material was explained as a background to the final chapter (Chapter 9).

References

[1] M. C. Petty, *Molecular Electronics: From Principles to Practice*. Wiley, 2007.

[2] J. G. Simmons, *DC Conduction in Thin Films*. Mills & Boon, 1971.

[3] J. G. Simmons, "Conduction in thin dielectric films," *J. Appl. Phys. D*, vol. 4, pp. 613–657, 1971.

[4] X. Mathew, J. P. Enriquez, P. J. Sebastien, M. Pattabi, A. Sanchez-Juarez, J. Campos, J. C. McClure, and V. P. Singh, "Charge transport mechanism in a typical Al/CdTe schottky diode," *Sol. Energy Mater. Sol. Cells*, vol. 63, pp. 355–365, 2000.

[5] A. S. Jombert, K. S. Coleman, D. Wood, M. C. Petty, and D. A. Zeze, "Poole-Frenkel conduction in single wall nanotube composite films built up by electrostatic layer-by-layer deposition," *J. Appl. Phys.*, vol. 104, p. 094503, 2008.

[6] J. Frenkel, "On pre-breakdown phenomena in insulators and electronic semiconductors," *Tech. Phys.*, vol. 5, pp. 647–648, 1938.

[7] S. Habermehl and R. T. Apodaca, "Dielectric breakdown and Poole-Frenkel field saturation in silicon oxynitride thin films," *Appl. Phys. Lett.*, vol. 86, p. 072103, 2005.

[8] N. F. Mott, *Conduction in non-crystalline materials*. Clarendon Press, 1987.

[9] V. Skákalová, A. B. Kaiser, Y. S. Woo, and S. Roth, "Electronic transport in carbon nanotubes: From individual nanotubes to thin and thick networks," *Phys. Rev. B*, vol. 74, p. 085403, 2006.

[10] M. Palumbo, K. U. Lee, B. T. Ahn., A. Suri, K. S. Coleman, D. Zeze, D. Wood, C. Pearson, and M. C. Petty, "Electrical investigations of layer-by-layer films of carbon nanotubes," *J. Phys. D: Appl. Phys.*, vol. 39, pp. 3077–3085, 2006.

[11] E. Bekyarova, M. E. Itkis, N. Cabrera, B. Zhao, A. Yu, J. Gao, and R. C. Haddon, "Electronic properties of single-walled carbon nanotube networks," *J. Am. Chem. Soc.*, vol. 127, pp. 5990–5995, 2005.

[12] T. W. Odom, J. Huang, P. Kim, and C. M. Lieber, "Atomic structure and electronic properties of single walled carbon nanotubes," *Nature*, vol. 391, pp. 62–64, 1998.

[13] M. Ouyang, J. Huang, C. L. Cheung, and C. M. Lieber, "Energy gaps in "metallic" single-walled carbon nanotubes," *Science*, vol. 292, pp. 702–705, 2001.

[14] C. Morgan, Z. Alemipour, and M. Baxendale, "Variable range hopping in oxygen-exposed single-wall carbon nanotube networks," *Phys. Stat. Sol. (a)*, vol. 205, no. 6, pp. 1394–1398, 2008.

[15] D. J. Perello, W. J. Yu, D. J. Bae, S. J. Chae, M. J. Kim, Y. H. Lee, and M. Yun, "Analysis of hopping conduction in semiconducting and metallic carbon nanotube devices," *J. Appl. Phys.*, vol. 105, no. 12, pp. 124309–124309–5, 2009.

[16] A. Kahn, N. Koch, and W. Gao, "Electronic structure and electrical properties of interfaces between metals and π-conjugated molecular films," *J. Poly. Sci. B: Polymer Physics*, vol. 41, no. 21, pp. 2529–2548, 2003.

[17] Y. Yun, *Pentacene based organic electronic devices.* PhD thesis, Durham University, 2009.

Chapter 5

Experimental Methods

5.1 Introduction

This chapter will outline key pieces of equipment and the main experimental techniques used in this work. Substrate preparation is described followed by details of solution preparation for the different materials used in this work. Three common metal deposition techniques are discussed: thermal evaporation, electron beam evaporation and sputtering. Photolithography is introduced as a method of patterning thin metal films (deposited by one of the three techniques discussed) and forming the various electrodes used in this work. The experimental set-up for Langmuir-Blodgett deposition is outlined, along with details of the equipment used for AC electric field alignment during deposition. Finally, several analysis techniques are discussed, including: atomic force microscopy, scanning electron microscopy, ellipsometry, current versus temperature and current versus voltage measurements.

5.2 Substrate Preparation

For the work relating to LB networks of nanotubes deposited on substrates with pre-prepared electrodes, see Section 5.5. This section refers to the preparation of blank borosilicate glass slide substrates and single crystal silicon wafer substrates. These required very careful cleaning to ensure the best possible transfer of material when passed through the floating layer of nanotubes at the air/water interface. To begin with, either the silicon or glass was cut to size using a diamond pen (typical sizes for this work ranged from 10 x 20 mm, up to around 20 x 30 mm). The substrates were then cleaned using a standard washing procedure, involving a rinsing step, followed by 15 minutes submersed in the solvent in an ultrasonic bath, further rinsing and then drying using compressed nitrogen. This was carried out with the following solvents in order: acetone, propanol, Decon 90 and de-ionised water.

5.2.1 Surface Treatment

Both hydrophilic and hydrophobic surfaces were required to investigate deposition of the nanotube films. Figure 5.1 shows how a surface can be characterised with a droplet of liquid forming a contact angle of θ (a) less than 90° on a hydrophilic surface and (b) greater than 90° on a hydrophobic surface. The glass and silicon naturally have a hydrophilic surface due to an oxide surface layer. Surface treatments

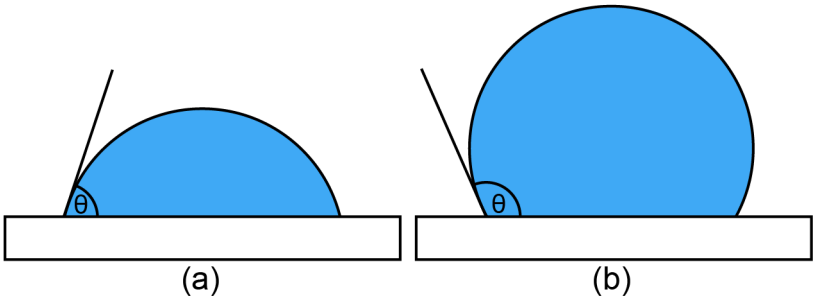

Figure 5.1: *Diagrams showing (a) a hydrophilic surface and (b) a hydrophobic surface. The contact angle is shown as θ.*

were used to change the hydrophobicity of the substrate. After cleaning, some of the substrates were treated with a solution of 2 % dimethyldichlorosilane in trichloroethane. This functionalises the surface of the glass or silicon, removing the negative charge (associated with the oxygen) from the surface. Figure 5.2 illustrates this process.

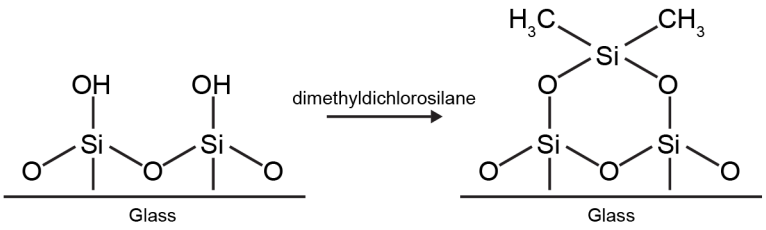

Figure 5.2: *Diagram showing the silanisation process. Adapted from [1].*

5.3 Solution Preparation

All of the carbon nanotubes used in this work were single-walled carbon nanotubes (SWCNTs). Materials from different sources were used along with several different purification methods. The following subsections will explain the preparation of each solution, and for the rest of the thesis they will be referred to by the names given.

5.3.1 Unsorted HiPCO Material

Unsorted HiPCO nanotubes were produced by the high-pressure conversion of carbon monoxide (HiPCO). They were purchased from Carbon Nanotechnologies Inc. (Houston, TX, USA) and were then purified following two different methods, the key difference between the two methods was a high temperature annealing step. All of the material was initially purified using the following procedure. First, the nanotubes were heated in an air furnace to 350 °C for 4 hours, and then washed

in 6 M HCl, with a final rinse in purified water to remove any remaining acid. One solution was made with this material (the "non-annealed" solution, SWCNT-U) by adding 1 mg of the purified solid to 50 ml of chloroform (Fisher Scientific, 99.9 % purity), sonicating for 1 hour and then leaving to stand for a few hours for any undissolved material to settle out. The material used was taken off the top of the suspension to minimise the number of large deposits. For some experiments, the SWCNT-U were filtered using a 2 µm filter to remove any remaining CNT aggregates in the solution. Another solution (the "annealed" solution, SWCNT-U_a) was made up to the same concentration, but with an additional 900 °C annealing stage under vacuum for 9 hours at the end of the purification process. Both solutions produced from this material contain unsorted nanotubes, with a mixture of semiconducting and metallic types [2].

5.3.2 Arc Discharge Sorted Material

Arc discharge sorted nanotubes were produced by the arc discharge method and were purchased from Nanointegris (Skokie, IL, USA) in dried mat form. Due to the high purity of the as-supplied tubes, they were simply dispersed in chloroform using an ultrasonic bath to a concentration of roughly 0.02 mg/ml without any further processing. As reported in the later chapters, some contamination was present and an extra methanol washing step was introduced before dispersing in

Property	**Metallic**	**Semiconducting**
Diameter Range	1.2 nm to 1.7 nm	1.2 nm to 1.7 nm
Mean Diameter	1.4 nm	1.4 nm
Length Range	100 nm - 4 µm	100 nm - 4 µm
Mean Length	∼0.5 µm	∼1 µm
Catalyst Impurities	∼1 % by mass	∼1 % by mass
Carbonaceous Impurities	∼5 % by mass	∼5 % by mass

Table 5.1: *Manufacturer's (Nanointegris) data for the sorted SWCNT used in this work, taken from [3].*

chloroform to try and remove what is thought to be residual surfactant contaminants. Sorted semiconducting and metallic nanotubes were used: named SWCNT-S and SWCNT-M, respectively. Table 5.1 shows the manufacturer's data for the nanotubes used in this work. It is important to note the different average lengths for the semiconducting and metallic nanotubes as this will be a key factor in determining the conductivity when different electrode gaps are considered.

5.3.3 Oxidised HiPCO Material

Oxidised HiPCO nanotubes were supplied by Prof. Karl Coleman (Department of Chemistry, Durham University). HiPCO produced CNTs were oxidised in 2.6 M HNO_3 for 4 hours to introduce acid groups onto the surface of the carbon nanotubes. This length of oxidation should produce functionalisation of around 5 % of the carbon atoms, resulting in a less hydrophobic nanotube. The CNTs were then dispersed into solution by simple sonication in chloroform to a concentration of 0.02 mg/ml. By reducing the hydrophobicity of the nanotubes, it was hoped that they would form more uniform layers on the subphase, with less tendency to group together. These are referred to as SWCNT-O in this work.

5.3.4 Graphene

Graphene was purchased from Nanointegris (Skokie, IL, USA) in aqueous solution form. Details of the solution are given in Table 5.2. This was used as supplied.

Property	Graphene Platelets
Single layer content	27 %
Double layer content	48 %
Triple layer content	20 %
4+ layer content	5 %
Average flake area	10 000 nm^2
Solution type	Aqueous solution
Concentration	0.05 mg/ml
Surfactant concentration	2 % by weight

Table 5.2: *Manufacturer's data for the graphene used in this work, taken from [4].*

5.4 Fabrication Techniques

Although Langmuir-Blodgett deposition was the main study of this work, several other standard thin film deposition techniques were used to fabricate electrodes and devices. These are briefly described in this section.

5.4.1 Metal Evaporation

Sputtering

Sputtering is a process in which atoms are ejected from a solid target material as a result of bombardment by energetic particles. A source of ions is provided by a glow discharge created by an electric field between two electrodes in a gas at low pressure. The target (material to be sputtered) is at the cathode, the chamber is evacuated and then filled with an inert gas at low pressure. A DC voltage of several kilovolts is applied between the electrodes; this ionises the gas and forms a plasma. The positive gas ions are then accelerated by the electric field to the cathode, sputtering the target atoms. A schematic diagram of a sputtering system is shown in Figure 5.3.

The main advantage of sputtering is that almost any material can be deposited. As no heating is required, even materials with very high melting points can be

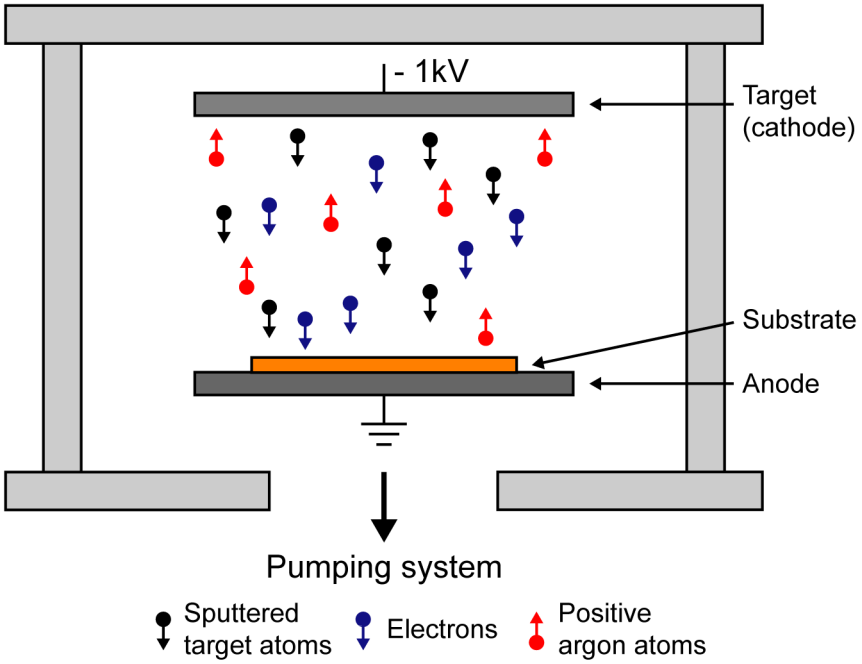

Figure 5.3: *Schematic diagram of a sputtering system using argon as the inert environment, adapted from [5].*

deposited. Sputtering can produce a uniformly thick deposit over large areas. Also, the sputtering rate is proportional to the current flowing between the electrodes so is more controllable than evaporation.

Thermal Evaporation

To make contact to the nanotube films, metals were patterned onto glass substrates by thermal evaporation through a shadow mask. When heated, solid materials vaporise. They can then condense on a cooler substrate. It is important that this process is carried out in a vacuum to ensure that there is a long mean free path. This allows the metal vapour molecules to travel directly to the substrate without colliding with any background gases. Another consideration is the evaporated particles colliding with foreign particles and reacting to form impurities in the deposited film.

A typical evaporation system is shown in Figure 5.4. This consists of a glass bell

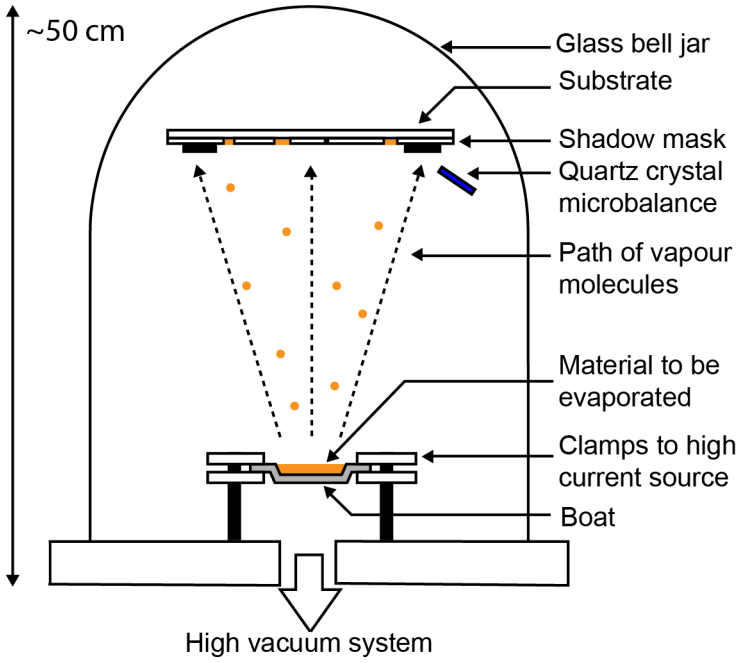

Figure 5.4: *Schematic diagram of a thermal evaporation system.*

jar with a two stage vacuum pumping system comprising of a rotary pump backing a diffusion pump. This is sufficient to create a vacuum in excess of 10^{-5} mbar. The material to be evaporated is held in a tungsten boat connected to a high current source providing sufficient power to heat the source to sublimation temperature. The thickness of the film deposited is measured by the change in oscillating frequency of a quartz crystal microbalance.

In this work an Edwards 306 thermal evaporator was used to deposit metal films of chromium/gold or aluminium for the various electrodes used. The high vacuum (of $<10^{-5}$ mbar) was achieved with an Edwards RV12 rotary pump backing an Edwards E04K diffusion pump. The quartz crystal microbalance was connected to an Edwards film thickness monitor (FTM7) to monitor deposition rate and film thickness.

Electron Beam Evaporation

In electron beam evaporation, the setup is similar to that of thermal evaporation (described in Section 5.4.1). The main difference being that the source material is heated with an electron beam. Electron beam evaporation offers precise control of low or high deposition rates, economical material consumption and works with most metals, numerous alloys and other compounds.

5.4.2 Spin Coating

Spin-coating was used to deposit uniform thin films from solution onto flat substrates. See Section 3.3.3 for for details on this process. A Laurell Technologies WS-400A-6NPP-LITE spin-coater was used for this work.

5.4.3 Photolithography

Photolithography, also known as optical or UV lithography, is a process used to pattern substrates by selectively removing parts of the surface. Figure 5.5 shows the key steps in patterning a thin film of metal on a substrate using a positive photoresist. First, the surface to be patterned was coated with photoresist by spin

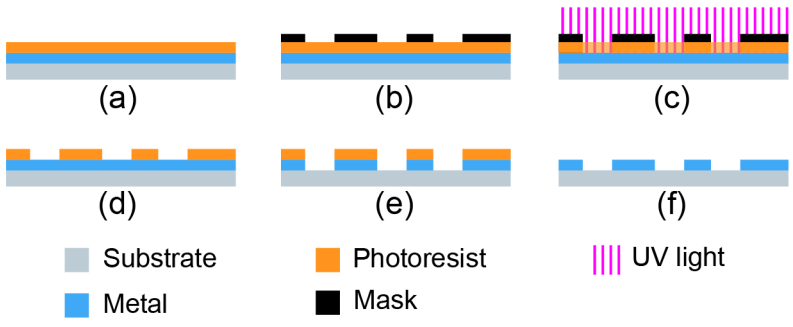

Figure 5.5: *Key steps in photolithography.*

coating (a). A mask was then aligned on the surface (b) and exposed to high intensity UV light (c). The exposure to UV light causes a chemical change in the resist allowing the exposed sections to be removed by a developing solution (d). The exposed areas of the metal were then etched (e) and then the remaining photoresist was removed to leave the patterned metal film on the substrate (f).

5.5 Electrode Preparation

Various types of electrodes were used in this work, including: sub-micron spaced palladium electrodes, linear and interdigitated micron spaced electrodes and large gap silver paint electrodes. The fabrication of these electrodes is discussed in this section.

5.5.1 Interdigitated and Linear Gold Electrodes

Photolithography (Section 5.4.3) was used to pattern interdigitated and linear electrodes in chromium/gold on 4 inch glass wafers. To form the electrodes, a thermally evaporated 5 nm seed layer of chromium was deposited followed by 50 nm of gold. The fingers of the interdigitated electrodes covered an area of 1 mm x 2 mm and had spacings between the fingers of 2 µm, 5 µm, 10 µm, 15 µm, 25 µm and 50 µm. Each set of electrodes consisted of three pairs of electrode pads oriented as shown in Figure 5.6. This allowed measurement of current versus voltage characteristics in different orientations in relation to the direction of dipping.

The linear electrodes were simply pairs of 1 mm x 2 mm gold strips separated by gaps of varying sizes, from 2 µm to 50 µm.

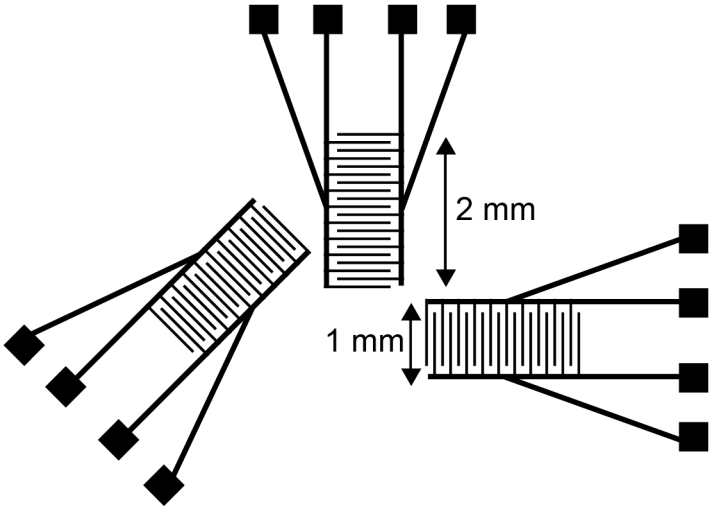

Figure 5.6: *Layout of interdigitated electrodes.*

5.5.2 Sub Micron Linear Electrodes

Electrodes with gaps between 100 and 300 nm were fabricated on glass wafers using a modified version of a controlled undercutting method based on aluminium wet etching [6]. First, the wafers were cleaned by placing them in a solution of a surface active cleaning agent (Decon 90) in an ultrasonic bath for 30 minutes. They were rinsed with de-ionised water before being placed in a 2:1 solution of H_2SO_4:H_2O_2 (piranha solution) for 1 hour. The wafers were then rinsed again and dried with a nitrogen gun before being dehydrated by baking on a hotplate at 200 °C. A multilayer stack of Cr (3 nm), Pd (30 nm) and Al (50 nm) was formed by electron beam evaporation (Figure 5.7(a)). Photoresist was spin coated and imaged by standard photolithography to form rectangular patterns on the surface. After ashing (an oxygen plasma cleaning step) to remove any unwanted photoresist residues, the wafer was submerged in a dilute solution of phosphoric, acetic and nitric acid (PAN) etch to dissolve the aluminium layer. A controlled undercut was formed beneath the photoresist pattern by carefully timing the etching process (Figure 5.7(b)). A second aluminium layer (40 nm) was then deposited by electron beam evaporation (Figure 5.7(c)) before the photoresist was dissolved in acetone, "lifting off" the aluminium

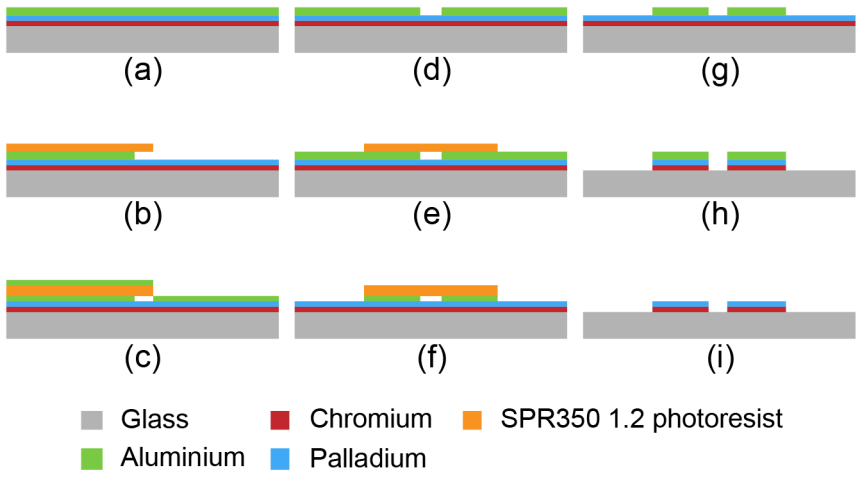

Figure 5.7: *Process to fabricate palladium electrodes on glass.*

on top of the photoresist covered region (Figure 5.7(d)). By using this sequence, it was possible to form an aluminium film containing gaps that followed the edges of the photoresist pattern. The widths of the gaps were defined by the controlled over-etching step.

To divide the film into electrode pairs, a second aligned rectangular photoresist pattern was printed to define the electrode pair (Figure 5.7(e)). The exposed aluminium was dissolved in PAN etch (Figure 5.7(f)), then the photoresist was dissolved in acetone followed by ashing to to remove any remaining residue (Figure 5.7(g)). The palladium and chromium layers were sputter etched using a reactive ion etcher at low pressure with a mixture of oxygen and argon gases, with the aluminium film acting as a hard mask (Figure 5.7(h)). The argon was included to provide the required sputter component, whilst the oxygen was used to passivate the aluminium surface through the formation of a low sputter yield oxide film. This surface passivation was found to increase the etching selectivity between the palladium and aluminium layers. The electrodes were checked for electrical isolation, then the aluminium hard mask was removed by submerging the wafers in neat 351 photoresist developer for 4 minutes (Figure 5.7(i)).

Figure 5.8 shows two gap regions imaged on an AFM. The electrodes were 2.0 mm

wide with the gap being typically 100 nm to 300 nm long. The electrical resistance between the electrodes was greater than 100 GΩ.

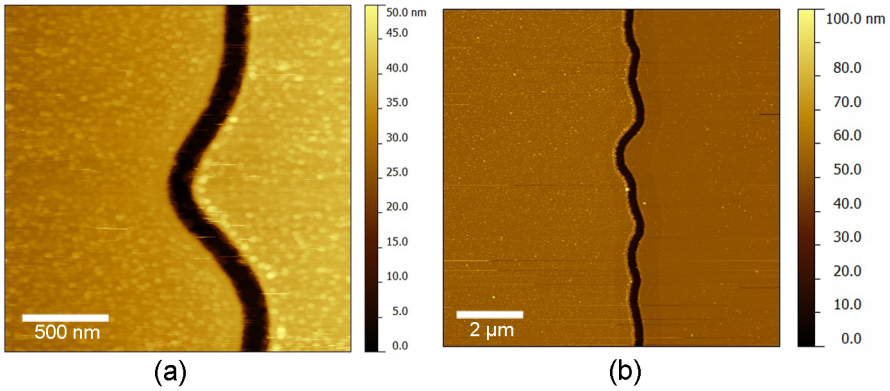

Figure 5.8: *AFM images of completed electrodes showing (a) a fine detail scan and (b) a large area scan of electrodes with a 200 nm gap.*

These palladium sub micron gap electrodes were primarily used for electrical measurements. Following a similar process the same electrode pattern was formed with aluminium and gold. This allowed for measurements on different work function metals to be taken to help understand the importance of the contact to the nanotubes.

5.5.3 Silver Paint Electrodes

For electrical measurements over larger areas (∼1 mm electrode separations and above), electrodes were "painted" on the surface of nanotube films using conductive silver paint (Agar Scientific, Electrodag 1415M). This method of electrode preparation allowed for very quick analysis of films and avoided the need for any harsh chemical treatments which could damage the nanotube films during the photo lithographic process.

5.6 Langmuir-Blodgett Film Deposition

A Molecular Photonics LB715 trough situated in a class 10,000 microelectronics cleanroom was used for recording all surface pressure versus area isotherms and for carrying out Langmuir-Blodgett (LB) deposition. A 3D representation of the trough showing the main trough and two barriers is shown in Figure 5.9. It was necessary to keep the equipment in such an environment to ensure that the water subphase/air interface was as clean and free from residual particles as possible. Before use, the trough and barriers were cleaned thoroughly using propanol to ensure that they were free from contaminants. The subphase used for all experiments was ultra pure de-ionised water at room temperature, $(20 \pm 1)\,^{\circ}\mathrm{C}$ with varying percentages of methanol (Fisher Scientific, analytical reagent grade) added to aid in the dispersion of nanotubes at the air/water interface. The water was purified by reverse osmosis, followed by carbon filtration, two stage de-ionisation and UV sterilisation.

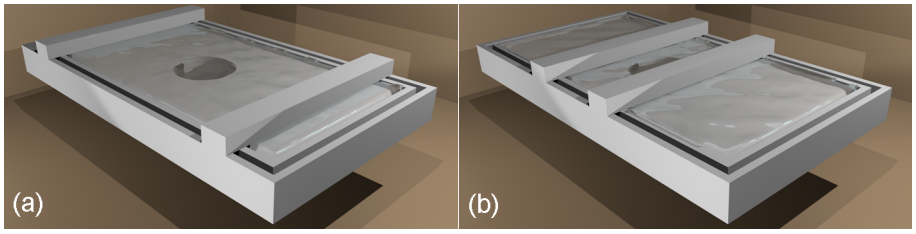

Figure 5.9: *Three dimensional representation of a Langmuir-Blodgett trough, showing the barriers (a) expanded and (b) compressed.*

The surface of the subphase was cleaned with a glass capillary tube attached to a suction pump to remove any traces of dust and any surface active contaminants. Nanotubes were then dispersed from suspension on to the surface of the water using a syringe. The trough was then left for 10 min to allow the solvent (chloroform) to evaporate, leaving just a thin layer of the nanotubes floating on the surface. A surface pressure versus area isotherm was measured by compressing the floating layer with the barriers (Figure 5.9(a) shows the barriers fully expanded and Figure 5.9(b) fully compressed). This allowed observation of the structure of the floating

layer and any changes associated with the transitions from gaseous to expanded to condensed phases as the floating layer became more organised. From the isotherm, a suitable pressure was chosen to perform LB deposition, usually at a point in the condensed phase where the floating layer was in its most orderly state.

For Langmuir-Blodgett deposition, a floating layer was prepared in the same manner as for recording a surface pressure isotherm, and a suitable substrate (usually glass for this work, see Section 5.2 for details) was mounted on the dipping arm. A control pressure was chosen and programmed into the software so that the pressure would be maintained throughout the dipping cycle. Other parameters such as dipping speed, dipper depth and number of cycles could be set before deposition was performed. For this work, a cycle refers to one complete downwards and upwards movement of the substrate through the air/water interface. Figure 5.10 shows a three dimensional representation of this process, with the barriers holding a constant control pressure, and the dipping arm at the three main positions during a cycle (a) entry, (b) bottom and (c) fully withdrawn.

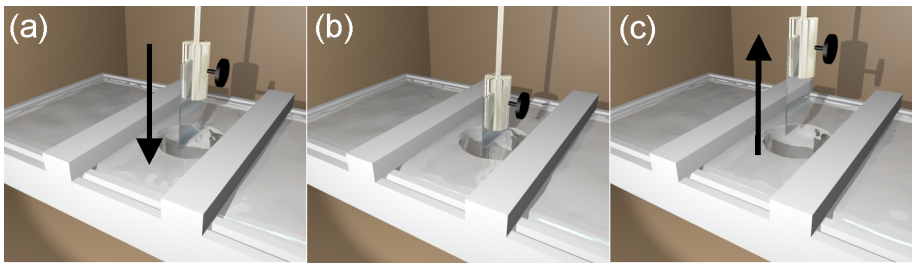

Figure 5.10: *Three dimensional representation of Langmuir-Blodgett deposition, showing the dipping arm at (a) entry, (b) bottom and (c) fully withdrawn. The arrow represents the direction of motion of the dipping arm.*

5.6.1 Alignment with Electric Field

Alternating current electric fields were applied to electrodes during LB deposition using a Farnell LFP1 sinewave oscillator and a Thurlby Thandar instruments WA301 wideband amplifier. The current flowing between the electrodes during deposition

was measured using a Picoscope ADC-100. Wires were connected to suitable linear electrodes using silver paint and held in place using epoxy resin.

5.7 Characterisation Techniques

Various techniques were implemented in studying the morphology, optical and electrical properties of the SWCNT networks. This section will outline the key equipment used.

5.7.1 Atomic Force Microscopy

Basic Operation

Atomic force microscopy (AFM) is a high-resolution form of scanning probe microscopy with the ability to image down to nanometre scale features. The main components of an AFM are the probe, scanner and laser/detector assembly as shown in Figure 5.11. The probe is located at the end of a cantilever and takes the form of a sharp tip (with a radius of curvature on the order of nanometres). Forces between

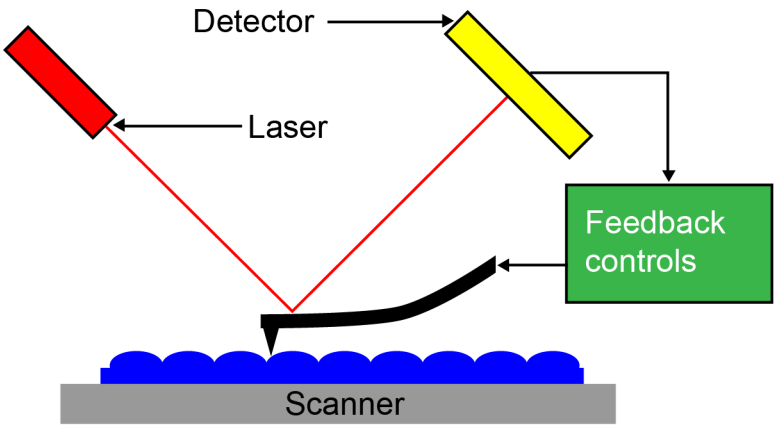

Figure 5.11: *Schematic of a typical atomic force microscope, adapted from [7].*

the tip and the sample surface cause the cantilever to deflect. A laser beam is reflected from the cantilever onto a position-sensitive-photo-detector. The change in light intensity across the photo-detector is fed back to the scanner to maintain constant deflection of the cantilever. Computer software generates a map of the surface topography. Contact mode AFM was performed with a Digital Instruments Nanoscope E scanning probe microscope, and tapping mode AFM was performed with a Digital Instruments NanoMan II scanning probe microscope.

Modes of Operation

In this work two different AFMs were used, one operating in contact mode and one operating in tapping mode. In contact mode (illustrated in Figure 5.11) the force between the tip and the sample surface is kept constant during scanning by maintaining a constant deflection as the probe is scanned across the surface of the sample. The tip deflection is used as the feedback signal. Measurement in this mode can result in material being dragged across the sample if it attaches to the tip making imaging difficult for "loose" materials. In tapping mode, the tip of the cantilever is not held in constant contact with the substrate. Instead it is oscillated at a frequency just above its resonant frequency to scan across the surface. Interactions with forces at the surface of the sample lower this amplitude. A feedback loop system maintains a constant oscillation amplitude by changing the sample-to-tip distance. The distance at each point is used to generate a topographic map of the surface. Tapping mode AFM has the benefit of not being in constant contact with the sample. This is advantageous with soft or loose samples as material is less likely to be dragged over the surface or become attached to the tip, thus making imaging difficult.

5.7.2 Scanning Electron Microscopy

Scanning electron microscopy (SEM) uses electrons to form an image of the sample surface. A beam of electrons is produced by an electron gun at the top of the microscope. This passes through the microscope (under vacuum) and through various electromagnetic fields and lenses which focus the beam onto the sample. When the beam is incident on the sample, electrons and X-rays are ejected from the surface. These electrons and X-rays are collected by a detector and interpreted by software to produce an image of the sample surface. Figure 5.12 shows a simplified schematic of a SEM. An FEI Helios Nanolab 600 microscope was used to gather the majority of SEM images in this work. This equipment also allowed energy-dispersive X-ray spectroscopy (EDX) to be undertaken on the samples to analyse the elements present in the nanotube films.

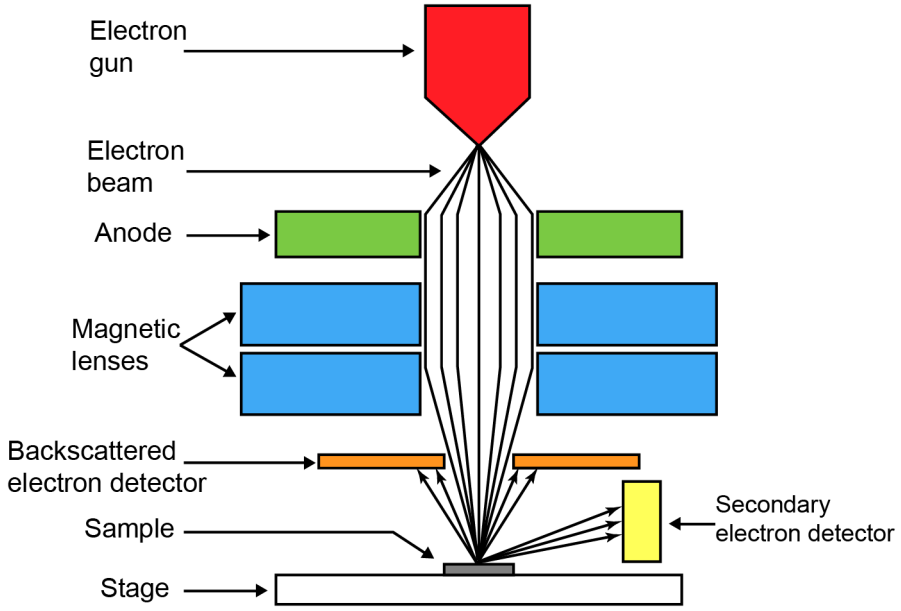

Figure 5.12: *Schematic of a typical scanning electron microscope.*

5.7.3 Ellipsometry

Ellipsometry is an optical technique for measuring various properties of thin films, including the refractive index and thickness. Its main advantages, apart from being a very sensitive technique, are the fact it is contactless so is non-destructive. A typical setup is shown in Figure 5.13. Light is emitted by a source and is linearly polarised before falling on the sample. The light is then reflected and passes through a second polariser (the analyser) and then enters the detector. Light reflected at an angle from a surface has elliptical polarisation. The equipment measures the complex reflectance ratio, which includes an amplitude component and the phase difference. These values cannot, in general, be directly converted into a thickness or refractive index, instead an iterative procedure using the Fresnel equations is used to match thickness and refractive index to the complex reflectance ratio. For this work, a Rudolph Research AutoEL-IV ellipsometer was used to measure the film thickness and refractive index at wavelengths of 632.8 nm, 546.1 nm and 405.0 nm.

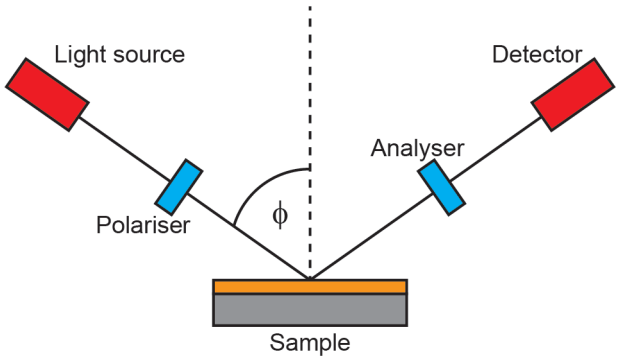

Figure 5.13: *Schematic setup of ellipsometry equipment, adapted from [5].*

5.7.4 Electrical Measurements

Current versus Voltage Measurements

In-plane, direct current (DC) electrical measurements were performed using two-point probe measurements in a screened metal sample chamber. This was connected to a mechanical rotary vane vacuum pump, capable of evacuating the chamber to 10^{-1} mbar. Sample currents were measured over a range of DC voltages using a Keithley 2400 digital sourcemeter.

Current versus Temperature Measurements

Current versus voltage measurements were taken across a range of temperatures (80 - 350 K) in an Oxford Instruments OptistatDN cryostat. Figure 5.14 shows a cross section view of a typical liquid nitrogen cooled cryostat. There is a central sample chamber which is evacuated to a vacuum of less than 10^{-1} mbar. This is then filled

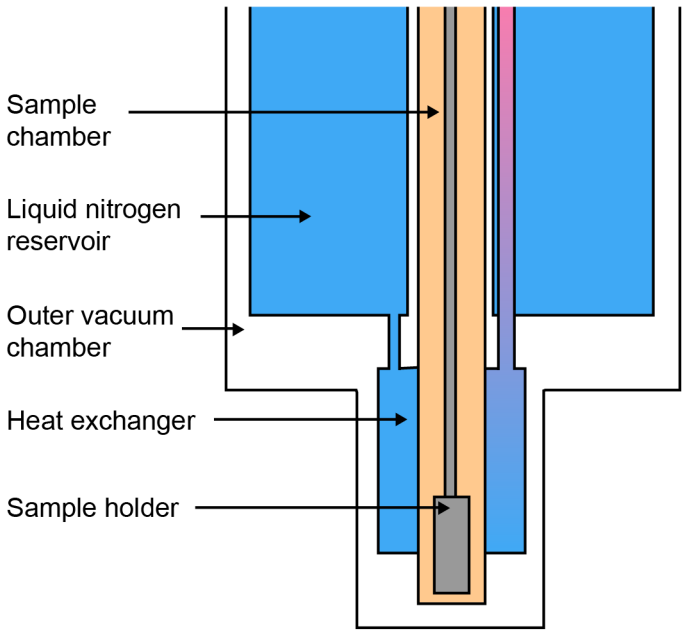

Figure 5.14: *Cross section view of the simplified internal components of a cryostat.*

with helium to act as a transfer gas across the sample chamber to the sample. The sample is held in place by a screw and clamp arrangement and contacts are made between the electrodes on the sample with wires by silver paint. The equipment is set up to allow four wire measurements to account for any change in resistance of the wires with temperature. A liquid nitrogen reservoir feeds a heat exchanger which is controlled by an Oxford Instruments ITC 5035 temperature controller.

A Keithley 2635A sourcemeter was used to log the *IV* data using LabView based software that controlled both the cryostat and sourcemeter.

5.7.5 Optical Absorption

Ultraviolet-visible spectroscopy (UV-Vis) is a form of absorption spectroscopy in the ultraviolet-visible spectral region. Figure 5.15 shows a diagram of a typical set up for double-beam measurements. In this type of spectrometer the light is split into two

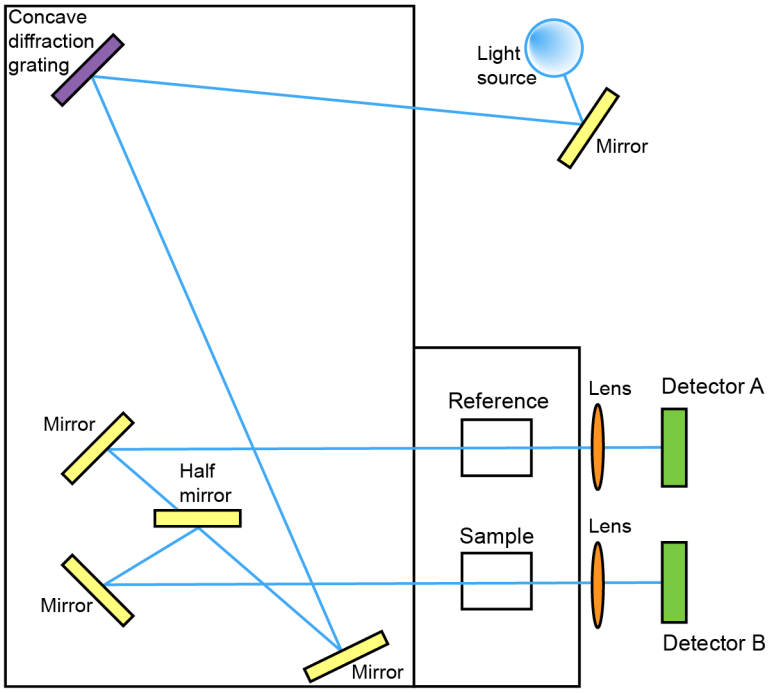

Figure 5.15: *Simplified diagram showing the internal components of a UV-VIS-NIR spectrometer.*

beams before it reaches the sample. One beam passes through a reference (this is taken as 100% transmission) with the other passing through the sample. The ratio of the two transmissions is then compared by the software and the absorbance and/or transmission is plotted versus the wavelength. Optical spectroscopy was performed on the SWCNT solutions as well as films deposited on glass. A Shimadzu UV 3600 spectrophotometer was used to gather all of the optical absorption data.

5.7.6 Contact Angle

Contact angle measurements were made with a Vickers optical microscope, laid horizontally to allow imaging across the substrate rather than the typical "top-down" approach. A droplet of water was spread from a micro syringe on to the surface of the substrate to be tested. Once focused, a photo was taken and the angle was measured on a computer.

5.8 Conclusions

This chapter presented the main experimental techniques used in this work. A brief overview of substrate preparation, nanotube purification and solution preparation was given. Thin film fabrication techniques, including thermal and electron beam evaporation, sputtering, spin coating and photolithography have been explained along with their application to electrode and device fabrication. The Langmuir-Blodgett deposition technique was outlined and presented as the main method for forming nanotube films in this work. Various characterisation techniques have been introduced, including AFM (contact and non-contact modes), SEM and ellipsometry. Optical absorption measuring equipment was also described. The operation of a cryostat for detailed low temperature electrical measurements was explained, including details of the electrical instrumentation.

References

[1] D. R. Knapp, *Handbook of analytical derivation and reactions.* Wiley, 1979.

[2] R. Saito, G. Dresselhaus, and M. S. Dresselhaus, *Physical properties of carbon nanotubes.* Imperial College Press, 1998.

[3] Nanointegris Inc., "Technical specifications sheet," Dec 2012. `http://www.nanointegris.com/skin/frontend/default/nano/downloads/Carbon%20Nanotubes%20Technical%20Data%20Sheet.pdf`.

[4] Nanointegris Inc., "Graphene technical specifications sheet," Dec. 2012.

[5] M. C. Petty, *Molecular electronics: From principles to practice.* Wiley, 2007.

[6] M. C. Rosamond, A. J. Gallant, M. C. Petty, O. Kolosov, and D. A. Zeze, "A versatile nanopatterning technique based on controlled undercutting and liftoff," *Adv. Mater.*, vol. 23, no. 43, pp. 5039–5044, 2011.

[7] K. S. Birdi, *Scanning probe microscopes: Applications in science and technology.* CRC Press, 2003.

Chapter 6

Langmuir-Blodgett Networks of Single-Walled Carbon Nanotubes

6.1 Introduction

This section looks at the preparation of single-walled carbon nanotube (SWCNT) thin film networks using the Langmuir-Blodgett (LB) deposition method. Different sources and purification methods are investigated in order to get the best possible transfer of material onto the substrates. The addition of methanol to the subphase to improve floating layer formation and film deposition is also investigated. To exploit the electrical properties of nanotubes, separated semiconducting and metallic materials were purchased to allow for more control over the electrical behaviour of the films. The advantages and disadvantages of the different materials from a deposition point of view are discussed in this chapter. The hydrophobicity of the films is investigated and this is related to the coverage of nanotubes in the thin films. More detailed analysis of the structure and electrical characteristics of the films will be given in Chapter 7.

6.2 Unsorted HiPCO Material

6.2.1 Non-annealed Material, SWCNT-U

A typical surface pressure versus area isotherm is shown in Figure 6.1. The isotherm is featureless showing a steady increase in surface pressure from 5 mN/m up to a maximum pressure of 28 mN/m as the floating layer is compressed from 80 cm^2 to 20 cm^2. This suggests that there is no significant order in the floating layer. This is to be expected, as the nanotubes are well known to exist as bundles or 'ropes' in solution [1] so are not able to pack tightly together. There is also some hysteresis evident with the pressure at the end of the cycle being slightly lower than the starting pressure. This is likely due to reorganisation of the nanotubes at the air/water interface or loss of some material into the subphase. Using this graph, as well as other trial experimental data, a constant pressure of 25 mN/m in the steepest region of the isotherm, was chosen to perform LB deposition.

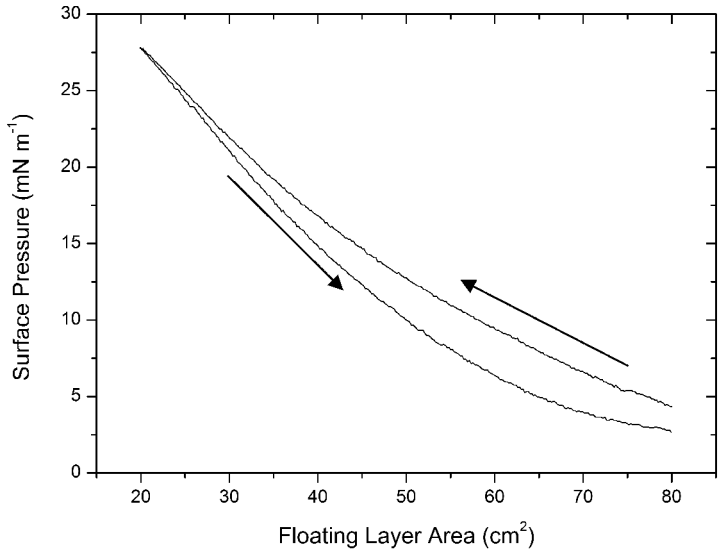

Figure 6.1: *Surface pressure versus area isotherm for 0.1 ml of SWCNT-U solution on a pure water subphase (pH 5.8 ± 0.1, temperature (20 ± 1)°C, barrier compression speed 0.5 mm/s).*

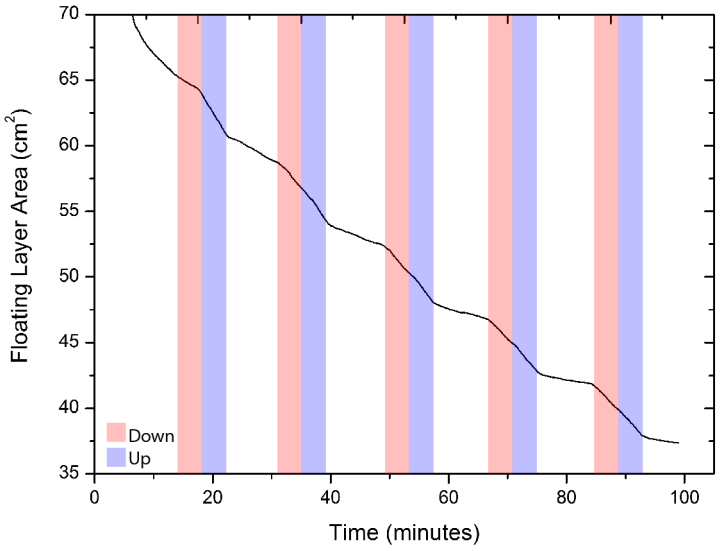

Figure 6.2: *Area versus time deposition record for 5 LB cycles of SWCNT-U onto hydrophilic glass. The floating layer was formed from 0.4 ml of SWCNT-U solution, and held at a constant pressure of 25 mN/m. The shading indicates the motion of the substrate through the floating layer.*

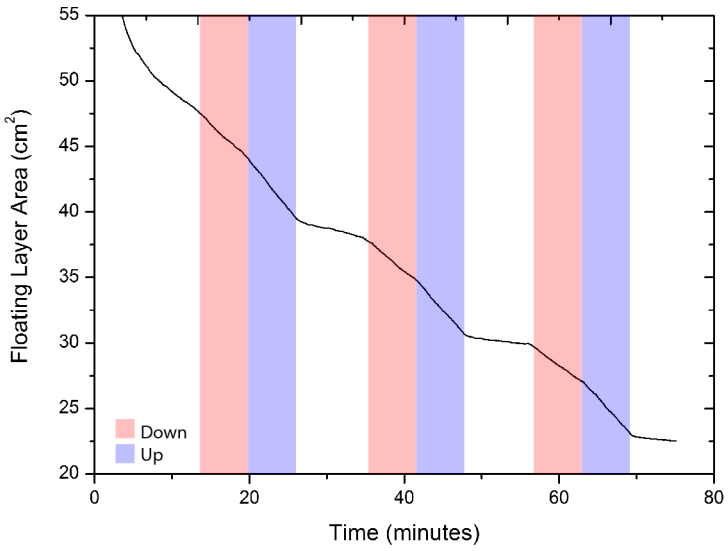

Figure 6.3: *Area versus time deposition record for 3 LB cycles of SWCNT-U onto hydrophobic glass. The floating layer was formed from 0.2 ml of SWCNT-U solution, held at a constant pressure of 25 mN/m. The shading indicates the motion of the substrate through the floating layer.*

Figure 6.2 shows a typical deposition record for SWCNT-U onto an untreated (hydrophilic) glass substrate, over 5 LB cycles. Deposition was performed as described in Section 5.6. The SWCNT-U follow Y-type deposition on hydrophilic glass, where the first layer is transferred as the substrate is withdrawn through the floating layer, then a further layer is picked up on each subsequent pass through the air/water interface. The transfer ratio for the first layer was high at 0.95 showing good transfer. On subsequent layers, the ratio was lower, around 0.7.

On hydrophobic glass, the nanotubes again show Y-type deposition with material being transferred on the first down-stroke through the floating layer. A layer of material is then transferred on each subsequent pass through the air/water interface, shown in Figure 6.3. The transfer ratio after the first two layers was slightly higher than that for the hydrophilic glass with values up to 0.9. It is expected that nanotubes should transfer more readily to a hydrophobic substrate, since the nanotubes themselves are highly hydrophobic. This is supported by the improved transfer ratio.

Figure 6.4 shows a transmission electron microscope (TEM) image of 3 LB layers

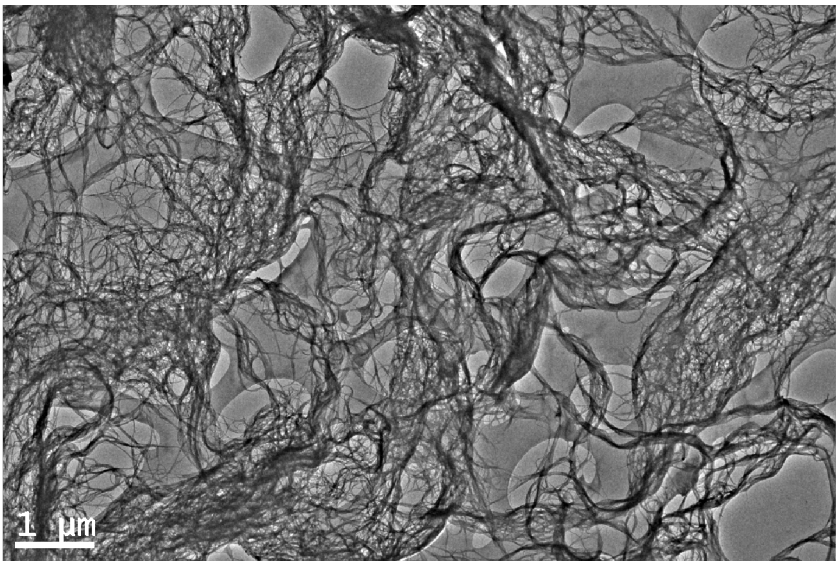

Figure 6.4: *TEM image of 3 LB layers of SWCNT-U transferred to an amorphous carbon grid.*

of SWCNT-U transferred to an amorphous carbon grid to allow imaging in the microscope. Bundles of nanotubes are clearly present showing that film transfer was obtained during deposition. Despite the successful transfer, the coverage is sparse with many gaps present in the film. This supports the observation made from the isotherms that films formed on the water surface are not continuous. A result of this is that multiple layers of nanotubes are likely to build up in density rather than overall thickness, particularly for a small number of dipping cycles. This is discussed further and related to the optical transmission in Section 7.2.1.

6.2.2 Annealed Material, SWCNT-U_a

As outlined in Section 5.3.1, a second solution of SWCNTs was made up with material having an extra annealing step in the purification process, referred to as SWCNT-U_a. The pressure versus area isotherm for this material is shown in Figure 6.5. There is much more structure to the isotherm than for the non-annealed

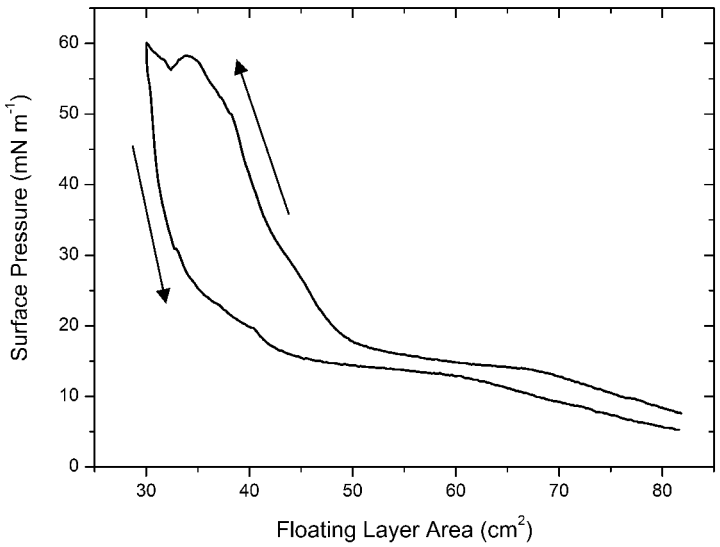

Figure 6.5: *Surface pressure versus area isotherm for 0.1 ml of SWCNT-U_a solution on a pure water subphase (pH 5.8 ± 0.1, temperature (20 ± 1)°C, barrier compression speed 0.5 mm/s).*

nanotubes (Figure 6.1) with an increasing surface pressure as the layer is compressed from 83 cm^2 to 67 cm^2, then a plateau region at around 15 mN/m. There is then a transition into a condensed region with a rapid increase in surface pressure up to a maximum of 58 mN/m. This is followed by a slight dip in pressure at an area of about 34 cm^2, most likely caused by a partial collapse in the structure of the floating layer, either by nanotubes sliding on top of each other, or by loss of material into the subphase (observed by small grey deposits in the bottom of the trough). A maximum pressure of 60 mN/m is recorded at the minimum trough area before the floating layer area is increased again. There is noticeable hysteresis as the area is increased with a significant offset (of around 5 mN/m) in final pressure relative to the starting pressure. As with Figure 6.1 for the non-annealed tubes, this decrease in surface pressure could be attributed to a loss of material into the subphase or the result of a more tightly packed, orderly film occupying less space on the surface causing a lower surface pressure.

The behaviour of the annealed nanotubes is more comparable to what is expected for a fatty acid, i.e. an expanded, then condensed region, suggesting that the annealed nanotubes produced a more organised film on the surface of the water. The heat treatment of the nanotubes is likely to have formed carboxylic acid groups on the surface of the carbon. It is known that the formation of such groups on the surface of nanotubes results in a less hydrophobic material, aiding solubility [2]. It is also likely that the hydrophilic acid groups aid in dispersion of the nanotubes on the water surface.

Figure 6.6 shows a floating layer area versus time deposition record for annealed SWCNTs on hydrophilic glass. The substrate first passes through the air/water interface at around 18 min. As can be seen from the graph, there is no reduction in the floating layer area (apart from the slight decrease present before the substrate is lowered) until it begins its upward stroke through the air/water interface. Although only one LB cycle is shown in the graph, Y-type deposition was observed for

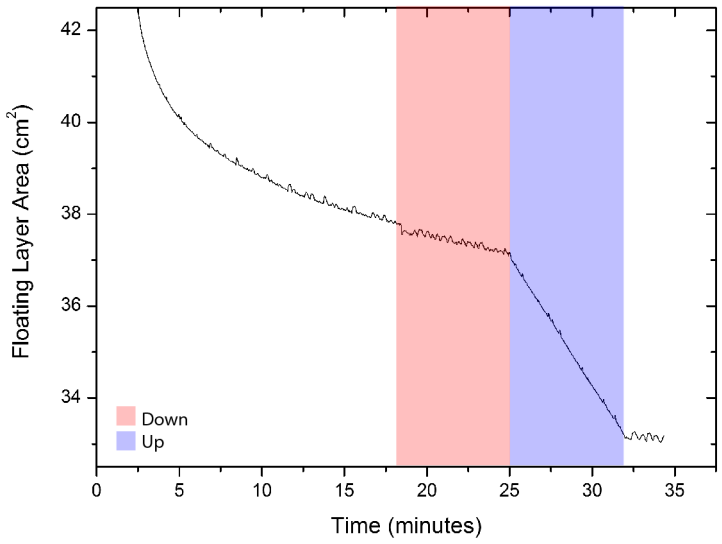

Figure 6.6: *Area versus time deposition record for 1 LB cycle of SWCNT-U_a onto hydrophilic glass. The floating layer was formed from 0.4 ml of SWCNT-U_a solution and was held at a constant pressure of 40 mN/m. The shading indicates the motion of the substrate through the floating layer.*

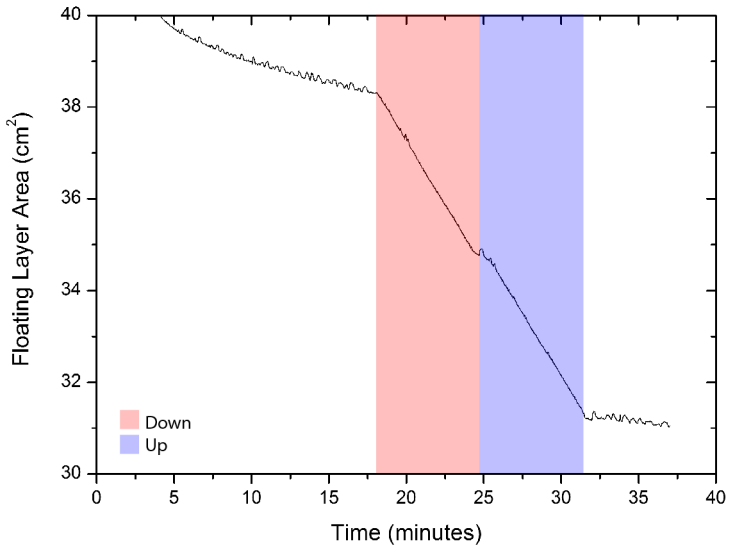

Figure 6.7: *Area versus time deposition record for 1 LB cycle of SWCNT-U_a onto hydrophobic glass. The floating layer was formed from 0.4 ml of SWCNT-U_a solution and was held at a constant pressure of 40 mN/m. The shading indicates the motion of the substrate through the floating layer.*

multiple cycles. The transfer ratio for the single layer shown in Figure 6.6 was 1.06, suggesting excellent transfer. The transfer ratio being above unity simply reflects the unstable nature of nanotubes compared with classical LB materials, however the sharp transition upon withdrawal from the subphase back to a level gradient suggests that the floating layer has stabilised. As with the non-annealed nanotubes, the behaviour was different when deposited on a hydrophobic substrate. Transfer occurred on the first downstroke as well as the first upstroke, following typical Y-type deposition on a hydrophobic substrate. Figure 6.7 shows the first cycle for deposition on hydrophobic glass. The first entry is at about 18 min and the bottom point is reached at around 24 min. The transfer ratio is good on each layer, showing a value of 1.06 for the first layer and 0.94 for the second layer. The slight reduction of the transfer ratio for the second layer more than likely represents the stabilisation of the floating layer following the first traverse through the air/water interface.

6.2.3 Alignment using Electric Fields

Alignment of nanotubes is a well-researched topic with various methods being reported for alignment during the growth process [3, 4]. The techniques have included manipulation during deposition from solution in electric fields [5, 6], in polymers by magnetic fields [7] or by mechanical means following deposition/growth [8]. There are reports of alignment of carbon nanotubes during LB deposition [9, 10, 11] and this will also be discussed later (see Section 7.4). This section briefly describes some initial results incorporating alignment of SWCNTs on linear electrodes with an AC field applied to the electrodes during deposition. The equipment used is described in Section 5.6.1 and LB deposition was performed in the same way as for all other experiments. A 5 V pk-pk 1 kHz AC voltage was used for the results presented here.

Figure 6.8(a) shows the floating layer area versus time dipping record over three LB

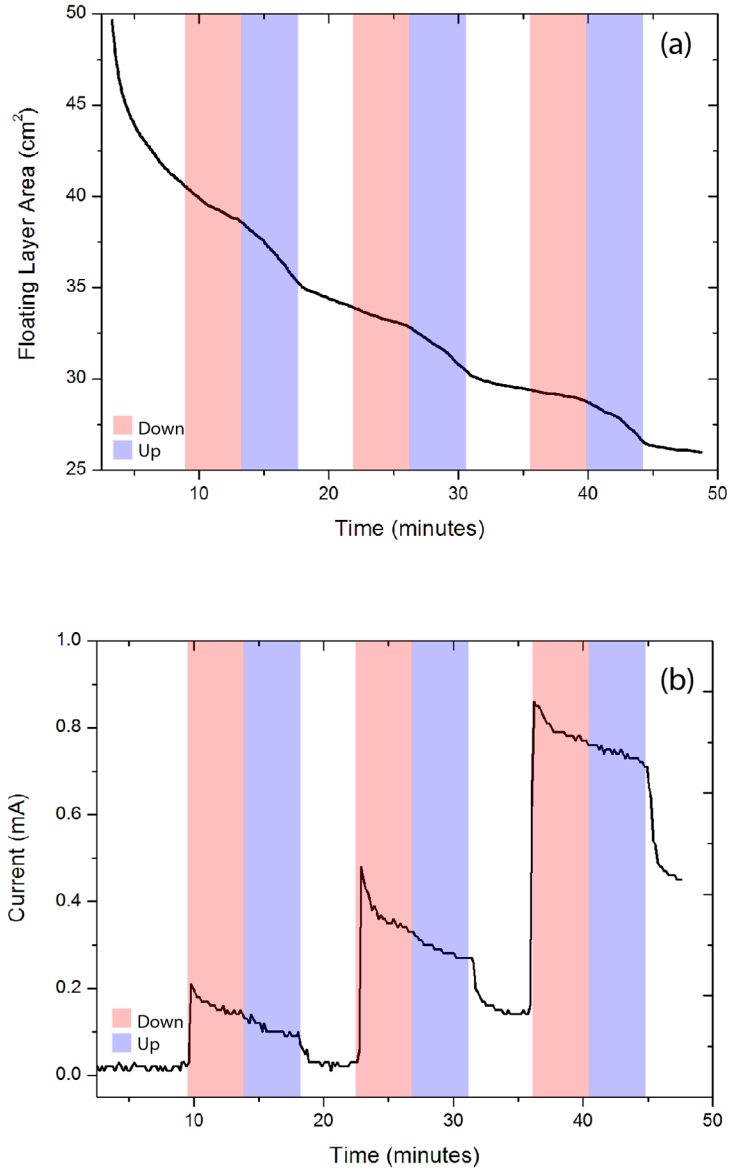

Figure 6.8: *Alignment of SWCNT-U by the application of a 5 V pk-pk 10 kHz AC field (a) area versus time record and (b) the current between the electrodes.*

cycles for SWCNT-U deposited on glass with linear electrodes (separation of 10 µm). Good film transfer is observed with pickup being apparent on each upstroke, transfer ratios were in the range of 0.77 to 0.96. In Figure 6.8(b) the current between the electrodes versus time is plotted. Both graphs show the relevant up and down motion of the dipping arm with the red shading indicating the downstroke and the blue shading representing the upstroke. As the substrate passes through the

floating layer for the first time at ∼9 min there is a peak in the current between the electrodes of about 0.2 mA followed by a gradual decrease until the substrate is withdrawn from the floating layer at ∼18 min, where the current drops to only slightly above the starting value. At the start of the next LB cycle, there is another peak in the current followed by a gradual decrease until the substrate is withdrawn. This time the current drops again, but remains at a constant level of around 0.15 mA whilst the substrate is in air showing that material has been permanently transferred to the substrate. The final LB cycle shows the same pattern again and this time a much higher residual current of about 0.45 mA is observed. The reduction in current as the substrate is withdrawn is almost certainly due to the electrodes losing contact with the material in the floating layer which would have been adding to the conductivity measured. The gradual decrease in current over each dipping cycle could be caused by the nanotubes being destroyed through Joule heating due to high power dissipation across the bundles. This has been reported by others as a mechanism for the breakdown of nanotubes with high power dissipation [12, 13, 14]. The ultra pure water used in the subphase typically has a resistivity of around 18 MΩ/cm. Even across the small electrode separations used for these experiments any current passing through the water will be small in magnitude compared to the current passing through the nanotube film.

Although there is no direct evidence from this work that the AC electric fields caused alignment during deposition, there is AFM evidence that suggests the nanotubes are attracted more strongly to the electrodes with an applied field. Figure 6.9(a) shows a typical 10 µm electrode gap with no film, (b) shows another typical electrode gap with a 5 layer LB film with no applied field during deposition, note how little material is present. In the third image (c) a ±5 V, 1 kHz sine wave was applied across the electrode gap during deposition of 5 layers of nanotubes. There is a significant increase in the amount of material present between the electrodes with the applied electric field. It has been suggested by others that a possible mechanism for this

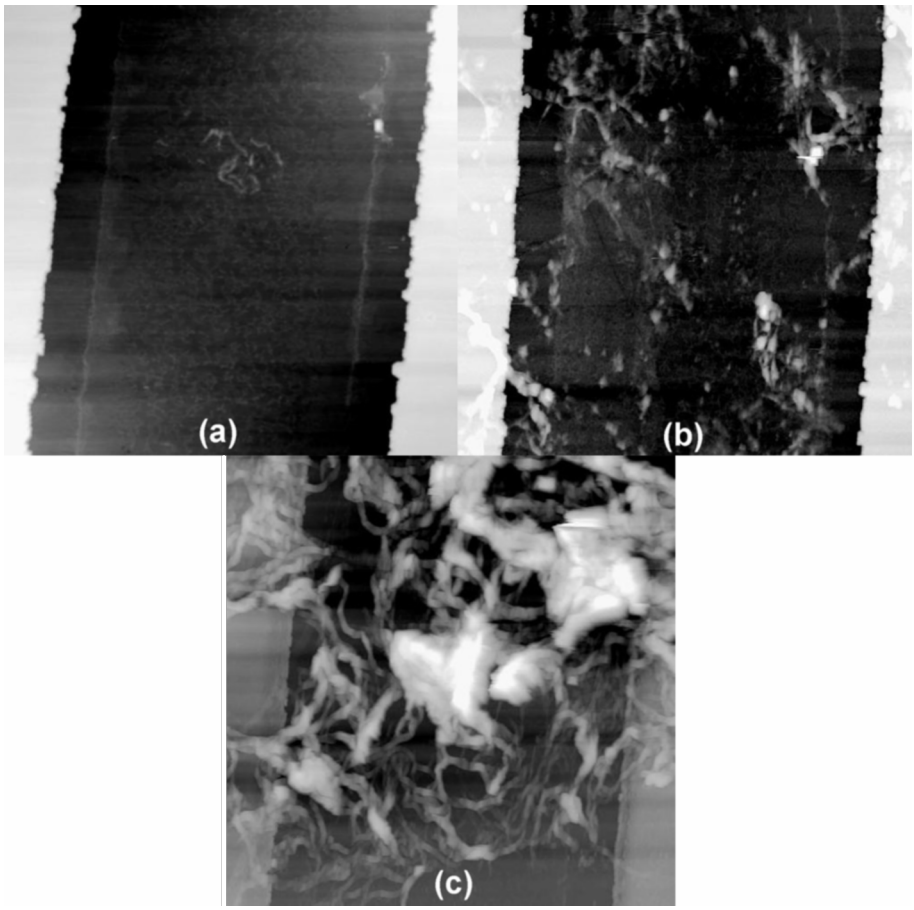

Figure 6.9: *AFM images showing a) No film, b) LB film (5 layers) with no applied voltage, c) LB film (5 layers) with AC voltage (±5 V, 1 kHz sine wave) applied, all on a 10 μm electrode gap.*

alignment is dielectrophoresis [15]. Only limited data have been gathered for these experiments, however the results presented here show promise for follow up work.

6.3 Arc Discharge Sorted Material

This section highlights the floating layer formation and deposition of arc discharge produced SWCNTs that have been sorted into semiconducting and metallic material (see Section 5.3.2 for details on solution preparation). It also looks into the effects of adding methanol into the subphase to aid in floating layer formation and with transfer to the substrate during deposition. This material was used for the majority of the work presented later in this thesis.

6.3.1 Pure Water Subphase

Semiconducting SWCNTs (SWCNT-S)

A series of surface pressure versus area isotherms are shown in Figure 6.10 for sorted semiconducting SWCNTs (SWCNT-S). The different curves represent different volumes of material spread on the water subphase. The solution was made to a concentration of 0.02 mg/ml as described in Section 5.3.2. If the 0.02 ml isotherm is taken as an example, the initial pressure of roughly 9 mN/m with the barriers fully expanded shows the presence of a layer of material before further compression. As the trough area is decreased, there is a gradual increase in surface pressure up to 17 mN/m showing order in the floating layer. When the floating layer is expanded again there is some hysteresis, with the pressure at maximum trough area now being 8 mN/m. However, this hysteresis effect is much less pronounced than for the unsorted HiPCO material (Figure 6.1 and 6.5).

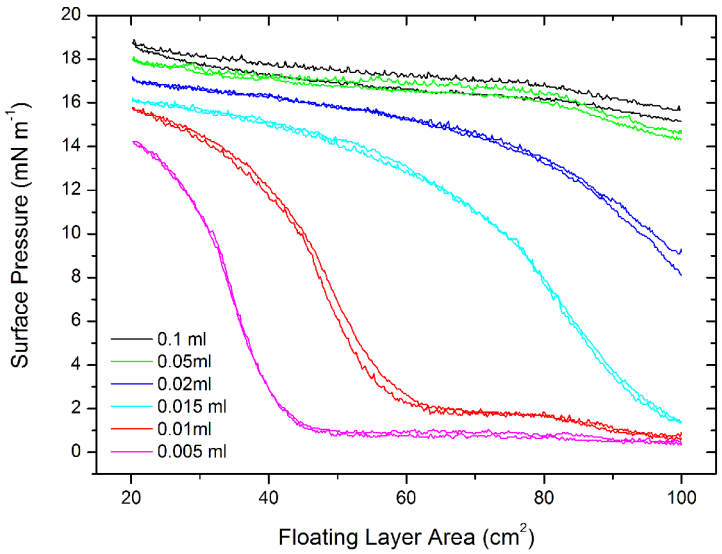

Figure 6.10: *Surface pressure versus area isotherms for varying volumes of SWCNT-S solution on a pure water subphase (pH 5.8 ± 0.1, temperature (20 ± 1)°C, barrier compression speed 0.5 mm/s).*

For the larger volumes of material (0.05 ml and 0.1 ml) there is little difference between the isotherms, suggesting that the maximum amount of material in a single floating layer has been reached. The extra material must either be forming multiple layers by overlapping as it is compressed, or is being lost into the subphase resulting in very little change in surface pressure. It is also possible that by using more starting material, the aggregation of nanotubes on the surface is increased resulting in larger bundles, which are less able to organise and pack tightly together on the surface. This could give rise to the featureless isotherm. When the amount of material spread is reduced to 0.015 ml, the starting pressure drops to below 2 mN/m showing an initially expanded phase. As it is compressed, a similar shape in the isotherm is observed as for 0.2 ml of material, with the maximum pressure being around 16 mN/m. Further reductions in the amount of starting material show an initial pressure of below 1 mN/m, suggesting an expanded phase where the nanotubes are very dispersed on the surface with virtually no interaction. There is a slight increase in surface pressure up to a plateau region showing an expanded phase and then a further increase in pressure showing a condensed region. If the isotherms are compared for the cases with 0.01 ml and 0.005 ml it can be seen that the transition point from expanded to condensed is shifted to the left when less material is present, although the basic shape remains the same.

Metallic SWCNTs (SWCNT-M)

As for the semiconducting nanotubes, a similar process of characterising the floating layers through isotherms was carried out for the metallic nanotubes (SWCNT-M). Figure 6.11 shows a series of surface pressure versus area isotherms for SWCNT-M. The different curves represent different volumes of material spread on the surface of the water subphase. In a similar manner to the SWCNT-S material, little hysteresis is observed showing good floating layer stability with little loss into the subphase or overlapping of the material on the water surface.

The effect of amount of SWCNT-M material spread on the subphase is shown in Figure 6.11, this indicates a very similar behaviour to the semiconducting material (Figure 6.10) with 0.05 ml and 0.1 ml of material showing little pressure change due to the high density of the floating layer. Again, when the amount of material is reduced, more features at lower pressure are observed, with the transition point from expanded to condensed phases becoming more pronounced and shifting to the left.

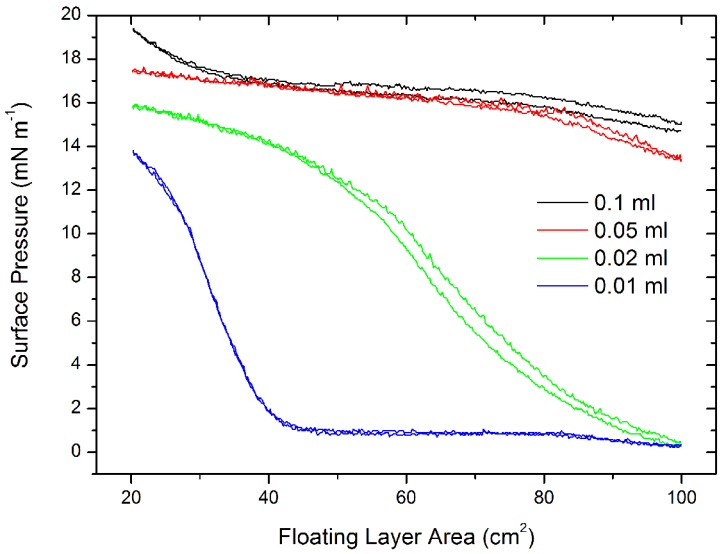

Figure 6.11: *Surface pressure versus area isotherms for varying volumes of SWCNT-M solution on a pure water subphase (pH 5.8 ± 0.1, temperature (20 ± 1)°C, barrier compression speed 0.5 mm/s).*

6.3.2 Methanol Addition to the Subphase

A small percentage of methanol was added to the subphase (as discussed in Section 5.6). This approach has been successfully used to aid in the spreading and LB transfer of phthalocyanine compounds [16]. Figure 6.12 shows four surface pressure versus area isotherms for SWCNT-S with varying percentages (by volume) of methanol in the subphase (0 %, 2 %, 5 % and 10 %). It is noted that with

an increasing amount of methanol in the subphase, the overall surface pressure generated by the floating layer is reduced. With the addition of 2 % methanol, the maximum surface pressure is lowered from 22 mN/m to 18 mN/m. Addition of alcohol to water is known to cause a reduction in its surface tension; the decrease in maximum pressure observed in the nanotube layer is approximately equal to the decrease caused by the addition of methanol. For example, the maximum surface tension of water at 20 °C is 72.75 mN/m. This is lowered to 63.46 mN/m with the addition of 5 % by weight of methanol [17]. The maximum surface pressure falls even further to 13 mN/m when more methanol (5 % by volume) is added. Another effect of adding methanol is shifting the isotherm to the left, when 10 % of methanol is added to the subphase, two distinct phase changes are observed, one at around 85 cm^2 and another at 55 cm^2. It is possible that by reducing the surface tension of the water, the highly hydrophobic nanotubes are repelled less when spread on the water resulting in better dispersed films on a water subphase with methanol added. The isotherm for 10 % methanol shows more structure suggesting order in

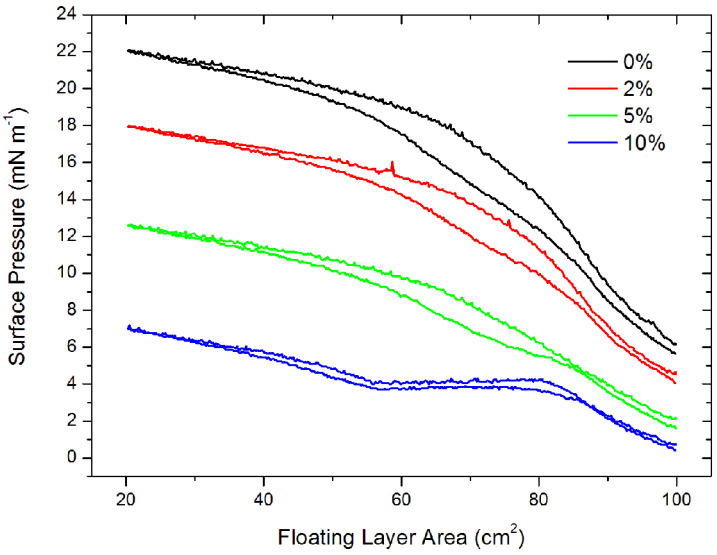

Figure 6.12: *Surface pressure versus area isotherms for 0.1 ml of SWCNT-S solution on a pure water subphase with varying percentages of methanol (temperature (20 ± 1) °C, barrier compression speed 0.5 mm/s).*

the film and with the phase change at $\sim$55 cm^2 a move to a more ordered film at lower floating layer areas.

6.3.3 Generic Isotherm

The previous pages discussed the two different materials used (SWCNT-S and SWCNT-M) and the isotherms formed by each material. The addition of methanol to the subphase, as well as changing the amount of material spread has been shown to affect the isotherms suggesting very different shapes under different conditions. In essence, there is just one shape of surface pressure versus floating layer area isotherm. By varying the amount of material and/or addition of methanol to the subphase different regions are then viewed. Figure 6.13 shows a comparison of the different conditions discussed previously for SWCNT-S on one graph. Although these data are for semiconducting nanotubes, the same general shape applies to the metallic nanotubes.

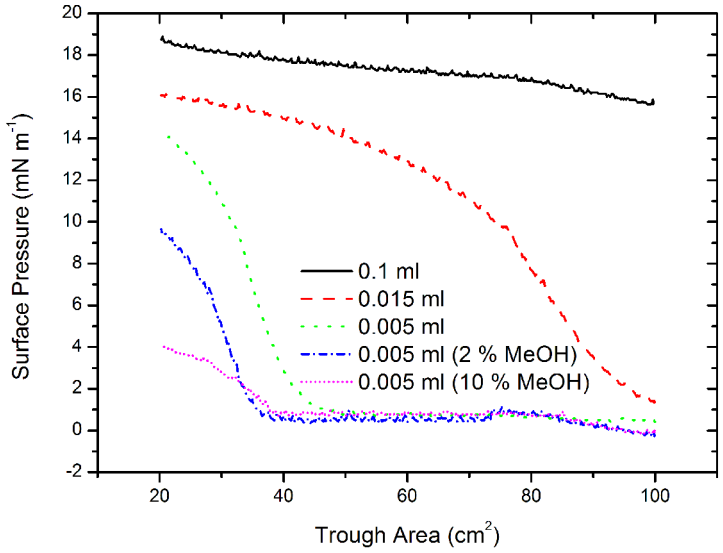

Figure 6.13: *Surface pressure versus area isotherms for SWCNT-S, showing the effect of volume of material and addition of methanol to the subphase.*

The "generic" isotherm is represented by the 0.005 ml curve. This shows an

expanded region up to around 1 mN/m and then a constant pressure plateau. Following this, there is a relatively pronounced transition into a condensed phase, which exhibits an almost linear increase in pressure up to approximately 10 mN/m. This suggests some organisation in the floating layer with the nanotubes (or bundles of nanotubes) packing together on the surface. After this condensed region, there is then a steady increase in surface pressure up to 14 mN/m at which point the minimum trough area is reached. The rate of increase in surface pressure towards the minimum trough area decreases, suggesting that the maximum pressure generated by the nanotube layer has been reached. When a larger amount of material is spread on the subphase (0.015 ml) it initially looks quite different. However, due to the increase in the amount of starting material, the isotherm has simply been shifted to the right. The extended plateau region is no longer present, instead the more organised condensed phase is immediately observed. The rate of surface pressure increase is less rapid than that for the smaller amount of material, possibly due to the formation of larger aggregates on the subphase surface, reducing the ability of the nanotubes to organise and pack tightly on the surface. If an even larger amount of starting material is used (0.1 ml), a significantly higher starting pressure is observed of 16 mN/m, implying that there is already a film of nanotubes covering the surface of the water. As this film is compressed, there is little structure evident in the isotherm and there is no significant increase in surface pressure or identifiable phase changes. The effect of adding methanol to the subphase is also summarised in Figure 6.13. By adding methanol, the overall surface pressure generated by the floating layer is reduced and the isotherm is shifted to the left. The transition point from expanded to condensed regions remains roughly the same, for both 2 % and 10 % addition of methanol suggesting that the size of the nanotube bundles has reached a minimum with the addition of 2 % methanol.

The isotherms show good repeatability for both materials as long as the careful cleaning procedures (outlined in Section 5.6) are followed for the trough and the

nanotubes are effectively dispersed in the spreading solvent through ultrasonication. This repeatability between experiments suggests that the effects observed above are as a result of changing the conditions (i.e. varying the amount of material or composition of the subphase) rather than simply differing results between experiments.

Figure 6.14 shows a representation of what the complete generic isotherm for SWCNT dispensed from solution in chloroform on a pure water subphase would look like. Region (a) starts from a gaseous/expanded phase, then the pressure slowly builds as the floating layer is compressed until it reaches a constant pressure plateau region (b). This section represents re-organisation of the floating layer but no increase in the order of the SWCNTs so no increase in surface pressure. Following this, a region of rapid increase in surface pressure is observed. Region (c) represents this main condensed phase with a steady increase in surface pressure. The final region observed (d) shows a rapid decrease in the rate of increasing surface pressure. In this region the maximum packing density of the SWCNT floating layer has been reached.

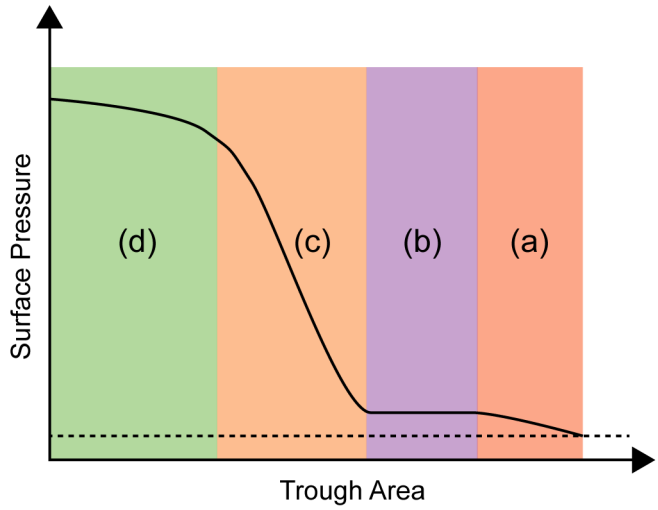

Figure 6.14: *Representation of the complete generic isotherm for SWCNT.*

6.3.4 LB Deposition

Semiconducting SWCNT (SWCNT-S)

Figure 6.15 shows a typical transfer record for SWCNT-S onto a hydrophilic substrate from a pure water subphase. In the first 10 minutes after the control process has been activated, the floating layer is very unstable and represented by the continuous decrease in floating layer area. This downwards trend is continued throughout the experiment, however it is clear where the substrate enters and is withdrawn through the floating layer area (shown on the graph). When the substrate first enters the subphase, there is a slight change in the slope of the curve, but no indication that material is transferred. On the first upstroke there is a noticeable change (at about 16 min) and some material is transferred, with a transfer ratio of about 1.3. This is significantly higher than the expected maximum transfer ratio of 1, which is likely due to the unstable nature of the nanotube film. On each subsequent downstroke there is a loss of material (represented by the increase in floating layer area), however the pickup is still greater so there is a net increase in the amount of material on the substrate. Transfer ratios were about 0.3 to 0.5 on subsequent layers, suggesting (poor) Z-type deposition, with transfer only on the upstroke.

Next, deposition was performed using the optimum conditions. This is shown in Figure 6.16 with a water subphase containing 5 % methanol and 0.3 ml of SWCNT-S solution spread on the surface. This was held at a control pressure of 10 mN/m, corresponding to the linear increase in surface pressure on the isotherm. Three LB deposition cycles were performed at a speed of 0.04 mm/s. The graph shows an unstable layer initially, represented by the steadily decreasing floating layer area. The layer stabilises slightly as the substrate is passed through the floating layer for the first time, however no material is transferred until the substrate is withdrawn.

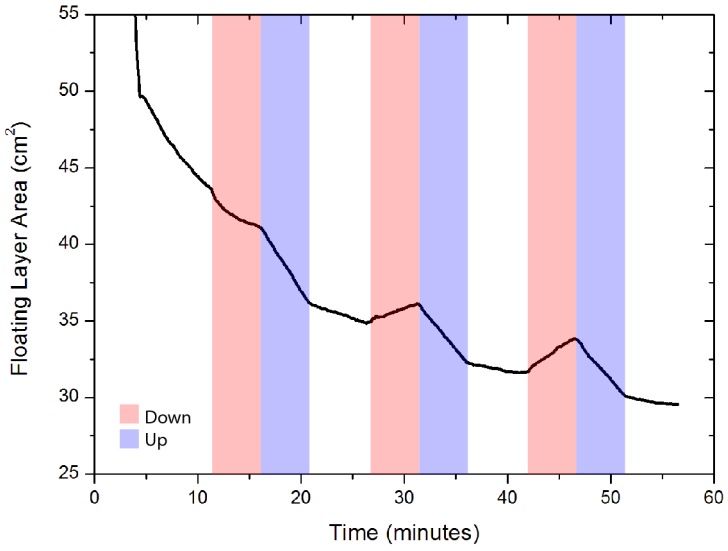

Figure 6.15: *Area versus time deposition record for 3 LB cycles of SWCNT-S onto hydophilic glass with a pure water subphase. The floating layer was formed by spreading 0.2 ml of SWCNT-S solution on a pure water subphase and was held at a constant pressure of 6 mN/m. The shading indicates the motion of the substrate through the floating layer.*

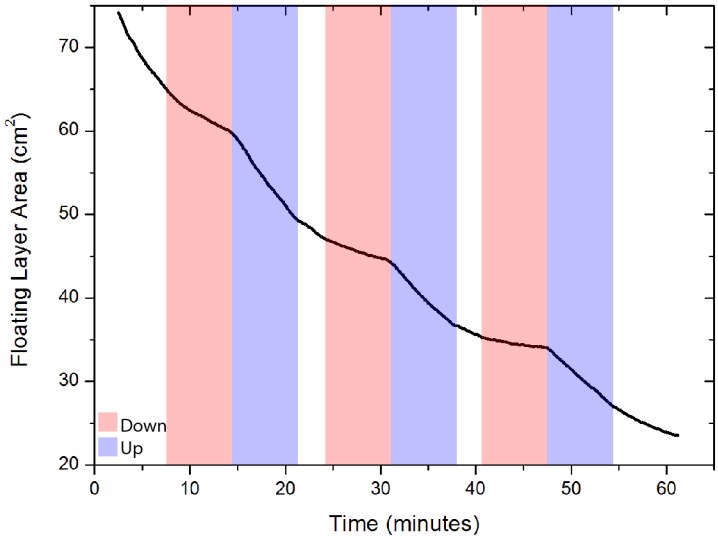

Figure 6.16: *Area versus time deposition record for 3 LB cycles of SWCNT-S onto hydrophilic glass. The floating layer was formed by spreading 0.3 ml of SWCNT-S solution onto a subphase consisting of water containing 5 % methanol and was held at a constant pressure of 10 mN/m. The shading indicates the motion of the substrate through the floating layer.*

The deposition for this material on hydrophilic glass shows Z-type behaviour, with material only being picked up on the upstroke through the air-water interface. If this deposition is compared with the deposition on a pure water subphase (Figure 6.15), then it is clear that the addition of methanol to the subphase has improved the quality of film transfer.

Metallic SWCNT (SWCNT-M)

Metallic nanotubes were also transferred to glass substrates by LB deposition. A control pressure of 15 mN/m was used with the area versus time graph for this experiment being shown in Figure 6.17. The SWCNT-M show a more stable floating layer initially represented by the low gradient of the graph between 5 min to 10 min compared to the SWCNT-S material (Figure 6.15). The first LB cycle shows little pickup on the first downstroke, then good transfer on the upstroke. The layer then appears to collapse as there is a continuous decrease in floating layer area even when the substrate is in the air (between 25 min to 33 min). This collapse is reflected in the transfer ratios which are much greater than unity on the out strokes. The next two LB cycles show similar transfer to the first with material only being transferred on the upstroke.

Methanol was added to the subphase (as with the semiconducting nanotubes) in an attempt to improve film transfer. Figure 6.18 shows the floating layer area versus time graph for this experiment. In the same way as the pure water subphase (Figure 6.17) the floating layer is initially stable, but following the first deposition cycle, the floating layer collapses with no clear transfer being observed throughout the following two LB deposition cycles. Unlike the semiconducting nanotubes, the addition of methanol does not appear to improve film transfer for the metallic nanotubes.

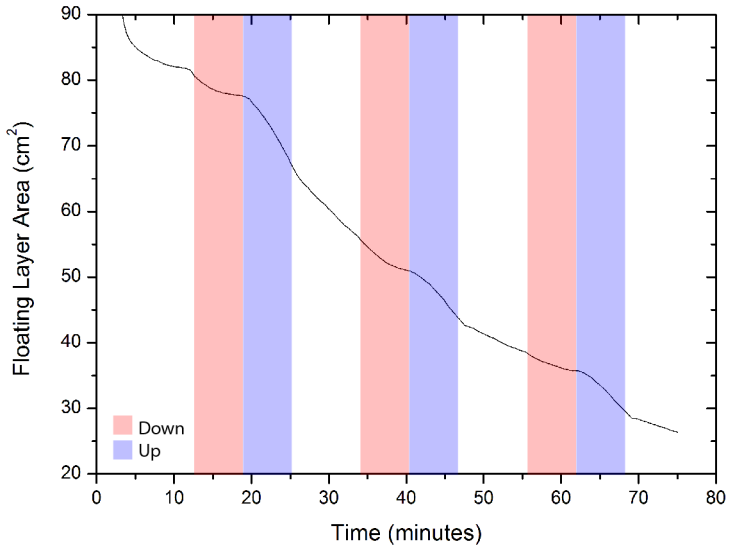

Figure 6.17: *Area versus time deposition record for 3 LB cycles of SWCNT-M onto hydrophilic glass. The floating layer was formed by spreading 0.1 ml of SWCNT-M onto a pure water subphase and was held at a constant pressure of 15 mN/m. The shading indicates the motion of the substrate through the floating layer.*

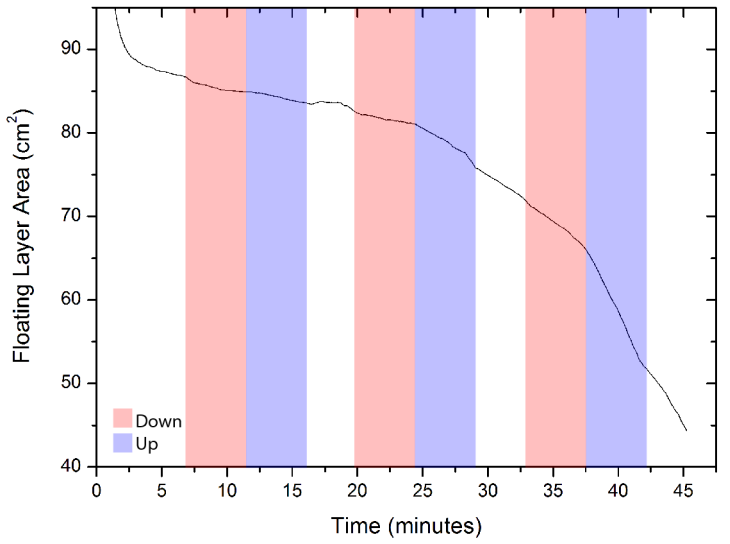

Figure 6.18: *Area versus time deposition record for 3 LB cycles of SWCNT-M onto hydrophilic glass. The floating layer was formed by spreading 0.1 ml of SWCNT-M solution onto a subphase consisting of water containing 5 % methanol and was held at a constant pressure of 8 mN/m. The shading indicates the motion of the substrate through the floating layer.*

6.3.5 Additional Purification

The sorted material showed signs of contamination when deposited on substrates (see Section 7.3.1). The most likely source of this contamination was residual surfactant from the separation process. Following guidance from the suppliers an extra washing step in methanol was introduced before dispersing the material in chloroform.

Pre-Washed Semiconducting SWCNTs (SWCNT-S_w)

Figure 6.19 shows a typical surface pressure versus area isotherm for pre-washed SWCNT-S_w spread on the surface of a 5 % methanol pure water subphase. The isotherm now shows all of the key regions described in the "generic" isotherm for sorted SWCNT materials (Figure 6.14), and a relatively high maximum surface pressure of around 26 mN/m compared with the unwashed materials, where a maximum pressure of only 20 mN/m was observed. Despite the higher pressure, there is also significantly more hysteresis when the area is increased again. If the

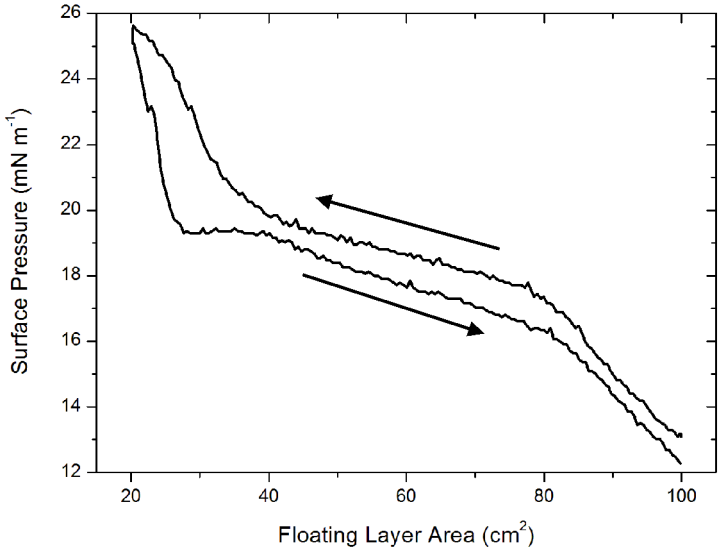

Figure 6.19: *Surface pressure versus area isotherm for 0.2 ml of pre-washed SWCNT-S_w solution spread on a pure water subphase with 5 % methanol (temperature (20 ± 1) °C, barrier compression speed 0.5 mm/s).*

contamination present was indeed a surfactant, then removing it would decrease the stability, possibly accounting for the greater hysteresis.

Pre-Washed Metallic SWCNTs (SWCNT-M_w)

After washing, sharp transitions were observed following the expanded phase into the long plateau region and then a second sharp transition into a condensed region (Figure 6.20). These transitions are similar to the ones observed for the unwashed material, although a higher maximum pressure is observed. Although the isotherm does not appear to be significantly altered by the extra washing step, AFM observations of LB films suggest that the contamination has been removed/reduced (see Section 7.3.1).

This washing step was not pursued any further. To remove the contamination a thermal annealing step (see Section 7.3.1) was introduced after LB deposition to improve the purity and electrical properties of the SWCNT films.

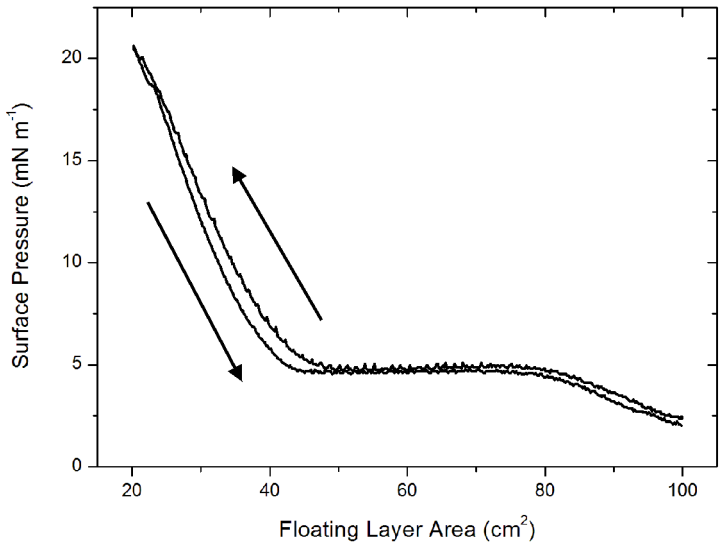

Figure 6.20: *Surface pressure versus area isotherm for 0.5 ml of pre-washed SWCNT-M_w solution spread on a pure water subphase with 5 % methanol (temperature (20 ± 1)°C, barrier compression speed 0.5 mm/s).*

6.4 Surface Hydrophobicity

To investigate the effect nanotube films have on the surface of un-treated (hydrophilic) glass, several samples were prepared with different materials. Figure 6.21 shows a series of photographs taken with an optical microscope (a), the edges

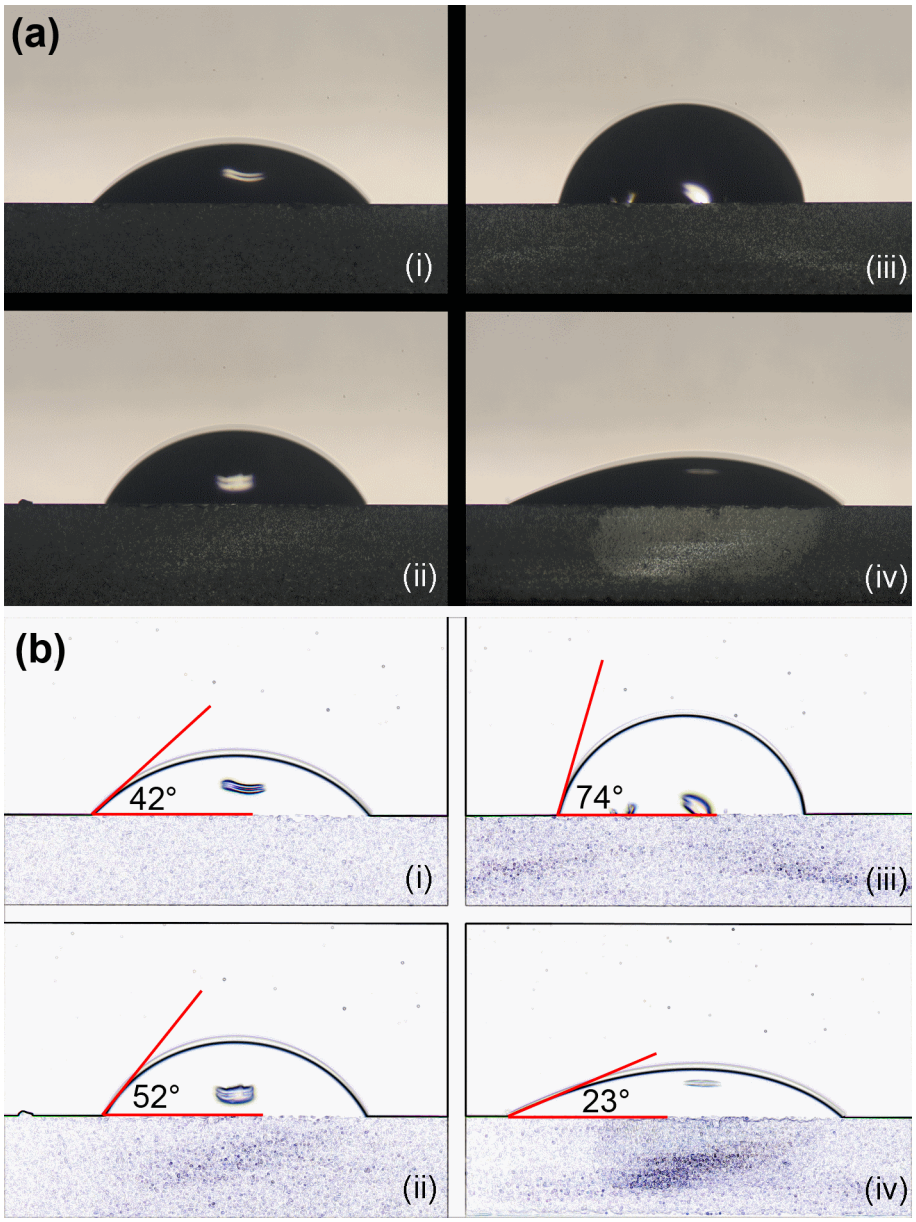

Figure 6.21: *(a) Photographs of water on the surface of various SWCNT films, (b) Edges highlighted to show the contact angle. Different films are represented; (i) 7-layer SWCNT-U, (ii) 2-layer SWCNT-U (filtered), (iii) 7-layer SWCNT-S and (iv) 7-layer SWCNT-M.*

have then been highlighted and the angles measured (b). The experimental set up for this measurement is explained in Section 5.7.6.

Table 6.1 summarises the material and number of layers deposited and the corresponding contact angle. From the results it is initially hard to see a pattern in the change in hydrophobicity. If the two unsorted SWCNT films are compared, the contact angles are similar (within 10°) to each other, however the number of layers transferred is significantly different, with just two layers of the filtered material (ii) increasing the hydrophobic nature of the glass more than 7-layers of the un-filtered solution (i). Similarly, 7-layer films of SWCNT-S (iii) and SWCNT-M (iv) show very different contact angles of 74° and 23° respectively. Initially, it was thought that the different nanotubes exhibited different hydrophobic properties. However a more likely explanation is that these differences are simply related to the quality of film transfer. Section 6.3.4 showed that, in general, SWCNT-S exhibited improved deposition compared with metallic nanotubes. This is reflected in the contact angles. Since more material would have been transferred for the SWCNT-S film, this would increase the hydrophobic nature of the glass more than the thinner/more sparse film of SWCNT-M. Similarly for the filtered and un-filtered material, filtering improved floating layer formation, hence improved deposition so more material would have been transferred despite the lower number of layers compared to the unsorted and un-filtered SWCNTs.

Label	**Material**	**No. of Layers**	**Contact Angle (°)**
(i)	SWCNT-U	7	42
(ii)	SWCNT-U (Filtered)	2	52
(iii)	SWCNT-S	7	74
(iv)	SWCNT-M	7	23

Table 6.1: *Summary of contact angles on hydrophilic glass for different material and number of layers for SWCNT films.*

6.5 Oxidised HiPCO Material

6.5.1 Isotherms

Unsorted HiPCO nanotubes were oxidised in HNO_3 to introduce carboxylic acid groups onto the surface of the nanotubes (Section 5.3.3). This is reported to improve dispersion of carbon nanotubes in solution [18]. Therefore, it was hoped that improved dispersion of SWCNTs in solution would aid LB deposition. Figure 6.22 shows a series of area versus surface pressure isotherms with varying amounts of material for oxidised single-walled carbon nanotubes (SWCNT-O). The isotherms show similar features to the arc discharge semiconducting and metallic material (Figure 6.10 and Figure 6.11 respectively). However, a key difference for the oxidised material is more pronounced transition points. The isotherm representing the least amount of material (0.025 ml) shows a long plateau region and then a sharp transition into a condensed phase at $35\,cm^2$. When more material is added

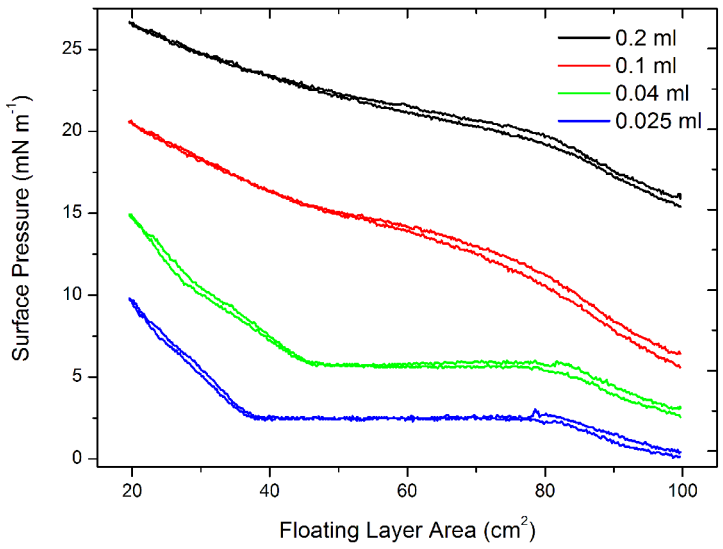

Figure 6.22: *Surface pressure versus area isotherm for varying volumes of SWCNT-O solution on a pure water subphase (pH 5.8 ± 0.1, temperature 20 ± 1 °C), barrier compression speed 0.5 mm/s.*

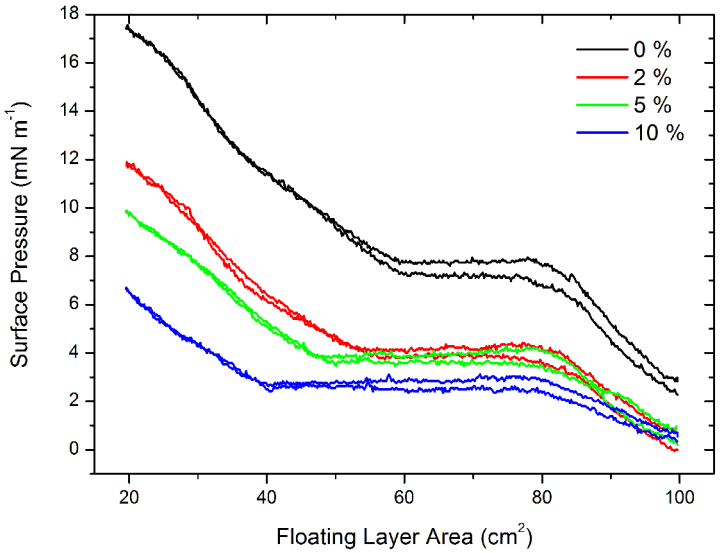

Figure 6.23: *Surface pressure versus area isotherms for 0.04 ml of SWCNT-O solution on a pure water subphase with varying percentages of methanol (temperature (20 ± 1)°C, barrier compression speed 0.5 mm/s).*

(0.04 ml) the plateau region and initial pressure are shifted up by around 3 mN/m suggesting that as soon as the material is spread there is a continuous film present on the surface giving rise to the increased surface pressure. The transition point into the condensed region was also shifted to the right, suggesting a larger "molecule per unit area value", perhaps caused by the material being more likely to group together when larger amounts are present on the surface. The 0.04 mN/m curve also shows the presence of a second condensed region, represented by the change in gradient at 28 cm^2. When more material is added (0.1 ml and 0.2 ml) much greater starting pressures are observed particularly for the latter. The initial pressure of 16 mN/m when 0.2 ml of material is spread suggests the presence of a dense film on the surface and with only a steady increase in surface pressure up to the maximum of 26 mN/m, suggesting that the nanotubes are already ordered on the surface.

These isotherms, in particular the one representing 0.04 ml, suggest that introducing carboxylic acid groups onto the surface of the nanotube indeed aids in floating layer formation. The addition of carboxylic acid groups decreases the hydrophobicity

of the nanotubes resulting in less tendency for them to aggregate in solution and when spread on the water subphase. This is observed in the isotherms by the sharp transitions and steep gradients in the condensed phase showing good order of the nanotube film.

Figure 6.23 shows the effect of adding varying percentages (by volume) of methanol to the pure water subphase on the surface pressure versus area isotherm when a constant amount (0.04 ml) of SWCNT-O material is used. In a very similar manner to the semiconducting and metallic material, the addition of methanol has the effect of both lowering the overall surface pressure generated and also shifting the isotherm to the left. This shift to the left suggests a lower "area per molecule value" most likely caused due to improved dispersion of the material on the water surface with the addition of methanol, as discussed in Section 6.3.2.

6.5.2 Deposition

Transfer of floating SWCNT-O layers to solid (glass) substrates was performed under optimised conditions. This involved using a water subphase with 5 % (by volume) of methanol added to aid in floating layer formation. The floating layer was then compressed and held at a constant pressure chosen from the steepest part of the isotherm (in this case around 10 mN/m). Figure 6.24 shows a typical deposition record for oxidised carbon nanotubes. The floating layer is relatively unstable as shown by the steady decrease in area between dipping cycles. Material is only transferred when the substrate is withdrawn through the floating layer, showing z-type deposition on the hydrophobic substrate.

The observations made in Section 6.5.1 suggested that the oxidised material would produce better deposition results. The sharp transition points and steep condensed regions shown in the isotherms suggest a more stable floating layer with oxidised

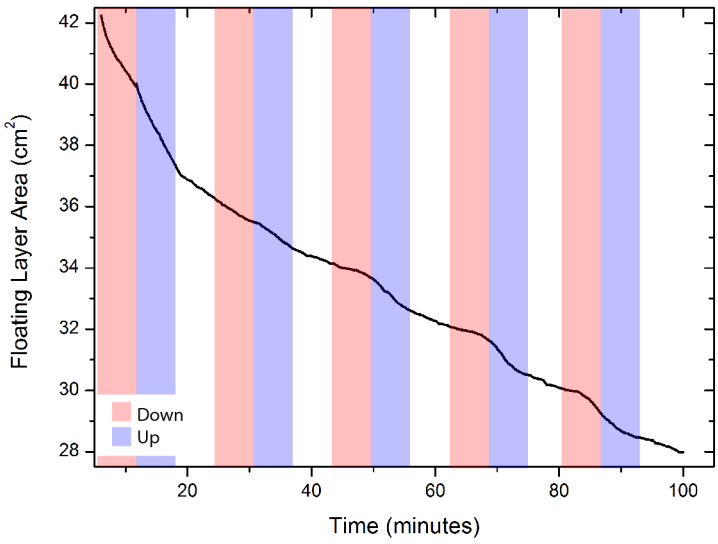

Figure 6.24: *Area versus time deposition record for 5 LB cycles of SWCNT-O onto hydrophobic glass. The floating layer was formed by spreading 0.3 ml of SWCNT-O solution onto a subphase consisting of water containing 5 % methanol and held at a constant pressure of 10 mN/m. The shading indicates the motion of the substrate through the floating layer.*

material. Instead, poor deposition was observed with low transfer ratios between 0.42 and 0.17, compared with the transfer ratios of up to 0.94 for the SWCNT-U_a and SWCNT-U HiPCO material. Later discussion in Section 7.3.1 indicates that residual surfactant present in the sorted material caused improved film transfer, whereas the oxidised material would have had fewer impurities due to the extra processing steps involved.

6.6 Optimum Deposition Conditions

Table 6.2 summarises the optimum conditions for successful film transfer as discovered through this work. Ranges of values are quoted, due to the unpredictable nature of the carbon nanotube solutions. These values assume well dispersed solutions, before each experiment the nanotubes were sonicated for 10 min in an ultrasonic bath in an attempt to improve consistency. Although transfer ratios greater than unity are not normally presented for LB deposition, for this work with SWCNT they simply reflect the unstable nature of the films. The very large transfer ratios show that there is floating layer collapse during deposition. This was described in the relevant sections. Despite this, successful film transfer was performed and the values here give an overview of the optimum conditions to minimise collapse of the floating layer.

Material	**Subphase**	**Control Pressure**	**Transfer Ratio**	**Deposition Type**
SWCNT-U	H_20	10–20 mN/m	0.7–0.95	Y-type
SWCNT-U_a	H_20	20–40 mN/m	0.94–1.06	Y-type
SWCNT-S	H_20 with 5 % methanol	7–10 mN/m	1.7–2	Z-type
SWCNT-M	H_20	7–10 mN/m	>2	Z-type
SWCNT-O	H_20 with 5 % methanol	10 mN/m	0.17–0.42	Z-type

Table 6.2: *Table showing optimum deposition conditions for the various SWCNT materials used in this work.*

Multiple layer films were built up with all of the materials listed in Table 6.2 to thicknesses of at least 7 layers, with no sign of an upper limit being reached in the ability to transfer layers. For the SWCNT-U, films of up to 99-layers in thickness were built up. If the deposition records are analysed, then the "best" SWCNT material to transfer by LB deposition appears to be the annealed SWCNT (SWCNT-U_a). Despite less consistent deposition records and more erratic transfer ratios, the superior coverage observed by AFM measurements was with SWCNT-S material transferred from a water with 5 % methanol subphase. The surfactant contamination present in this material is thought to have aided in transfer.

6.7 Graphene

A surface pressure versus area isotherm for graphene platelets in aqueous solution is shown in Figure 6.25. The starting pressure of 8 mN/m and then an immediate linear increase up to 12 mN/m suggests the presence of a relatively complete layer in the condensed phase to begin with. From 80 cm^2 to 40 cm^2 there is a plateau region followed by a slight increase in surface pressure down to the minimum trough area of 20 cm^2. As there is no significant increase in surface pressure, this would indicate that there is no significant order generated in the floating layer. When the layer is expanded there is a large amount of hysteresis evident. A much lower surface pressure is recorded when the floating layer area is increased again with the final pressure reduced to 6.5 mN/m. This is likely to be related to the plate-like and highly hydrophobic nature of the graphene. This will make the formation of an ordered floating layer difficult as the graphene plates will tend to overlap each other and "curl" on the surface. There are reports of successful LB deposition of

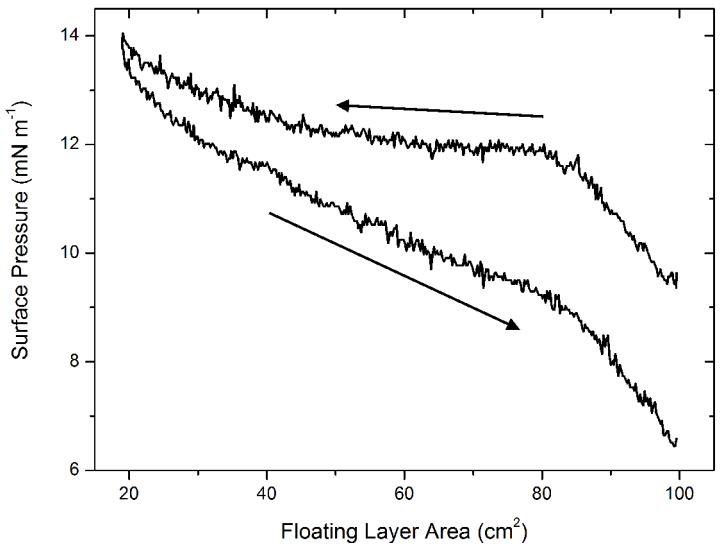

Figure 6.25: *Surface pressure versus area isotherm for 0.1 ml of graphene solution on a pure water subphase (pH 5.8 ± 0.1, temperature (20 ± 1)°C, barrier compression speed 0.5 mm/s).*

graphene/graphite oxide [19, 20] where the graphene has hydrophilic groups added to reduce the hydrophobicity thus improving the floating layer formation. This has not been explored further in this work as nanotubes are the main focus of this thesis.

A TEM image of one LB layer of graphene deposited on an amorphous carbon grid is shown in Figure 6.26. Although the film quality is poor, with only a few graphene platelets evident on the surface, a few pieces of graphene were successfully transferred.

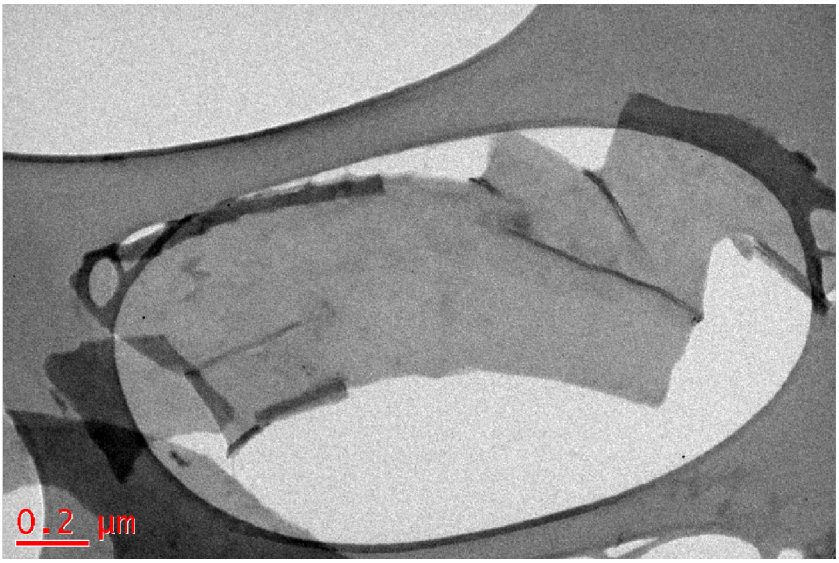

Figure 6.26: *TEM image of one LB cycle of graphene deposited on an amorphous carbon grid.*

6.8 Conclusions

Single-walled carbon nanotubes have successfully been transferred from floating layers on a pure water subphase, onto solid borosilicate glass substrates. Unsorted, annealed SWCNTs showed significantly more structure in the floating layers and exhibited improved transfer onto solid substrates compared with the non-annealed SWCNTs. This was attributed to the introduction of carboxylic acid groups on the surface of the nanotubes during the annealing step, reducing their hydrophobic nature. Langmuir-Blodgett deposition with an AC field applied to electrodes on the substrate showed increased amounts of material around the electrode, suggesting that electric fields could be used to manipulate deposition and potentially affect the alignment of the nanotubes. The mechanism responsible for alignment is thought to be dielectrophoresis. Floating layers of semiconducting and metallic SWCNTs were characterised, with both materials showing similar results. It was found that varying the amount of starting material shifted the isotherm along the area axis, and different regions could be observed. A general isotherm was presented showing the four key regions observed as the surface pressure of the floating layer was increased. The addition of small percentages of methanol to the subphase appeared to aid in floating layer formation, with sharper transitions between different phases being observed. Transfer of the floating SWCNT layer to solid substrates proved challenging when a pure water subphase was used. The addition of a small volume of methanol to the subphase improved deposition for semiconducting SWCNTs, however metallic nanotubes still exhibited poor floating layer stability resulting in poor transfer. The introduction of acid groups on the surface of unsorted nanotubes via an oxidation process improved floating layer formation, likely due to the reduced hydrophobicity of the oxidised SWCNTs. Surprisingly, deposition was not improved with the oxidised material. Floating layer formation of graphene was briefly explored, however this yielded significantly poorer results compared with

the SWCNTs.

References

[1] T. Takahashi, K. Tsunoda, H. Yajima, and T. Ishii, "Dispersion and purification of single-wall carbon nanotubes using carboxymethylcellulose," *Jap. J. Appl. Phys.*, vol. 43, no. 6A, pp. 3636–3639, 2004.

[2] A. Suri and K. S. Coleman, "The superiority of air oxidation over liquid-phase oxidative treatment in the purification of carbon nanotubes," *Carbon*, vol. 49, pp. 3031–3038, 2011.

[3] K. Hata, D. N. Futaba, K. Mizuno, T. Namai, M. Yumura, and S. Iijima, "Water-assisted highly efficient synthesis of impurity-free single-walled carbon nanotubes," *Science*, vol. 306, pp. 1362–1364, 2004.

[4] Z. F. Ren, Z. P. Huang, J. W. Xu, J. H. Wang, P. Bush, M. P. Siegal, and P. N. Provencio, "Synthesis of large arrays of well-aligned carbon nanotubes on glass," *Science*, vol. 282, pp. 1105–1107, 1998.

[5] Z. Zhou, D. Wan, X. Dou, L. Song, W. Zhou, and S. Xie, "Postgrowth alignment of SWNTs by an electric field," *Carbon*, vol. 44, pp. 158–193, 2006.

[6] K. J. Donovan and K. Scott, "Transient electric birefringence in suspensions of single-walled carbon nanotubes," *Phys. Rev. B*, vol. 72, p. 195432, 2005.

[7] K. Tsuda and Y. Sakka, "Simultaneous alignment and micropatterning of carbon nanotubes using modulated magnetic field," *Sci. Technol. Adv. Mater.*, vol. 10, p. 014603, 2009.

[8] L. Jin, C. Bower, and O. Zhou, "Alignment of carbon nanotubes in a polymer matrix by mechanical stretching," *Appl. Phys. Lett.*, vol. 73, no. 9, pp. 1197–1199, 1998.

[9] Y. Guo, N. Minami, S. Kazaoui, J. Peng, M. Yoshida, and T. Miyashita, "Multi-layer LB films of single-wall carbon nanotubes," *Physica B*, vol. 323, pp. 235–236, 2002.

[10] Y. Kim, N. Minami, W. Zhu, S. Kazoui, R. Azumi, and M. Matsumoto, "Langmuir-Blodgett films of single-wall carbon nanotubes: Layer-by-layer deposition and in-plane orientation," *Jpn. J. Appl. Phys.*, vol. 42, pp. 7629–7634, 2003.

[11] X. Li, L. Zhang, X. Wang, I. Shimoyama, X. Sun, W.-S. Seo, and H. Dai, "Langmuir-Blodgett assembly of densely aligned single-walled carbon nanotubes from bulk materials," *J. Am. Chem. Soc.*, vol. 129, pp. 4890–4891, 2007.

[12] C. Venet, C. Pearson, A. S. Jombert, M. F. Mabrook, D. A. Zeze, and M. C. Petty, "The morphology and electrical conductivity of single-wall carbon nanotube thin films prepared by the Langmuir-Blodgett technique," *Colloids and Surfaces A*, vol. 354, pp. 113–117, 2010.

[13] P. G. Collins, M. S. Arnold, and P. Avouris, "Engineering carbon nanotubes and nanotube circuits using electrical breakdown," *Science*, vol. 292, pp. 706–709, 2001.

[14] T. Fukao, S. Nakamura, H. Kataura, and M. Shiraishi, "Solution-processed single-walled carbon nanotube transistors with high mobility and large on/off ratio," *Jpn. J. Appl. Phys.*, vol. 45, no. 8A, pp. 6524–6527, 2006.

[15] R. Krupke, F. Hennrich, and H. V. Löhneysen, "Separation of metallic from semiconducting single-walled carbon nanotubes," *Science*, vol. 301, pp. 344–347, 2010.

[16] G. G. Roberts, M. C. Petty, S. Baker, M. T. Fowler, and N. J. Thomas, "Electronic devices incorporating stable phthalocyanine Langmuir-Blodgett films," *Thin Solid Films*, vol. 132, pp. 113–123, 1985.

[17] G. Vázquez, E. Alvarez, and J. M. Navaza, "Surface tension of alcohol + water from 20 to 50 °C," *J. Chem. Eng. Data*, vol. 40, pp. 611–614, 1995.

[18] J. Y. Lee, K. Liang, K. H. An, and Y. H. Lee, "Nickel oxide/carbon nanotubes nanocomposites for electrochemical capacitance," *Synth. Met.*, vol. 150, pp. 153–157, 2005.

[19] L. J. Cote, F. Kim, and J. Huang, "Langmuir-Blodgett assembly of graphite oxide single layers," *J. Am. Chem. Soc.*, vol. 131, pp. 1043–1049, 2008.

[20] T. Szabó, V. Hornok, R. A. Schoonheydt, and I. Dékány, "Hybrid Langmuir-Blodgett monolayers of graphite oxide nanosheets," *Carbon*, vol. 48, pp. 1670–1692, 2010.

Chapter 7

Morphology and Optical Characterisation of SWCNT Networks

7.1 Introduction

This section begins by looking at contaminants that are present in the films. These are observed visually and then analysed by AFM and SEM. The film thickness is estimated from AFM and ellipsometry data. Optical absorption is measured for the unsorted and sorted semiconducting and metallic nanotubes. The orientation of nanotubes during deposition is explored by the use of sets of interdigitated electrodes aligned at different angles on the substrate.

7.2 Unsorted HiPCO Material

7.2.1 Optical Transmission

Unsorted carbon nanotubes typically show relatively featureless absorbance curves, apart from a general increase in absorbance at shorter wavelengths [1]. Figure 7.1 depicts the optical absorbance across the visible spectrum (350 nm to 1000 nm) for a series of LB SWCNT-U films of varying thicknesses. The number of layers refers to the total number transferred to both sides of the substrate (since LB layers will be transferred to both sides of the substrate during deposition). The data reveal good transmission in the near-infra red region, with the films becoming more absorbing at shorter wavelengths. The absorption spectra for all films are relatively smooth, apart from small peaks at 460 nm and 660 nm. Similar peaks are noted in the literature and are related to the valence to conduction band electronic transitions [2, 3].

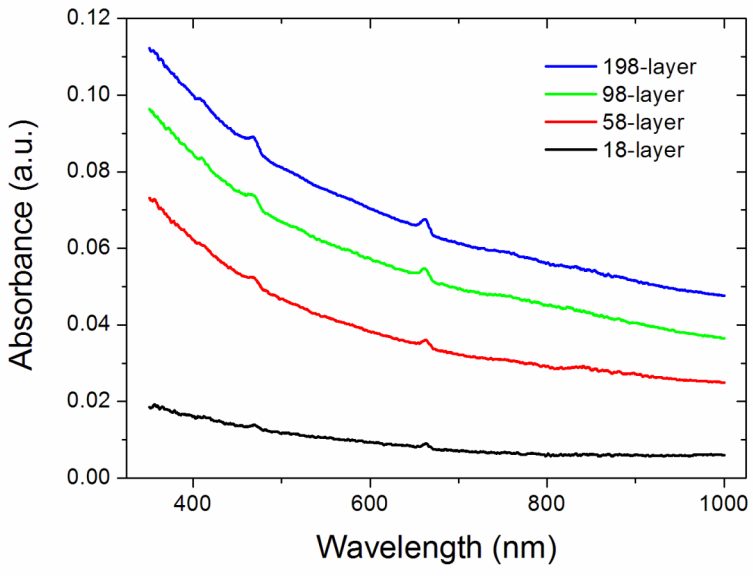

Figure 7.1: *Optical absorbance spectra between 350 nm and 1000 nm for LB SWCNT-U films of varying thickness on glass substrates.*

The dependence of film thickness on absorbance at a fixed wavelength of 500 nm is shown in Figure 7.2. Thicker films show greater absorbance, obeying a nonlinear

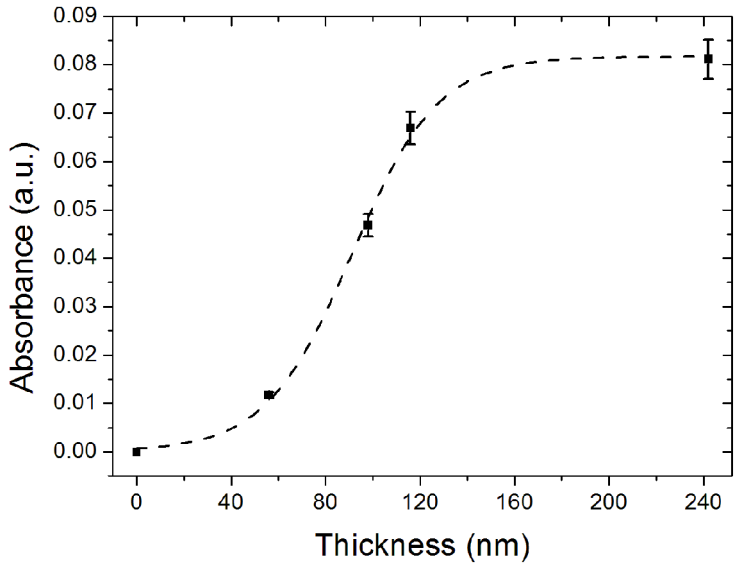

Figure 7.2: *Absorbance versus total thickness at a wavelength of 500 nm for LB SWCNT-U films.*

relationship over the range of thicknesses tested. There is a significant increase in absorbance from 56 nm to 98 nm, then from 98 nm to 116 nm the increase is proportionally less per layer. It is suggested that this is related to the structure of the films and how the material is built up on the substrate. For Langmuir-Blodgett films, it is usually assumed that one monolayer is transferred at a time so the number of dipping cycles corresponds directly to the film thickness. It is unlikely that nanotubes perform in this manner since they exist as bundles or "ropes" of tubes in solution rather than individually dispersed. Due to this, the formation of perfect monolayers is unlikely. When the first few layers are deposited the network is sparse (as discussed in Section 6.2.1 and shown in Figure 6.4); this corresponds to a very high optical transmission (for example the 56 nm thick film in Figure 7.2). As the substrate is passed through the floating layer repeated times, it is proposed that gaps in the film are initially filled in rather than directly increasing the overall thickness. Although the amount of material transferred is the same, whether it goes down in equal layers or by "filling in the gaps", the areas where there is a large amount of material are likely to introduce scattering so less light is transmitted

relative to the areas with little or no material. As the film is built up in thickness, the scattering effect will become less dominant as the coverage across the surface becomes more uniform (due to gaps being "filled in"). This could explain why up to 120 nm there is a rapid increase in absorbance for the thinner films, then as the dominance from scattering is reduced there is a much smaller increase in absorbance up to the thickest film measured of 240 nm.

A photograph of a 58-layer SWCNT-U LB film deposited on glass is shown in Figure 7.3(a), for comparison half of the substrate has been left uncoated (b). This was placed on top of a piece of paper with the logo printed on to show the difference in transparency. Visually, the nanotubes show good uniform coverage of the substrate with only a few black spots where aggregation in the floating layer has caused large amounts of material to coalesce.

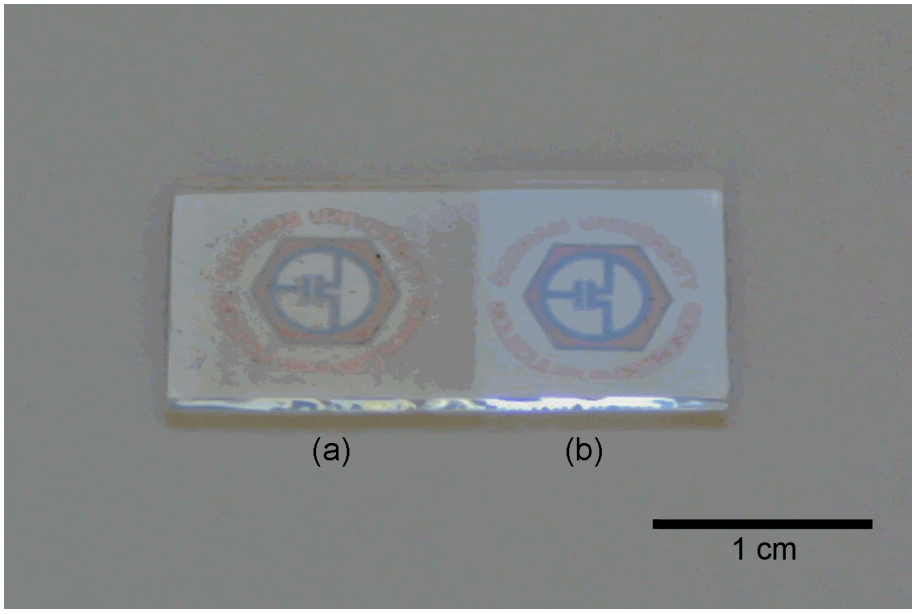

Figure 7.3: *Photograph of (a) a 58-layer SWCNT-U LB film deposited on glass and (b) the uncoated substrate for comparison, placed on top of the logo printed on paper.*

7.3 Arc Discharge Sorted Material

7.3.1 Material Contaminants

Semiconducting SWCNTs

The presence of a surface "residue" was observed optically on some substrates. This was particularly pronounced on the surface of silicon where the interference of light reflecting off the silicon with light reflecting off the surface of the film caused the silicon to appear coloured. The colour is dependant on the thickness of the film. Similar observations were made with the SWCNT-M material and are discussed later in this section. This contamination was only present in the sorted SWCNT-S and SWCNT-M materials.

It was apparent from AFM imaging that the sorted SWCNT-S and SWCNT-M solutions contained some form of contamination that was also present in the films following LB deposition. This made imaging difficult and un-washed or non-annealed samples suggested nanotube bundles embedded in another material.

Figure 7.4 shows two AFM images of a 5-layer SWCNT-S film, (a) as deposited and (b) after post-washing the film with acetone and propanol. As deposited, the

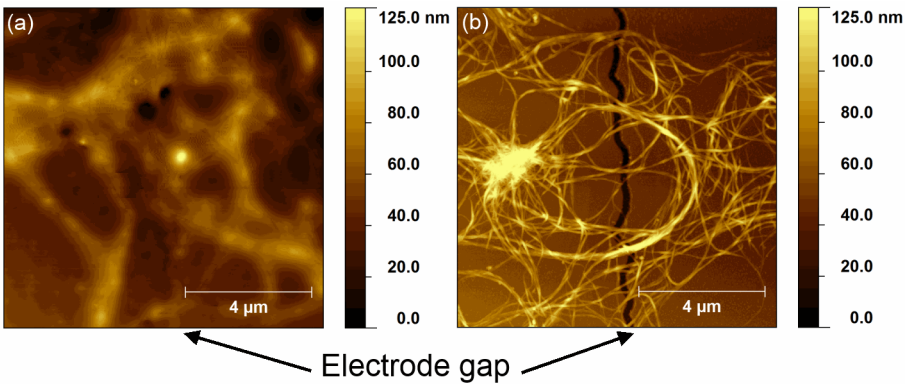

Figure 7.4: *Tapping mode AFM images of 5-layer LB films of SWCNT-S on palladium sub-micron electrodes showing (a) as-deposited and (b) after post-washing with propanol and acetone.*

electrode gap is hard to distinguish from the palladium electrodes since it appears to be "filled in". The nanotubes also appear to be surrounded by some form of surface contamination. After post-washing (b), there is a significant difference in the appearance of the film, the gap between the electrodes is now clearly visible and the fine structure of the nanotube bundles is evident.

A detailed study was undertaken on the SWCNT-S material using scanning electron microscopy (SEM) as well as energy dispersive X-ray spectroscopy (EDX). Figure 7.5 shows SEM images of a 5-layer annealed SWCNT-S film deposited on palladium sub-micron electrodes. Although annealed, some larger deposits of contamination were still present. The first image (a) shows the as-deposited film; there is significant electrical charging apparent on the surface making imaging difficult. This is likely to be due to contamination present within the film. This image shows the nanotube network embedded within another film of material. As previously discussed, this contamination can be washed away with suitable solvents, however this can also wash away some of the conducting nanotube material. Instead, the sample was annealed at 150 °C for 120 min to burn off any residue, the result is shown in (b). There is no charging apparent on the surface and the nanotubes appear to be uncoated.

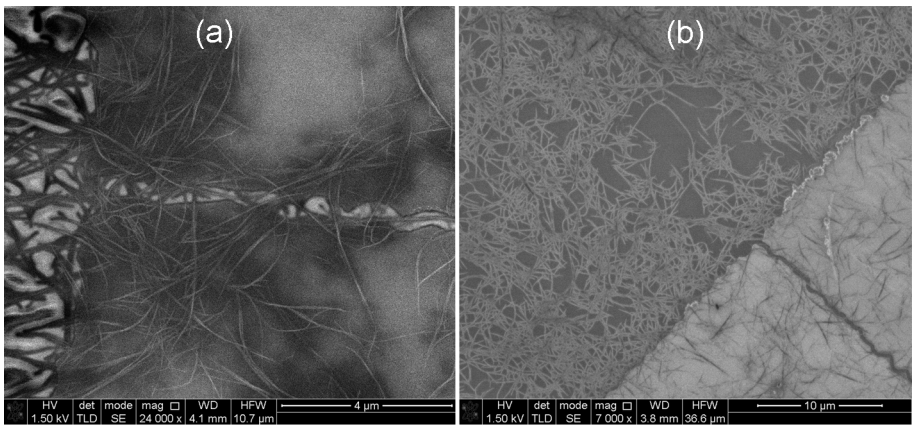

Figure 7.5: *SEM images of a 5-layer SWCNT-S film showing, (a) surface contamination in the as-deposited film and (b) the nanotube network after annealing.*

For a more detailed analysis of the materials present on the surface, an element map was made using the EDX function of the microscope. Two regions are shown in

Figure 7.6 with (a) showing a typical electrode gap region and (b) a large sodium deposit. From both regions, it can be seen that aluminium is present over the whole substrate (remaining from the fabrication process), palladium is present over the majority of the substrate apart from where it has been etched to form the electrode gap (a). Silicon and oxygen are being detected from the glass substrate, the signals are masked from the palladium, hence the higher concentration measured over the electrode gap (a). Carbon shows a slightly lower density across the electrode gap (a), this could be due to the "burning out" of nanotubes following the application of a voltage to the sample (in this case a $-1\,\mathrm{V}$ to $1\,\mathrm{V}$ sweep prior to imaging), or simply the SWCNT-S adheres to the palladium more easily than glass. The large deposit near the electrode gap (a) shows a high density of carbon and iron (circled in blue), this is likely to be a catalyst impurity surrounded by a large number of nanotubes.

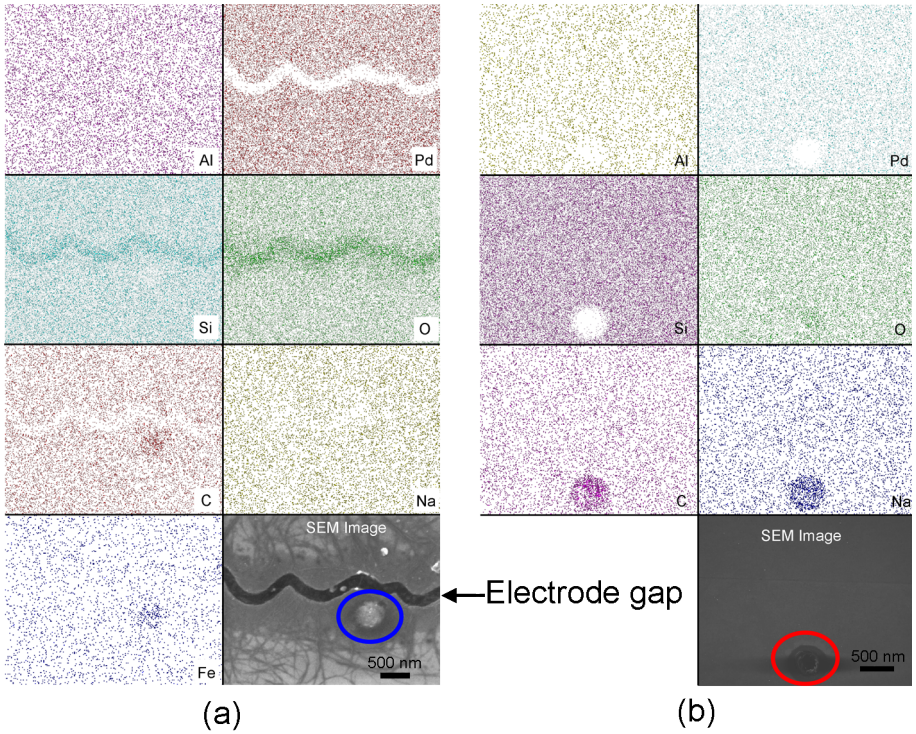

Figure 7.6: *Element map from EDX data for an annealed 5-layer SWCNT-S LB films on palladium electrodes showing (a) an area around the electrode gap and (b) a large sodium deposit. The blue circle highlights a dense deposit of carbon and iron, the red circle highlights a large deposit of carbon and sodium.*

In the second region (b) there is a large deposit towards the bottom of the area imaged (circled in red). This is comprised primarily of carbon and sodium suggesting the presence of a sodium salt. There are several of these regions across the substrate, leading to the conclusion that the main residue present can be attributed to the remains of a surfactant from the separation process [2]. This was reinforced by the observation that water also appeared to wash off the majority of the contamination from the surface. This sort of contamination was not present in films produced from SWCNT-U and SWCNT-U_a nanotubes, which had not been previously suspended with the use of surfactants.

The evidence presented here suggests that the contamination is present in the purchased material. An extra methanol washing step before suspending the material in chloroform was performed in an attempt to remove the contamination. This involved rinsing the dried nanotube mat in methanol in an ultrasonic bath for one hour, then leaving to dry before dispersion in chloroform, as described in Section 6.3.5.

Langmuir-Blodgett deposition was successfully carried out using the washed material to a thickness of 5-layers with washed SWCNT-S on a glass substrate with palladium electrodes. The extra washing step with methanol does not appear to have removed the surface contamination. Figure 7.7(a) shows the as-deposited film. Imaging in

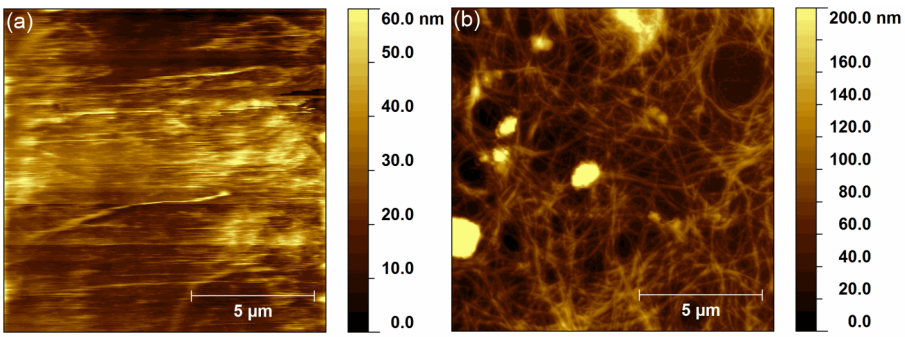

Figure 7.7: *Contact mode AFM images of a 5-layer LB film of washed SWCNT-S on glass with palladium electrodes (a) as deposited and (b) after annealing at 150°C for 30 min.*

contact mode proved difficult, as the surface appeared to be loose and was moved around by the tip. When the substrate was annealed at 150 °C for 30 min the structure of the SWCNT-S film is clear, allowing easy imaging of the surface (b). It is hard to say if the contamination was removed by pre-washing or the annealing step. The annealing step could have had one of two effects, either burning off any impurities present in the film, or simply improving the adhesion of the nanotubes to the surface. Either of these would explain the difference between Figure 7.7(a) and (b).

Metallic SWCNTs

Sorted metallic SWCNTs also appeared to contain some form of contamination in the as-deposited films. An AFM of a typical 4-layer SWCNT-M LB film on glass is shown in Figure 7.8(a). In a similar manner to the SWCNT-S, the nanotubes appear embedded within another material, making imaging difficult with the AFM.

The SWCNT-M were washed with methanol (as described in Section 6.3.5) before dispersion in chloroform, and then transferred by LB deposition to a glass substrate. A 1-layer film of washed SWCNT-M is shown in Figure 7.8(b), as can be seen there is little evidence of any contamination in the image.

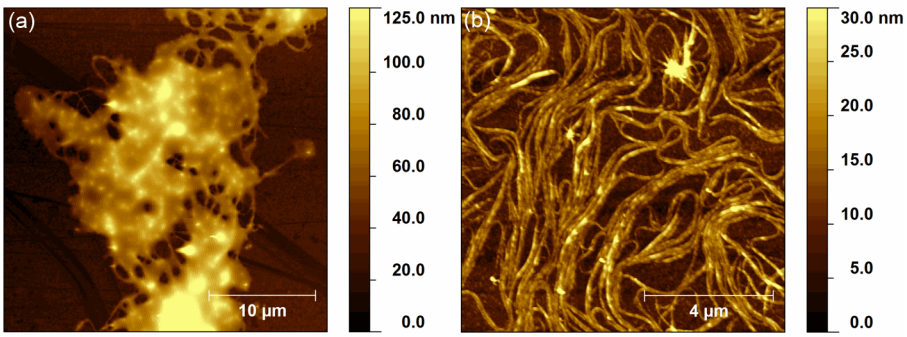

Figure 7.8: *Tapping mode AFM images of (a) a 4-layer LB film of unwashed SWCNT-M deposited on glass and (b) a 1-layer LB film of washed SWCNT-M deposited on glass.*

Although the contamination present in the bought in material could to some extent be removed by pre-washing in methanol; LB film transfer using pre-washed material proved challenging. It was concluded that the presence of this residue aided in layer formation and film transfer. For this reason the thermal annealing step following LB deposition was chosen as the preferred method of removing the impurity to improve conductivity and adhesion to the substrate.

7.3.2 Film Thickness

Ellipsometry and atomic force microscopy were used to estimate the thickness of deposited SWCNT networks. Semiconducting and metallic material are analysed in this section.

Semiconducting SWCNTs

Figure 7.9 shows an AFM image of a 4-layer LB SWCNT-S film deposited on silicon. The material has been removed on the left hand side to reveal the thickness of the film. Three height profiles have been taken from the AFM image and are shown in the graph. The step height can be estimated as being roughly 10 nm to 30 nm if the region between 8 µm to 16 µm along the x-axis is considered and the large peaks are ignored (as these are likely a result of material being displaced from the left hand side). This would estimate the layer thickness at roughly 2.5 nm to 7.5 nm.

A second method of measuring film thickness was used, ellipsometry, with a summary of the data in Table 7.1 for a 4-layer film (assuming a non-absorbing film). Due to the nature of the measurement system, an average thickness over an area will be obtained, rather than point measurements. The thickness ranges from 5.7 nm to 12.2 nm. This variation across the substrate is due to the sparse nature of

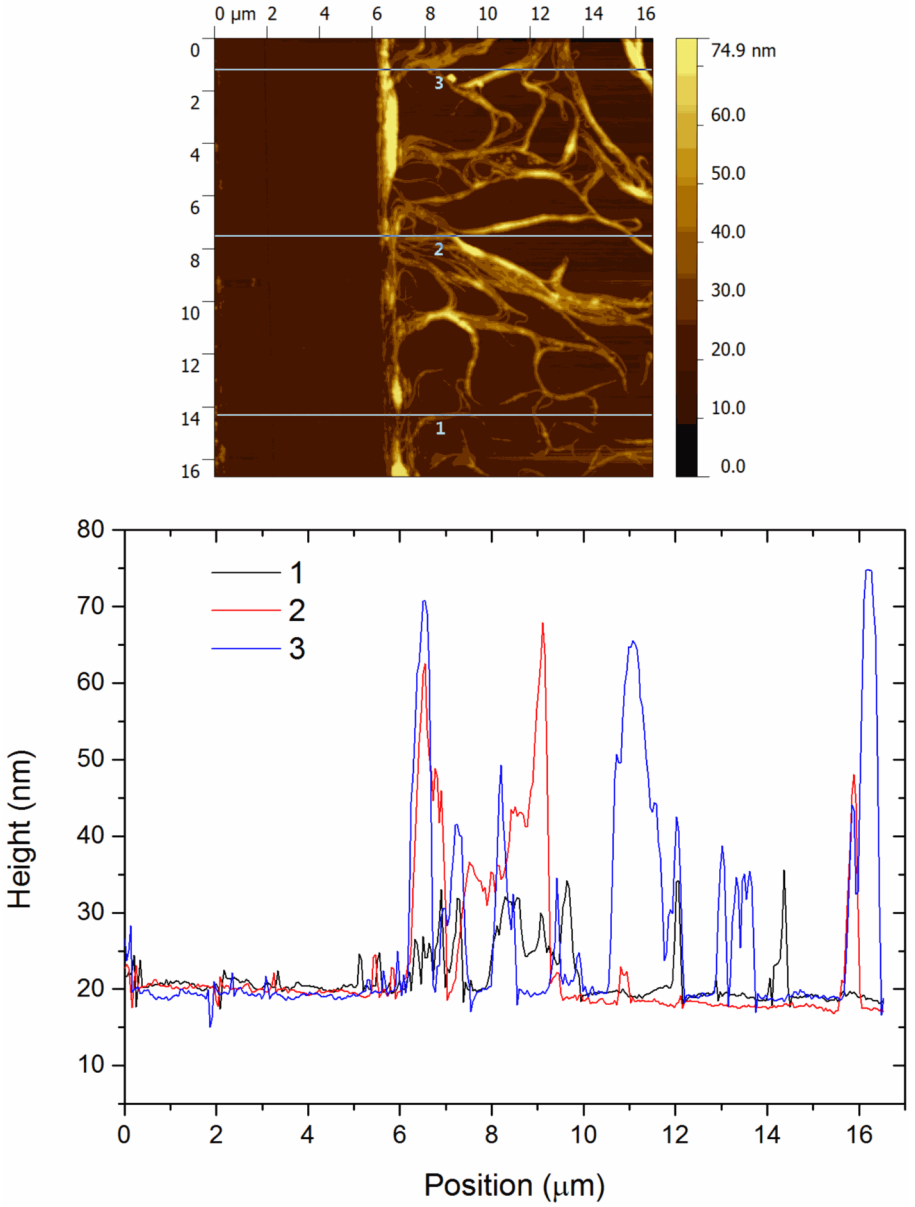

Figure 7.9: *AFM image of an annealed 4-layer SWCNT-S film deposited on a silicon wafer, the film has been removed on the left side of the image. The lower image shows three height profiles across the film.*

Location	Thickness (nm)	Refractive Index at 632.8 nm	Refractive Index at 546.1 nm
1	5.9	2.07	1.47
2	12.2	2.36	1.99
3	7.5	2.29	2.05
4	5.7	2.02	1.42
5	8.9	2.58	1.81

Table 7.1: *Summary of ellipsometry data for a 4-layer SWCNT-S film.*

the coverage when only a few LB layers of nanotubes are transferred. An average thickness across the surface can be calculated to be 8 nm, giving a thickness per layer of 2 nm. This is comparable to the lower limit of the thickness range estimated from the AFM data. Ellipsometry also provided refractive index values, averaged over five points, for the semiconducting LB Networks of 2.26 at 632.8 nm and 1.75 at 546.1 nm.

Metallic SWCNTs

A 4-layer SWCNT-M film was prepared in the same manner as the SWCNT-S for a direct comparison of the film thickness and amount of material transferred during LB deposition. Figure 7.10 shows an AFM image of the 4-layer SWCNT-M LB film on silicon along with three height profiles taken from the AFM scan. Due to the very sparse nature of the metallic LB films, particularly at low numbers of layers it is difficult to estimate a step height as no clear step is observable. If the average height of the bundles (to the right of the image) is considered then an average value between 10 nm to 20 nm can be estimated giving a very approximate layer thickness of 2.5 nm to 5 nm.

A summary of the film thickness and refractive index at 632.8 nm (assuming a non-absorbing film) from ellipsometry measurements is shown in Table 7.2. The thickness ranges from 3.2 nm to 4.7 nm, suggesting a more uniform coverage on the substrate than the semiconducting nanotubes, however this is hard to quantify from the data presented. An average thickness from these five regions is 3.9 nm giving a value per layer of below 1 nm, much smaller than the value reported from AFM. From the AFM image in Figure 7.10 it can be seen that rather than long interconnected bundles spanning the area, the metallic nanotubes have deposited in much smaller bundles, well distributed over the substrate.

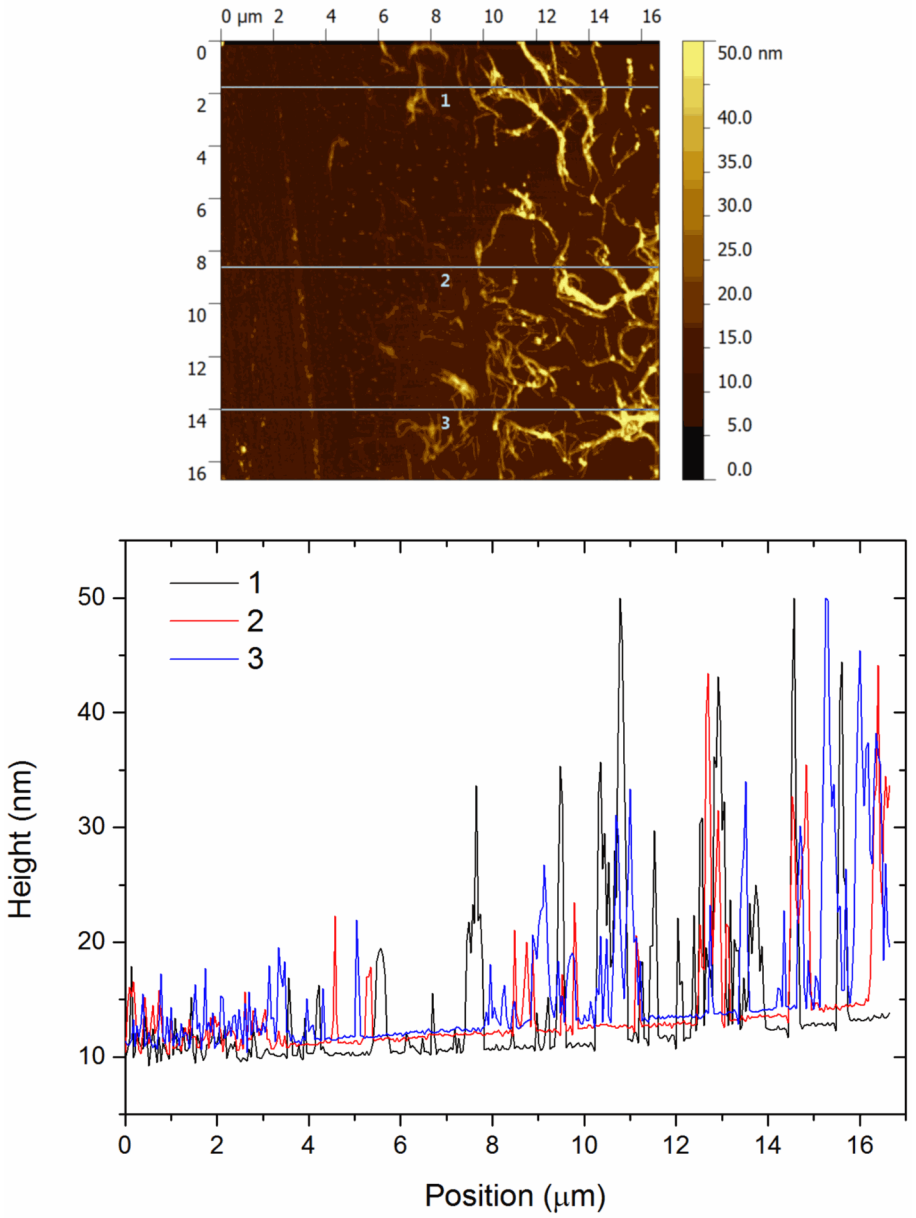

Figure 7.10: *AFM image of an annealed 4-layer SWCNT-M film deposited on a silicon wafer, the film has been removed on the left side of the image. The lower image shows three height profiles across the film.*

Location	Thickness (nm)	Refractive Index at 632.8 nm	Refractive Index at 546.1 nm
1	4.7	2.03	3.09
2	3.6	1.90	2.77
3	4.3	1.17	2.83
4	3.8	2.25	2.82
5	3.2	1.90	2.76

Table 7.2: *Summary of ellipsometry data for a 4-layer SWCNT-M film.*

However, the average height due to so much of the substrate remaining uncoated will be low so when ellipsometry is used the average over a certain area will return a low value. This is much lower than that of the semiconducting nanotubes, as expected for SWCNT-M which have shown poorer deposition throughout this work. The refractive indices of the metallic LB networks are 1.85 at 632.8 nm and 2.85 at 546.1 nm. This shows a higher refractive index at 632.8 nm and lower at 546.1 nm compared with the SWCNT-S material, possibly related to the greater/weaker absorption peaks around these wavelengths.

7.3.3 Optical Transmission

Solution Spectra

The optical absorbance spectra across a wavelength range from 400 nm to 1600 nm for chloroform solutions of semiconducting and metallic nanotubes were recorded

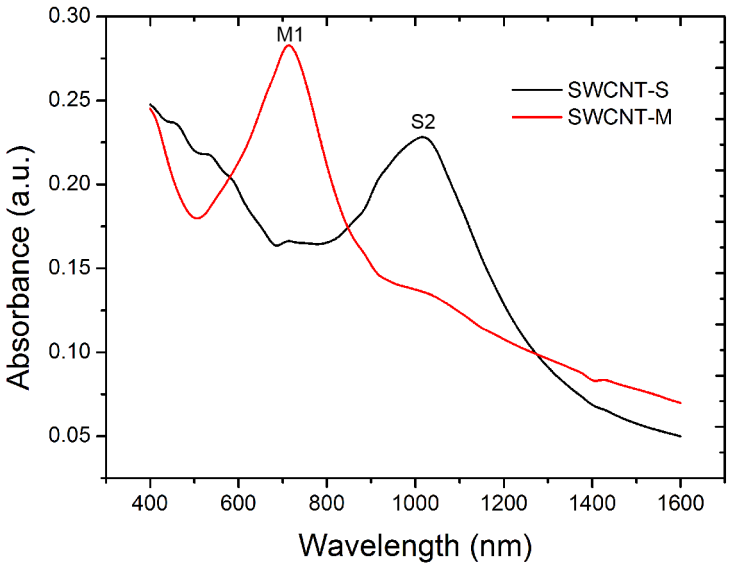

Figure 7.11: *Optical absorbance for SWCNT-S and SWCNT-M suspended in chloroform. The first metallic, E_{11}^{M} (M1) and second semiconducting, E_{22}^{S} (S2) transitions are labeled.*

and the results are presented in Figure 7.11. An absorption maxima at 1050 nm is observed for the SWCNT-S, corresponding with the second semiconducting transition (E_{22}^{S}), labelled S2. The absorption maxima at 700 nm for the SWCNT-M corresponds with the first metallic transition (E_{11}^{M}), labeled M1. These different maxima are related to the band structure of the nanotubes, in particular transitions between the valence and conduction bands, light is absorbed when in resonance with the E_{ii} values for certain nanotubes in a sample. This identifies clear differences between the two materials, showing that the nanotubes have indeed been sorted. These absorption data correspond with published data regarding optical absorption of sorted SWCNTs [2], .

Solid Phase Spectra

Thin films of SWCNT-S and SWCNT-M were prepared on borosilicate slide glass under the optimum LB deposition conditions for each material. For accurate

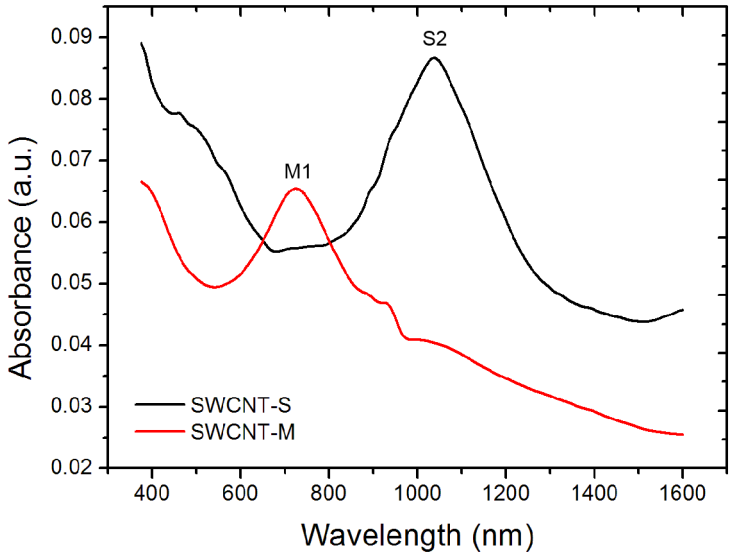

Figure 7.12: *Optical absorbance for 14-layer SWCNT-S and SWCNT-M LB films as deposited on glass. The first metallic, E_{11}^{M} (M1) and second semiconducting, E_{22}^{S} (S2) transitions are labeled*

comparison, LB deposition was carried out to produce 14-layer films for each material. The absorbance spectra are shown in Figure 7.12 for both materials across the wavelength range 400 nm to 1600 nm. It is clear from the data that the semiconducting nanotube film is significantly more absorbing across all wavelengths. This is to be expected from the results presented in Section 6.3.4 where it was noted that the semiconducting nanotubes transferred more successfully to glass substrates. Although the number of LB cycles was the same for both materials, more material would have been transferred per layer for the semiconducting material resulting in a denser film, hence the increased absorbance. As for the solution spectra (Figure 7.11) there are the same differences in the shape of the absorption spectra. Absorption maxima are present at the same wavelengths, 1050 nm for SWCNT-S and 700 nm for SWCNT-M. The features are broadened slightly in the solid phase, as expected.

7.4 Orientation During LB Deposition on Interdigitated Electrodes

To measure the in-plane DC conductivity, interdigitated gold electrodes were fabricated as described in Section 5.5.1. Electrodes with a nominal gap of 5 µm were used for the results presented here, significantly greater than the maximum length of an individual tube (maximum length of 1 µm). Conducting pathways must therefore consist of bundles of tubes spanning the electrodes. The layout of these electrodes also offered the opportunity to measure the conductivity in different orientations on the film to explore the alignment of the nanotubes during transfer from the floating layer to the substrate. Unsorted HiPCO SWCNT-U material was used for the experiment.

Figure 7.13 shows the current versus voltage characteristics for a 29-layer SWCNT LB film in relation to the dipping direction. An interesting observation is the high

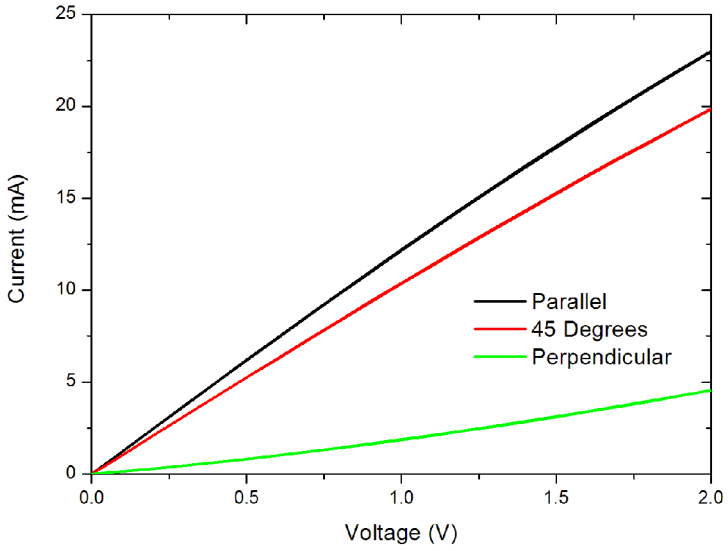

Figure 7.13: *In-plane current versus voltage characteristics for a 29-layer SWCNT-U film on glass with 5 µm interdigitated gold electrodes.*

in-plane anisotropy showing a significantly higher current along the direction of dipping ("parallel"). The conductivity for the 45° orientation is lower and the conductivity perpendicular to the direction of dipping is significantly lower again. These electrical data suggest a preferred alignment of nanotubes along the direction of dipping [4]. It is unclear whether the alignment of nanotubes occurs on the subphase surface during compression or during transfer to the substrate. If the

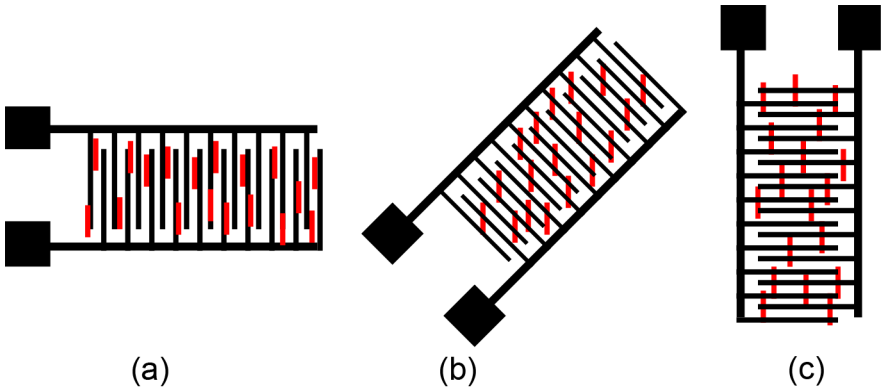

Figure 7.14: *Schematic diagram depicting the proposed alignment of SWCNT-U (represented by the red bars) on interdigitated electrodes, showing (a) perpendicular, (b) 45° and (c) parallel to the direction of dipping.*

nanotubes were aligned on the surface, parallel to the barriers, then the SWCNTs would become aligned perpendicular to the direction of dipping if the orientation was preserved during LB transfer. This is contrary to the results presented here. Alignment during film transfer (under the influence of the water meniscus) may be a more likely process. LB film experiments with other molecules have shown a similar anisotropy; for example the helices of polymers are orientated with their main axis parallel to the direction of dipping [5]. Others have noted alignment of nanotubes during LB deposition [6] (observed through optical anisotropy), supporting these findings.

The three electrode configurations with the proposed orientation of SWCNT-U following LB deposition are shown in Figure 7.14. The 45° (b) and parallel (c) orientations show how the bundles of nanotubes span the "fingers" of the electrodes resulting in the high conductivity, compared to the perpendicular (a) orientation where the majority of bundles lie between the "fingers", not contributing to the conductivity of the film.

7.5 Conclusions

It has been shown that there are contaminants present in the sorted SWCNT material. These are most likely to be residual surfactant used during the separation process. This contamination can be removed by washing with acetone and propanol, however a thermal annealing technique was favoured so as not to remove any conducting material from the network. AFM and ellipsometry data revealed a single layer thickness for the SWCNT-S and SWCNT-M materials of approximately 2 nm to 2.5 nm. However, a more accurate way to look at the thickness of LB networks of SWCNT is of an increase in density, particularly for a low number of LB cycles. Optical absorbance shows clear differences between the unsorted and sorted materials, and provide strong evidence of separated SWCNT-S and SWCNT-M in the sorted material. In-plane DC electrical measurements have shown alignment in the network, with the nanotubes exhibiting preferential orientation along the direction of dipping when transferred from the floating layer to a glass substrate.

References

[1] G. Grüner, "Carbon nanotube films for transparent and plastic electronics," *J. Mater. Chem.*, vol. 16, pp. 3533–3539, 2006.

[2] A. A. Green and M. C. Hersam, "Colored semitransparent conductive coatings consisting of monodisperse metallic single-walled carbon nanotubes," *Nano Lett.*, vol. 8, no. 5, pp. 1417–1422, 2008.

[3] M. S. Strano, C. A. Dyke, M. L. Usrey, P. W. Barone, M. J. Allen, H. Shan, C. Kittrell, R. H. Hauge, J. M. Tour, and R. E. Smalley, "Electronic structure control of single-walled carbon nanotube functionalization," *Science*, vol. 301, no. 5639, pp. 1519–1522, 2003.

[4] M. K. Massey, C. Pearson, D. A. Zeze, B. Mendis, and M. C. Petty, "The electrical and optical properties of orientated Langmuir-Blodgett films of single-walled carbon nanotubes," *Carbon*, vol. 49, pp. 2424–2430, 2011.

[5] G. Duda, A. J. Schouten, T. Arndt, G. Lieser, G. F. Schmidt, C. Bubeck, and G. Wegner, "Preparation and characterization of monolayers and multilayers of preformed polymers," *Thin Solid Films*, vol. 159, pp. 221–230, 1998.

[6] Y. Kim, N. Minami, W. Zhu, S. Kazoui, R. Azumi, and M. Matsumoto, "Langmuir-Blodgett films of single-wall carbon nanotubes: Layer-by-layer deposition and in-plane orientation," *Jpn. J. Appl. Phys.*, vol. 42, pp. 7629–7634, 2003.

Chapter 8

Electrical Characterisation of SWCNT Networks

8.1 Introduction

The formation of contacts to carbon nanotubes is key to obtaining reliable electrical data. In this chapter, this phenomenon is studied in depth with a range of different electrode materials and electrode separations. An additional processing step involving thermal annealing after Langmuir-Blodgett deposition is also explored to improve nanotube-to-metal contact formation. Finally, the conduction mechanisms at work in the networks are investigated and the differences between the semiconducting and metallic material are contrasted.

8.2 Contact Formation

This section highlights the various electrode materials and configurations used to ensure that Ohmic contacts between the electrode and nanotubes were formed. To minimise any contact effects it is important to choose a metal with a similar work function to the nanotubes. Figure 8.1 shows the electrode arrangement for the two methods of forming contacts referred to in this chapter. The top electrode contact has electrodes formed on top of the SWCNT material, whereas the bottom electrodes are pre-defined on the substrate before the SWCNTs are deposited.

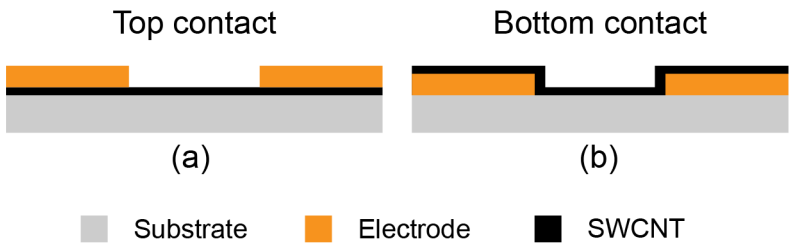

Figure 8.1: *Electrode layout used for electrical measurements for (a) top and (b) bottom contact.*

8.2.1 Aluminium Electrodes

Bottom Electrode

Semiconducting and metallic SWCNTs were deposited on top of pre-fabricated aluminium submicron electrodes (dimensions of 130 nm x 2 mm) by a solution casting method (Section 3.3.5) from solution in chloroform. The current versus voltage results for both materials are shown in Figure 8.2 with (a) representing SWCNT-S and (b) representing SWCNT-M. As can be seen, the maximum currents for both materials are very low. However, this is later improved by using a top contact structure where the electrodes are patterned following deposition of the LB

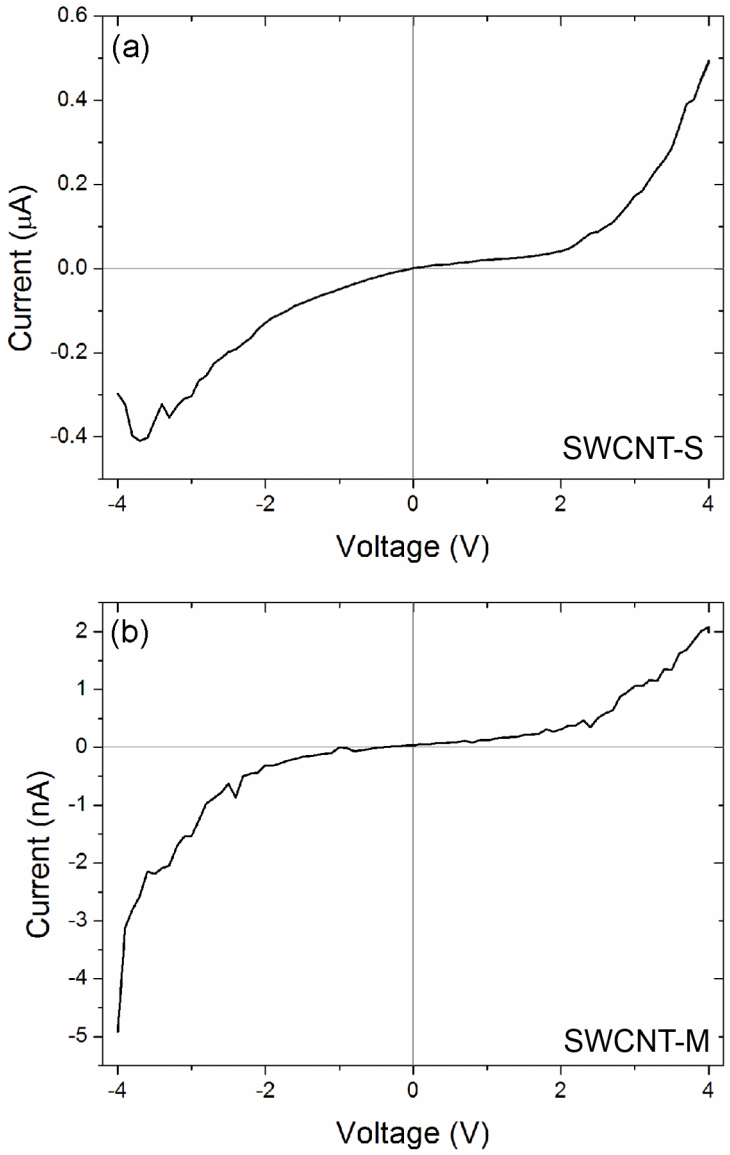

Figure 8.2: *Current versus voltage for drop-dispensed nanotubes on aluminium submicron linear electrodes (130 nm x 2 mm) with (a) SWCNT-S and (b) SWCNT-M.*

layers. The important observation from these data is in the shape of the behaviour, with both materials revealing nonlinear current versus voltage characteristics. This suggests the presence of a potential barrier(s) at the electrode(s) to nanotube interface(s).

Top Electrode

Aluminium submicron electrodes were fabricated on top of a 5-layer LB SWCNT-S network and the current versus voltage response was recorded, this is shown in Figure 8.3. The maximum current recorded, ranging from about 0.2 mA to 7 mA, is significantly higher than that for the bottom electrode devices shown in Figure 8.2 (i.e. in the mA range rather than µA range). This improvement in conductivity is thought to have been a result of the fabrication of the electrodes on top of the SWCNT-S network. The chemicals and heat involved in the lithography and metal deposition processes will have cleaned contaminants from the nanotubes, improving the contact. Thermal annealing of the nanotube networks is discussed in more detail in Section 8.2.6. Despite the improved conductivity, the current versus voltage characteristics remain nonlinear for all devices. This supports the observation made with the bottom contacted aluminium electrodes that a potential barrier is present at the nanotube/electrode interface. Aluminium is also reported in the literature as

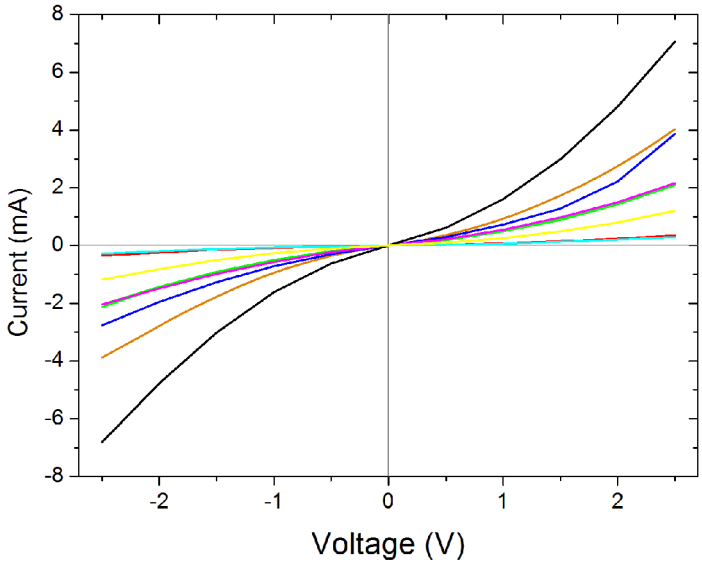

Figure 8.3: *Current versus voltage for aluminium submicron linear electrodes (130 nm x 2 mm) fabricated on top of a 5-layer LB SWCNT-S network, the different curves represent a range of devices tested on the same substrate.*

being a poor electrode material to use with carbon nanotubes due to its low work function (4.06 eV to 4.26 eV [1]) compared with other metals (such as palladium and gold) [2].

8.2.2 Gold Electrodes

Bottom Electrode

As aluminium appeared to be an unsuitable electrode material, gold was evaluated next due to its higher work function of 5.1 eV to 5.47 eV [1]. SWCNT-S and SWCNT-M networks were transferred by LB deposition to a thickness of 7-layers on glass substrates with pre-defined 15 µm chromium/gold interdigitated electrodes (see Section 5.5.1 for electrode details). Figure 8.4 shows the current versus voltage characteristics for (a) semiconducting and (b) metallic nanotubes. Both characteristics are slightly nonlinear. However, these are significantly more linear than those for the aluminium electrodes (Figure 8.2) suggesting an improved contact has been made to the nanotubes with gold electrodes. The greater conductivity for the SWCNT-M network is attributed to the interdigitated electrode design. Any large aggregates of nanotubes transferred to the substrate during LB deposition will bridge the "fingers" of the electrodes and dominate the conductivity. In this case, an abnormally large conductivity is created for the SWCNT-M compared to the SWCNT-S network.

Top Electrode

For completeness, chromium/gold electrodes were also patterned on top of 5-layer LB networks of SWCNT-S and SWCNT-M, shown in Figure 8.5. These characteristics show an improved linearity of the current versus voltage characteristic for both

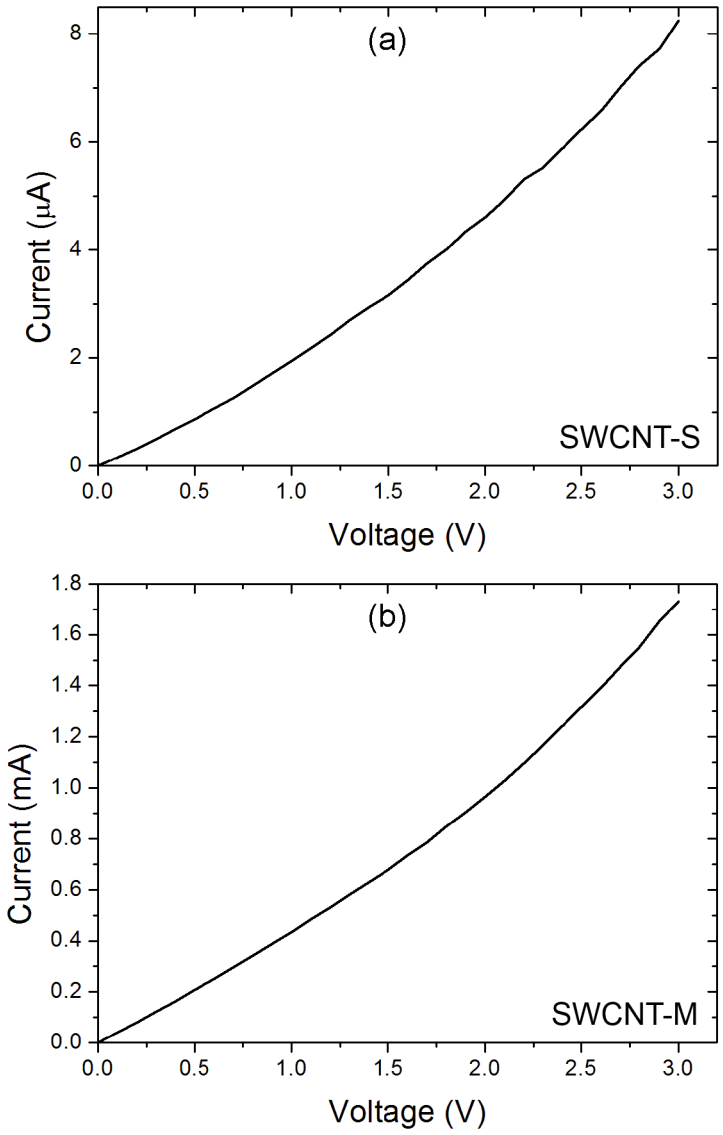

Figure 8.4: *Current versus voltage characteristics for 5-layer LB networks deposited on top of chromium/gold 15μm interdigitated electrodes, with (a) SWCNT-S and (b) SWCNT-M.*

SWCNT-S (a) and SWCNT-M (b). This is attributed to the heat involved during the evaporation of the metal to form the electrodes. This improves the contact to the nanotubes through a thermal annealing process. It is also thought that by evaporating the gold on top of the network, there will be improved physical contact between the nanotubes and the metal. Gold is known to produce good Ohmic contacts to carbon nanotubes[2].

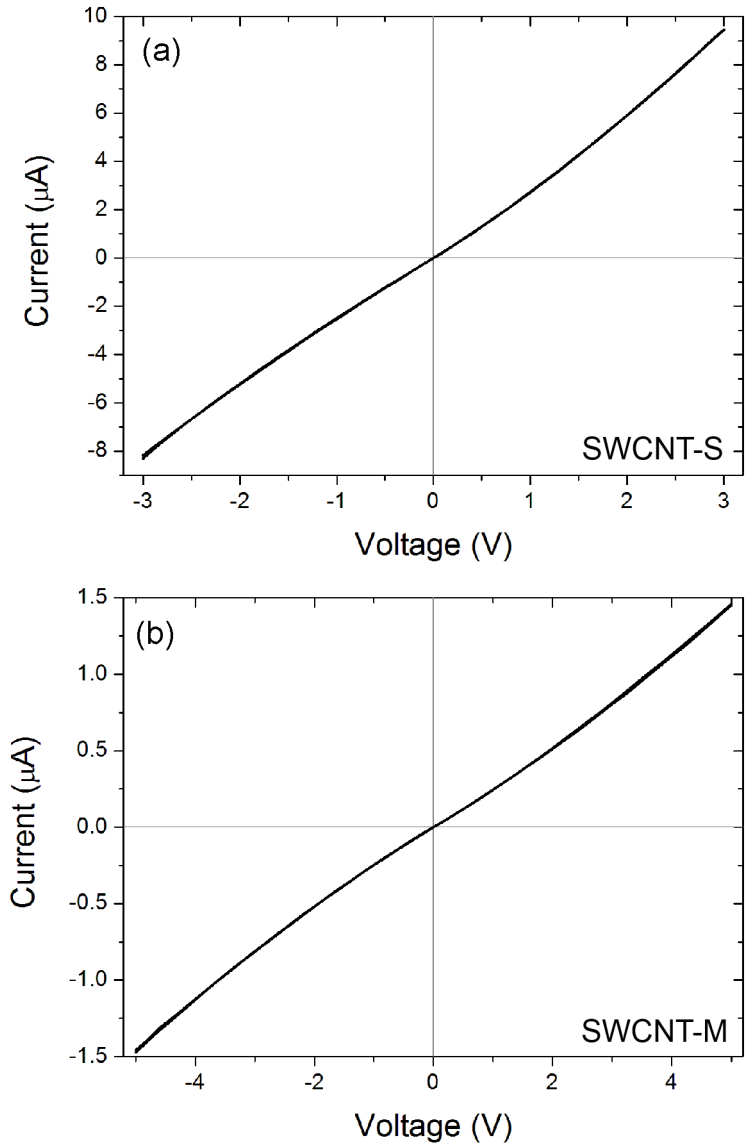

Figure 8.5: *Current versus voltage characteristics for 50 μm chromium/gold electrodes fabricated on top of 7-layer SWCNT networks on glass with (a) semiconducting and (b) metallic material.*

8.2.3 Gold - Aluminium Electrodes

Submicron spaced electrodes were fabricated from two metals with different work functions, in this case gold and aluminium. A 3-layer LB network of unsorted SWCNT-U was deposited on the electrodes and the current versus voltage behaviour was measured, shown in Figure 8.6. Although very low currents are recorded, there is asymmetry in the current versus voltage characteristics with significantly more current in one direction than the other. This asymmetry supports the suggestion that aluminium electrodes (Section 8.2.1) form a barrier with carbon nanotubes.

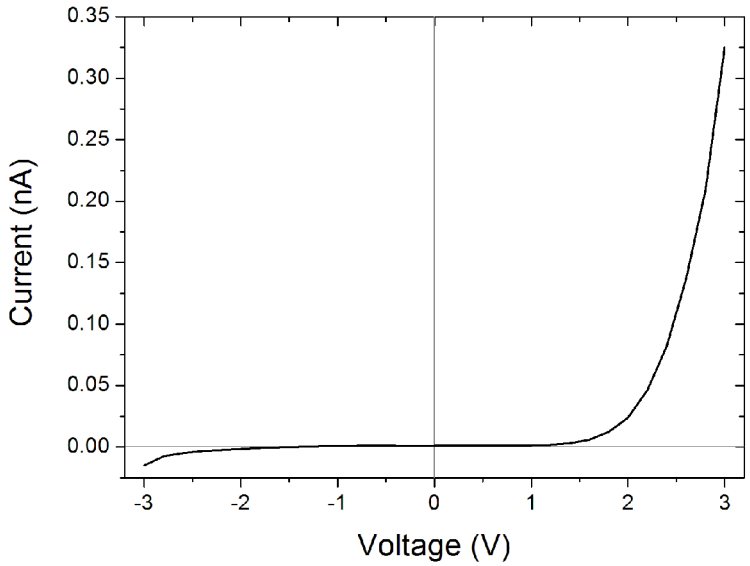

Figure 8.6: *Current versus voltage characteristic for a 3-layer unsorted SWCNT-U LB network deposited on gold and aluminium electrodes (130 nm x 2 mm).*

8.2.4 Silver Electrodes

Silver was also investigated as a potential electrode material as it has a similar work function (4.52 eV to 4.74 eV) to that of gold (5.1 eV to 5.47 eV) [1]. Langmuir-Blodgett networks of SWCNT-S and SWCNT-M were prepared on glass substrates, then silver paint was used to make contacts to the top of the network. The dimension

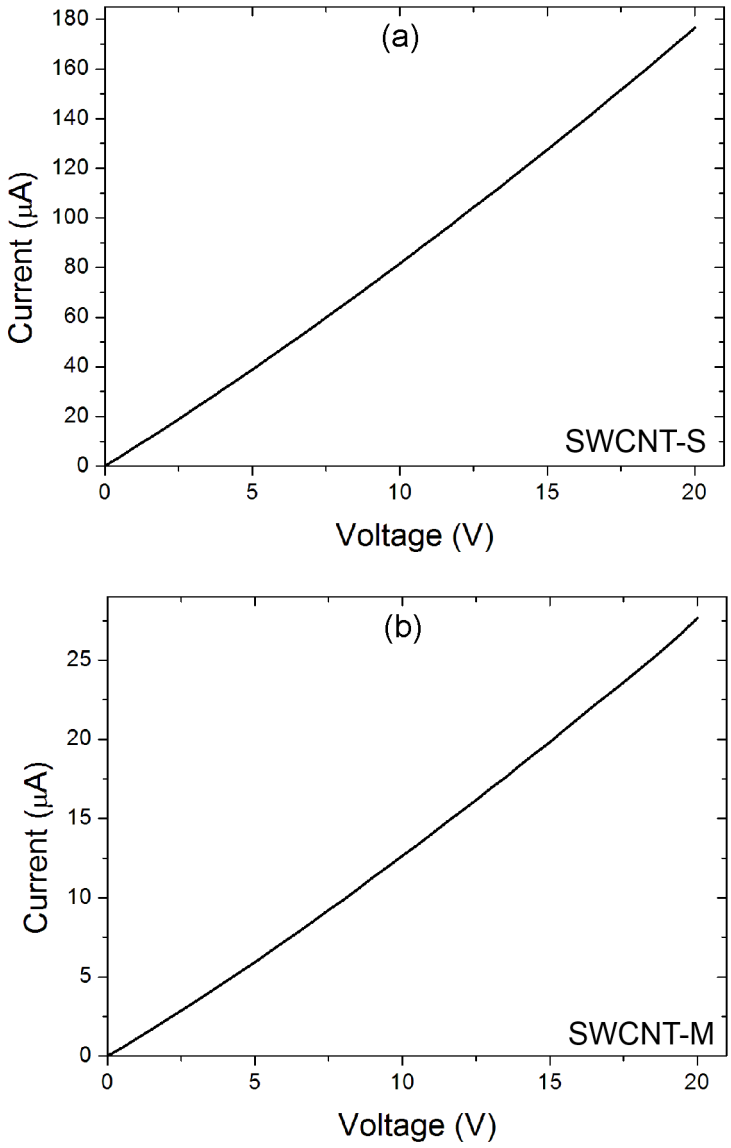

Figure 8.7: *Current versus voltage characteristics for 7-layer SWCNT networks on glass with 1 mm x 5 mm silver paint electrodes with (a) semiconducting and (b) metallic material.*

of the electrode gap was approximately 1 mm x 5 mm, so the conductivity across the network was measured across a relatively large area compared to the previous electrodes discussed. Figure 8.7 shows the current versus voltage characteristics for (a) SWCNT-S and (b) SWCNT-M material. Both materials show a near linear response, indicating a good contact to the nanotubes. The semiconducting material shows conductivity roughly one order of magnitude greater than that for metallic

nanotubes. This is in agreement with the improved deposition noted in Section 6.3.4 for SWCNT-S.

8.2.5 Palladium Electrodes

The final metal used to make contact to the nanotube networks was palladium. Again this is a high work function metal (5.22 eV to 5.6 eV), similar to that of

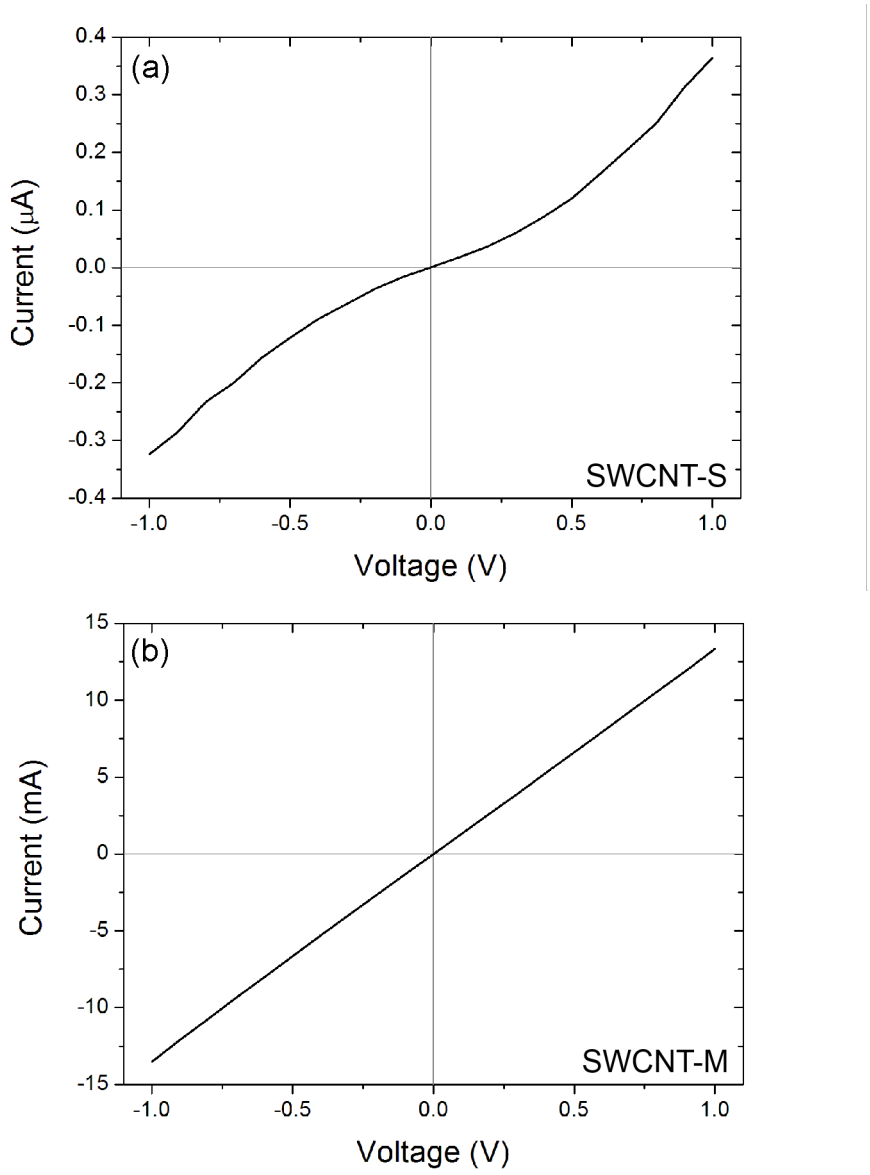

Figure 8.8: *Current versus voltage characteristics for 5-layer sorted SWCNT networks on glass with 220 nm x 2 mm palladium electrodes with (a) SWCNT-S and (b) SWCNT-M.*

gold [1]. This is widely reported as one of the optimum metals to produce ohmic contacts with carbon nanotubes [3, 4, 5]. Glass substrates were prepared with submicron spaced palladium electrodes, with channel dimensions of 220 nm x 2 mm. Networks of SWCNT-S and SWCNT-M were deposited to a thickness of 5-layers by LB deposition with the current versus voltage responses shown in Figure 8.8. The semiconducting nanotubes (a) show very low currents and a nonlinear response. However, this was later improved by a thermal annealing step (Section 8.2.6) which burnt off any contaminants present at the nanotube/electrode interface resulting in improved conductivity and a linear response. The metallic nanotubes show good Ohmic conduction as deposited on the substrate, again annealing will be shown to improve the conductivity further (Section 8.2.6).

8.2.6 Thermal Annealing

As reported in Section 7.3.1, there appears to be surface contamination present in the sorted SWCNT material. It was found that washing or thermal annealing of the networks following deposition removed the majority of this contamination. Thermal annealing was chosen as the preferred method since there is a reduced probability of removing conducting material from the network, compared to the washing process. Figure 8.9 shows the current between the palladium electrodes, with an applied voltage of 0.2 V, as a function of annealing time. Annealing was performed in air on a hotplate at 150 °C. The current before annealing was very low (only 0.16 µA). After 15 min of annealing this increased by several orders of magnitude, to 0.4 mA. Following a further 15 min of annealing the current increased again, this time by approximately a factor of 2 to 0.96 mA. Subsequent measurements show a further increase in current with a longer anneal time, however the rate of increase is significantly lower. An optimum anneal time of 30 min was chosen as this time period had the most effect on improving conductivity. It is thought

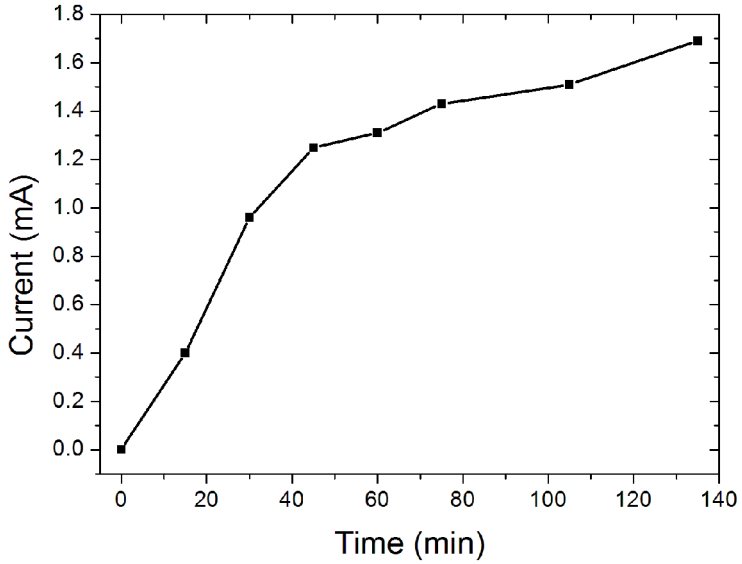

Figure 8.9: *Current versus total anneal time for a 5-layer LB network of SWCNT-S deposited on glass with 220 nm x 2 mm palladium electrodes at a voltage of 0.2 V.*

that the annealing process removes the contamination present in the as deposited networks, thus improving the contact to the palladium. It has also been reported in the literature that annealing improves the contacts between metals and nanotubes [6, 7].

A series of optical micrographs are provided in Figure 8.10, showing the uncoated electrodes, then after one drop of the nanotube solution has been spread on the surface and finally after annealing. As the networks have been drop dispensed, there is a large amount of aggregation on the surface (shown by the larger deposits). There is also the presence of a residue, which is indicated by the different coloured "coffee stain" rings formed during solvent evaporation. These result from multiple reflections though different films in contact with the glass. Following annealing, there is less residue present on the surface, indicated by the absence of the majority of the drying rings. This shows visually that the majority of the contamination has been removed after 30 min of annealing.

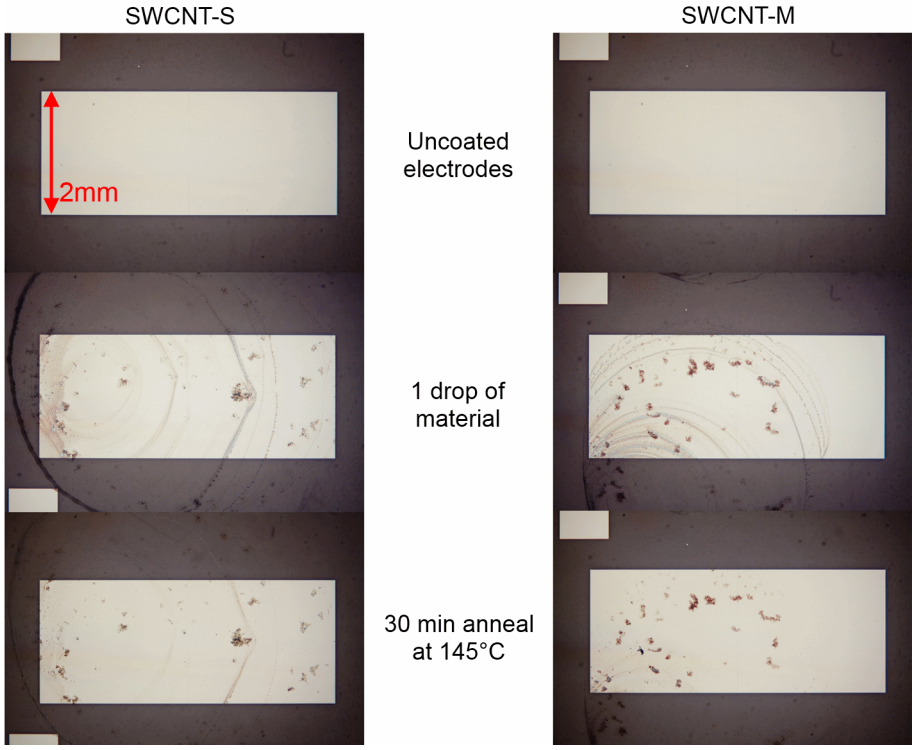

Figure 8.10: *A series of optical micrographs showing uncoated electrodes, electrodes with one drop of either SWCNT-S or SWCNT-M solution and after 30 min annealing at 150°C.*

Figure 8.11 shows the current versus voltage characteristics before and after annealing for 30 min for 5-layer SWCNT-S (a) and SWCNT-M (b) LB networks deposited on palladium submicron electrodes. In their as deposited state, the SWCNT-S show little conductivity, but following annealing the current increases to several mA. The metallic nanotubes exhibit good conductivity as deposited, but reveal some nonlinearity in their current versus voltage characteristic. After annealing, the current increases to a maximum of approximately 40 mA and the linearity has improved.

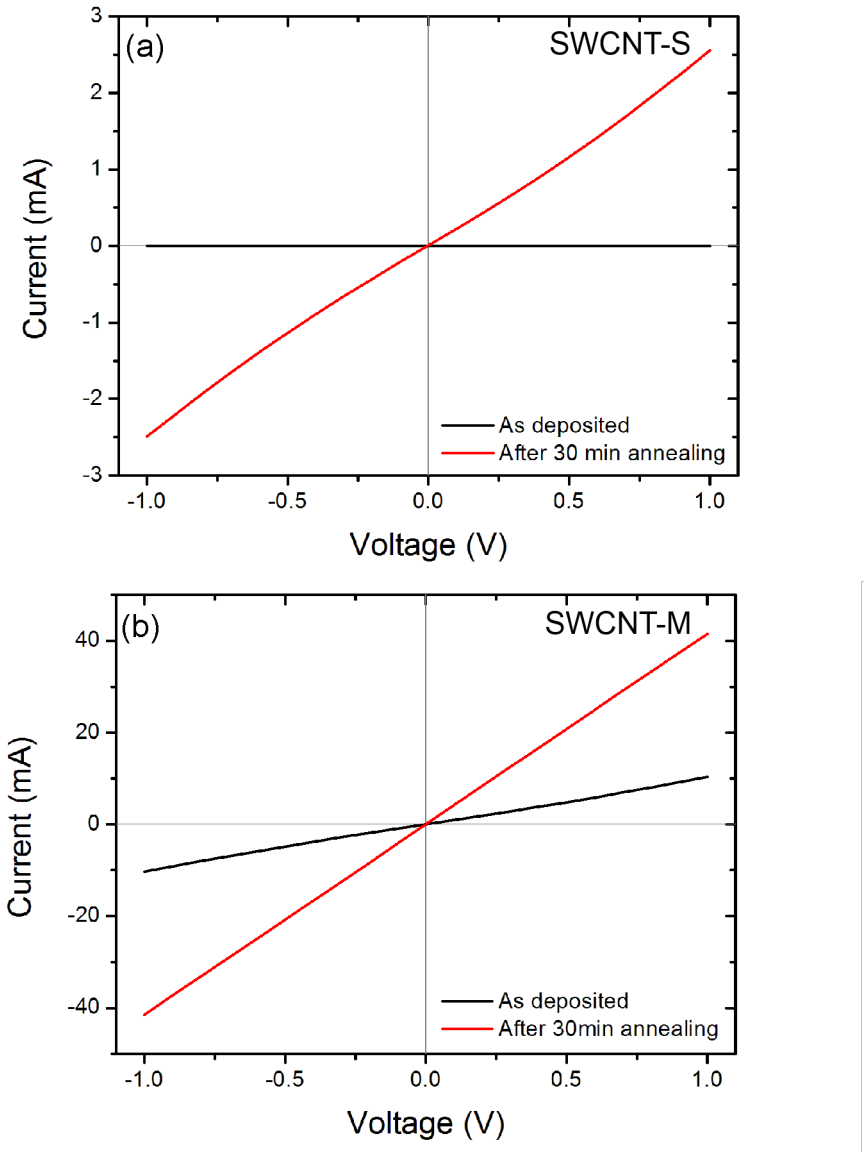

Figure 8.11: *Current versus voltage characteristics of 5-layer SWCNT-S (a) and SWCNT-M (b) networks on palladium submicron electrodes before and after thermal annealing.*

8.2.7 Electrode Spacing

Another check for the quality of contact between the electrodes and nanotube network, is to check the conductivity across a network through a range of different electrode separations. If contact effects are negligible then the conductivity should scale approximately with the electrode spacing, whereas if contact effects dominate then little scaling will be observed.

Silver Paint

Figure 8.12 shows a photograph of a 7-layer LB network of unsorted SWCNT-U deposited on glass with 4 electrodes painted onto the surface with silver paint; (1), (2), (3) and (4). The current versus voltage characteristics for three different electrode pairs are also shown in Figure 8.12. As expected, the greatest current is measured between the closest spaced electrodes ((3) - (4)) and the lowest current is measured between the furthest spaced electrodes ((1) - (3)).

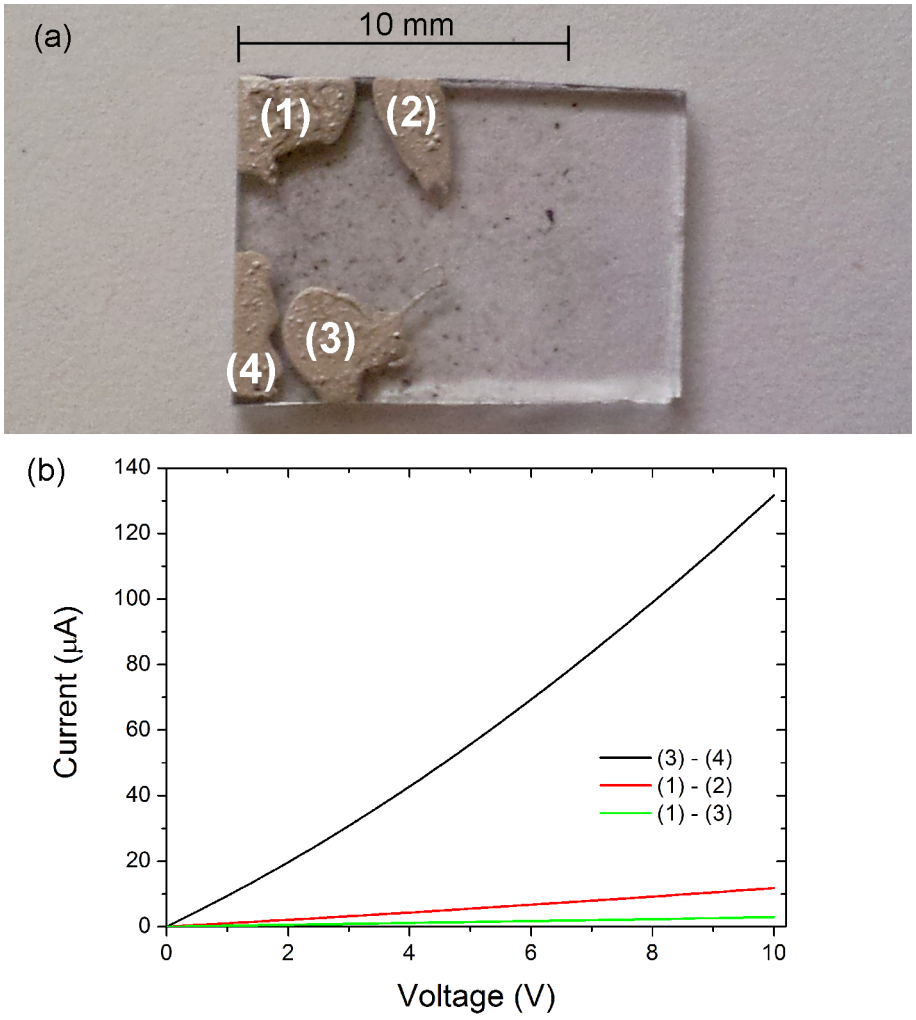

Figure 8.12: *(a) Photograph showing silver paint electrodes on a 7-layer LB network of SWCNT-U deposited on glass. (b) The graph shows the current versus voltage characteristics across different electrode pairs.*

The resistance values between the various electrodes are summarised in Table 8.1. The lowest resistance of 0.076 MΩ corresponds to the narrowest electrode gap of around 1 mm. Between electrodes (1) and (2) the resistance is approximately 10 times greater. Although the gap is only around twice the width of (3) and (4), the length is significantly less. If the dimensions are taken into account it can be concluded that the resistance has scaled roughly linearly. The resistance across the sample (electrodes (1) to (3)) is 3.44 MΩ, around 4 times greater than between (1) and (2). This has not directly scaled with the separation distance, however there are multiple pathways present for conduction (for example electrode (1) to (4) to (3)) so this is not surprising. Therefore, it can be concluded that contact effects are minimal since it is shown that the resistance does scale approximately with electrode separation.

Electrode 1	**Electrode 2**	**Resistance (MΩ)**
(3)	(4)	0.076
(1)	(2)	0.85
(1)	(3)	3.44

Table 8.1: *Summary of electrical resistance across different pairs of electrodes for a 7-layer LB network of SWCNT-U.*

Palladium

A diagram showing the layout of the palladium electrodes is shown in Figure 8.13. Measurements were taken between electrode pairs (submicron gaps) as well as from one electrode pair to another (∼2 mm). The electrodes used for the measurements presented later are numbered in the diagram.

Figure 8.14 shows the current versus voltage characteristics on; (a) electrodes with submicron gaps and (b) between the electrode pairs across much larger gaps (∼2 mm). As can be seen from (a), high currents are observed with maximum values of between 2 mA to 6 mA at 0.5 V between the very small electrode gaps (of just 220 nm).

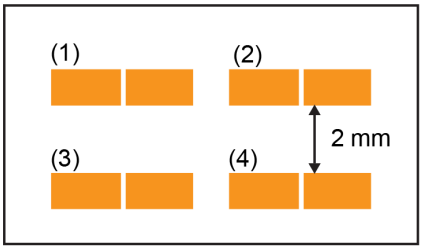

Figure 8.13: *A diagram showing the electrode layout used to gather the results in Figure 8.14.*

Across larger distances (b) the current is significantly lower for the same applied voltage. The average resistance, taken from the 4 electrode pairs, is calculated to

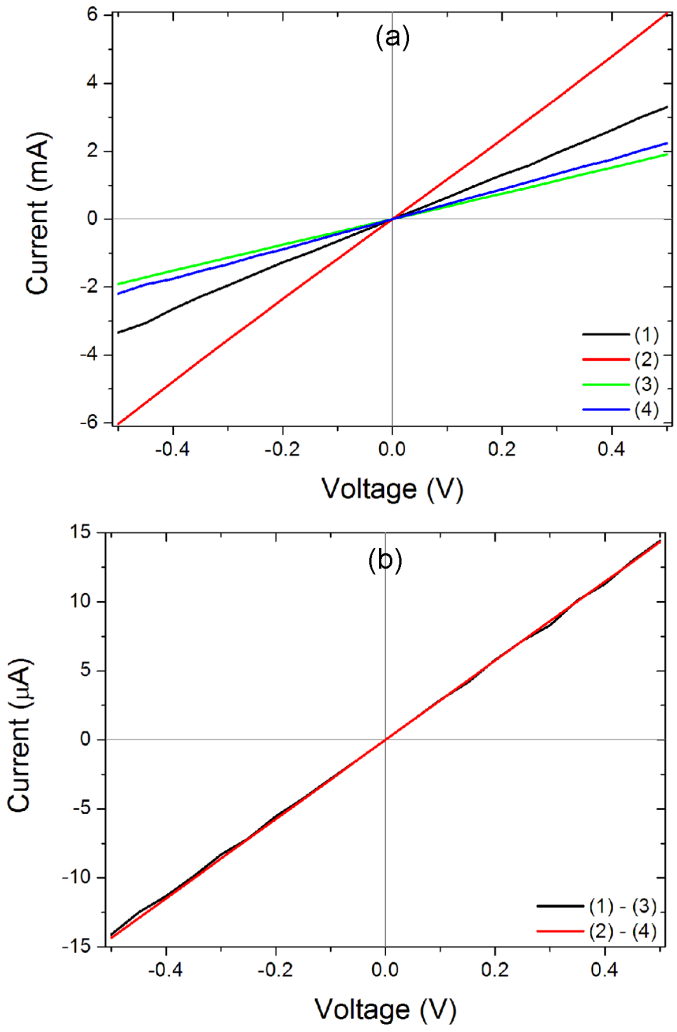

Figure 8.14: *Current versus voltage for an annealed 5-layer LB pre-washed SWCNT-S_w deposited on glass with (a) 220 nm x 2 mm palladium electrodes and (b) between electrode pairs.*

be 180 Ω. The resistance across the larger gap between electrode pairs (averaged at 34.8 MΩ) does not scale perfectly with the increase in electrode separation, however it does increase on the same order of magnitude. As with the silver electrodes, contact effects do not appear to be dominant, providing further evidence that palladium forms reliable Ohmic contacts to the nanotube networks in this work.

8.3 Electrical Annealing

The majority of SWCNT-U networks revealed semiconductive behaviour, i.e. an increasing resistance with decreasing temperature. In some cases metallic behaviour was observed, i.e. a decreasing resistance with decreasing temperature. It has previously been shown that the conductivity of SWCNT thin films can be modified by the application of a high electric field (greater than 4×10^6 V/m) [8, 9]. Due to the high electrical power dissipation in the film, a significant reduction of the in-plane conductivity of the sample was observed. It is believed that the metallic nanotubes reorganise in the film, or more likely are "burnt out" due to Joule heating during this electrical annealing. This theory is supported by atomic force microscopy evidence [8]. The current versus voltage characteristics are shown in Figure 8.15 before and after electrical annealing. There is a significantly lower overall conductivity following this electrical annealing process. The linearity of the characteristic has also changed after annealing, beforehand showing an almost linear response and afterwards showing a nonlinear characteristic, suggesting a voltage dependent resistance.

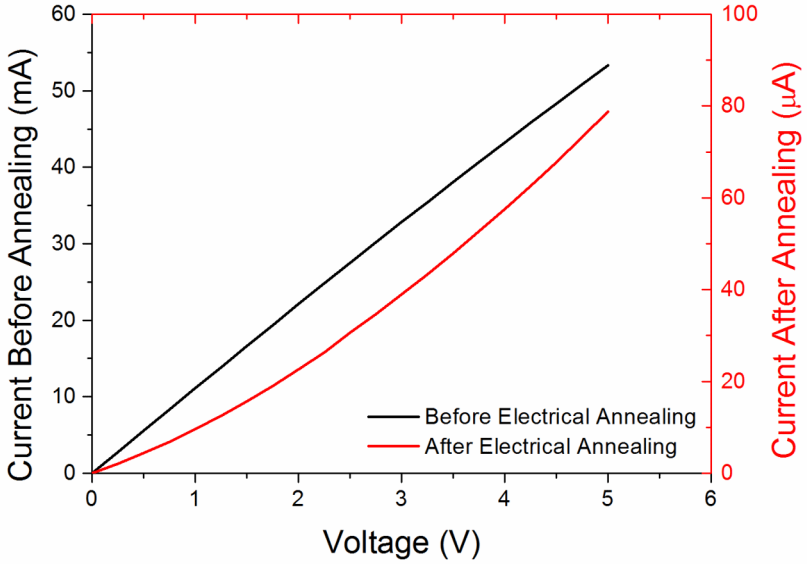

Figure 8.15: *In plane, room temperature current versus voltage characteristics for a 29-layer LB SWCNT-U network on 5 μm electrodes before and after electrical annealing.*

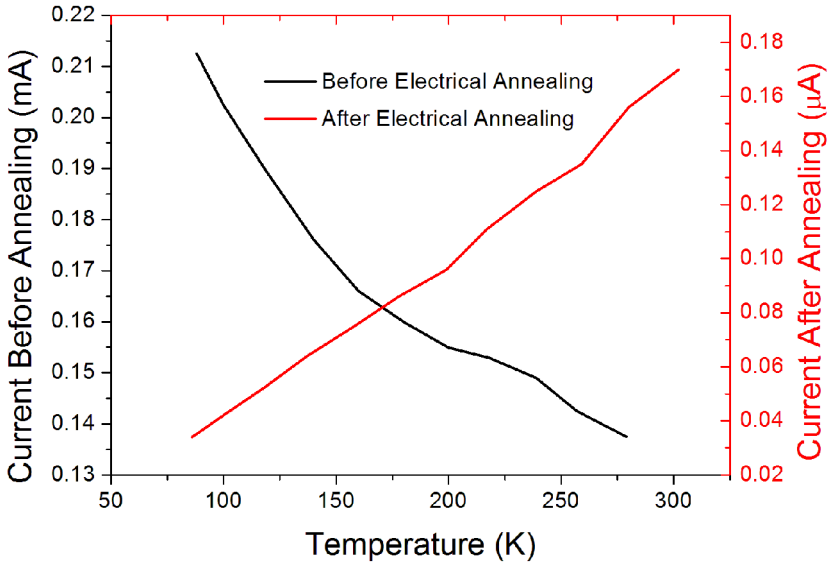

Figure 8.16: *Current versus temperature characteristic for a 29-layer LB SWCNT-U network on 5 μm electrodes before and after electrical annealing.*

The temperature dependence of the current is shown in Figure 8.16 measured at a fixed voltage of 1 V. The two curves shown are for before and after an electrical annealing step, showing a change from a metallic temperature dependence to semiconducting after annealing. The majority of nanotubes in this mixed material are semiconducting. Therefore, it is expected that the majority of pathways between the electrodes will be dominated by semiconducting to semiconducting or semiconducting to metallic SWCNT junctions. However, in some cases it is also possible for metallic nanotubes to form a percolating pathway, explaining the (infrequent) observations of a metallic temperature dependence, before any annealing.

8.4 Conductivity Mechanisms

To understand the physical processes at work in SWCNT-S and SWCNT-M nanotube networks, current versus voltage sweeps were taken across a wide range of temperatures (80 K to 350 K) on electrodes of varying spacing (220 nm, 50 µm and 2 mm). Based on previous results, palladium electrodes were used in the following section to make contacts to the nanotube networks (unless otherwise stated). The networks were thermally annealed following LB deposition to improve the electrode contact.

8.4.1 Metallic Nanotubes

Current versus voltage characteristics for a thermally annealed 5-layer SWCNT-M LB network at temperatures between 80 K to 350 K are shown in Figure 8.17; the electrode spacing was 220 nm. The current versus voltage curves are linear at all temperatures, in contrast to the nonlinear responses at lower temperatures for SWCNT-S reviewed later in this section.

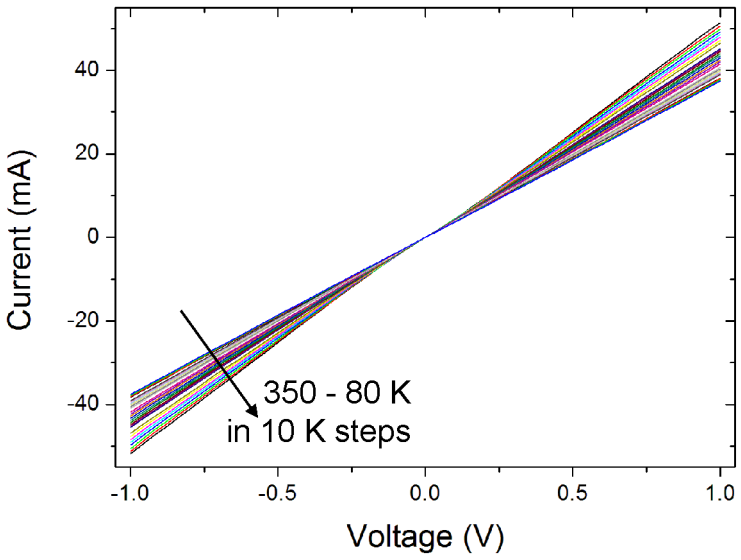

Figure 8.17: *Current versus voltage plots for a thermally annealed 5-layer SWCNT-M LB network at varying temperatures on palladium electrodes with a spacing of 220 nm.*

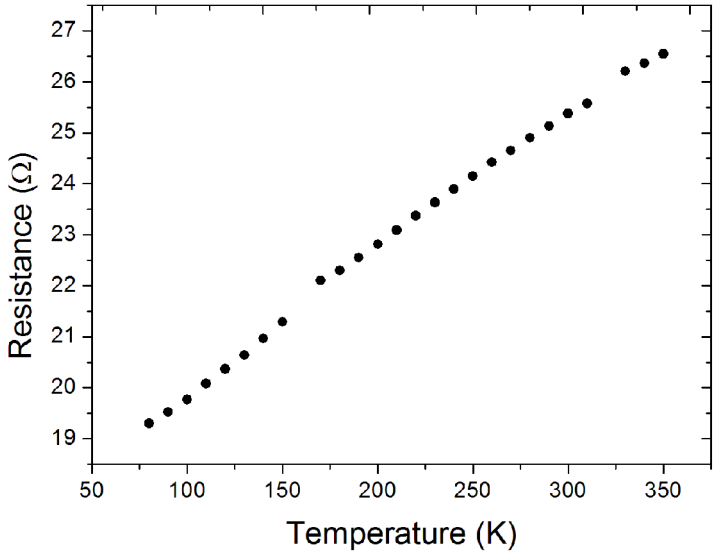

Figure 8.18: *Resistance versus temperature for the same data as presented in Figure 8.17.*

The resistance versus temperature data at a fixed voltage (1 V) are shown in Figure 8.18. The resistance of the network decreases with decreasing temperature, as expected for metallic conduction. The resistance versus temperature relationship can be approximated by a linear relationship

$$R(T) = R_0[1 + \alpha(T - T_0)] \tag{8.1}$$

where R_0 and T_0 are a fixed resistance and temperature (in this case 25.4 Ω at 300 K). The temperature coefficient of resistance (α) can be calculated from Figure 8.18, giving a value of 0.001/K. This value is comparable to other published work, for example, 0.0026/K [10].

8.4.2 Semiconducting Nanotubes

Semiconducting SWCNTs were tested in the same way, using submicron spaced electrodes with an electrode separation of 220 nm. Measurements with electrode separations of 50 µm and 2 mm were also taken to study the conduction mechanisms at work in the networks.

The current versus voltage curves for a thermally annealed 5-layer SWCNT-S LB network at temperatures between 80 K to 350 K are shown in Figure 8.19 for an electrode spacing of 220 nm. As expected for a semiconducting material, the network resistance increases at lower temperatures, however the linearity of the response varies according to temperature. Above 150 K, the current is almost proportional to the voltage. As the temperature is reduced below 150 K the responses become increasingly nonlinear.

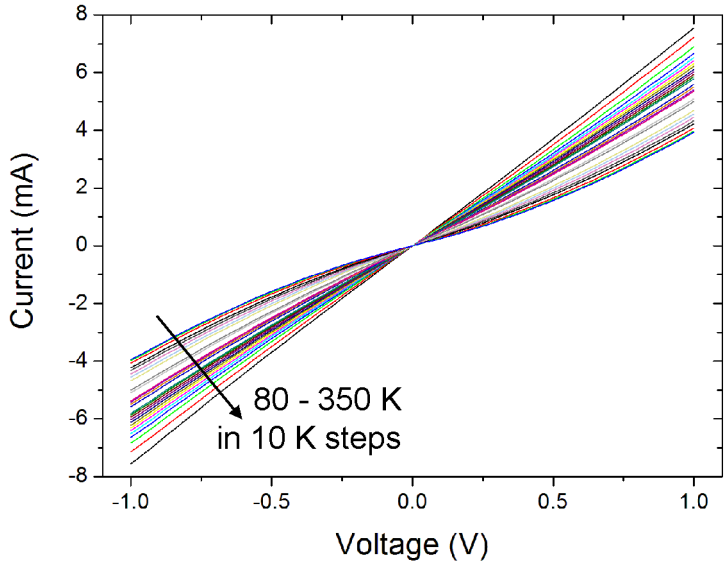

Figure 8.19: *Current versus voltage plots for a thermally annealed 5-layer SWCNT-S LB network at varying temperatures on palladium electrodes with a spacing of 220 nm.*

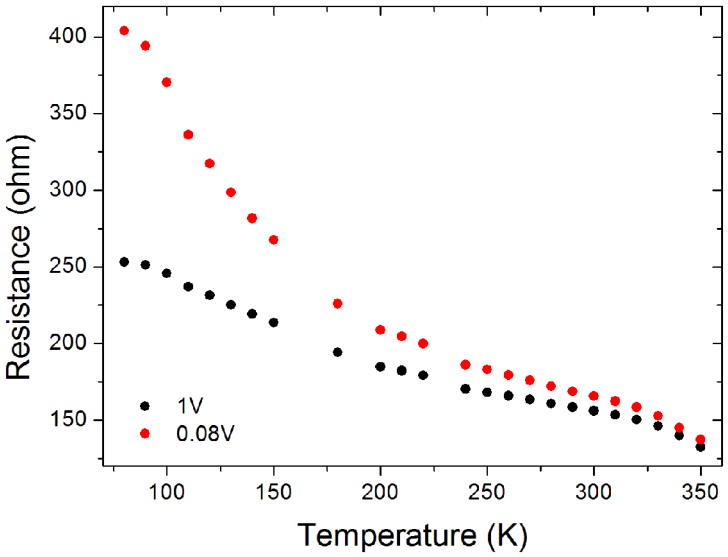

Figure 8.20: *Resistance versus temperature for the same data as presented in Figure 8.19.*

Plots of resistance versus temperature at two different voltages (1 V and 0.08 V) are shown in Figure 8.20. This shows that the resistance of the SWCNT-S network depends on the applied voltage, particularly below 150 K. These data are consistent with those shown in Figure 8.19, revealing an increasing nonlinearity in the current versus voltage characteristics below 150 K.

Figure 8.21 shows the same data again, this time plotted in the form of a logarithm (current) versus the reciprocal of temperature at two different applied voltages. These Arrhenius plots do not reveal a straight line fit, as might be expected for a crystalline semiconductor dominated by a single impurity level. If the classical single crystal semiconductor model were appropriate, this suggests multiple impurity levels present within the band gap of the carbon nanotube. A range of activation energies between 1 meV to 41 meV can be calculated from Figure 8.21. Typical figures reported in the literature range from about 29 meV for individual un-doped nanotubes [11] to between 10 meV and 20 meV for layer-by-layer networks [12].

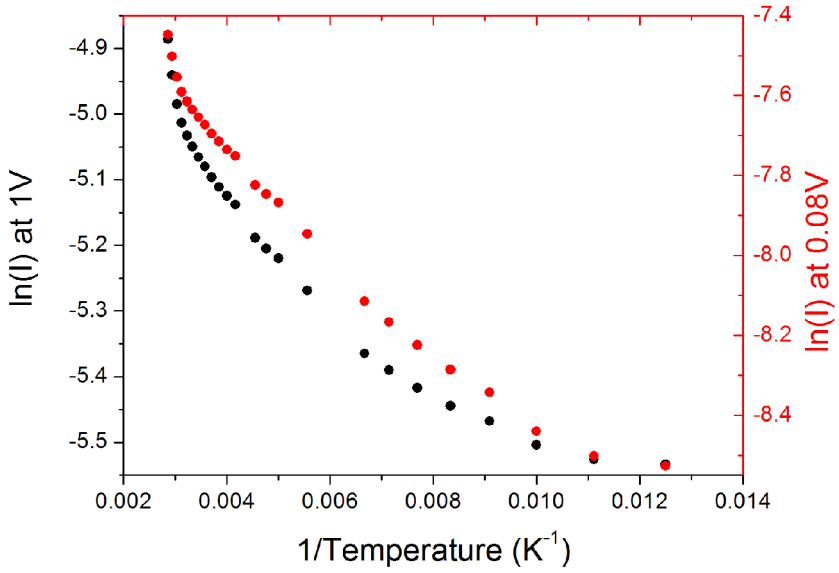

Figure 8.21: *Arrhenius plot for the same data as presented in Figure 8.19.*

There are a number of different physical processes that could account for the electrical conductivity of the SWCNT-S thin film network, which have been reported in the literature [11, 12, 13]. From the work with different metals and electrode separations (Section 8.2) it is assumed that conductivity in the SWCNT-S network is dominated by bulk rather than contact effects. Quantum mechanical tunnelling and variable range hopping [14] between the individual tubes have been considered as possible conductivity mechanisms to explain the electrical conduction in unsorted (i.e. mixed semiconducting and metallic) carbon nanotube networks. Schottky emission and the Poole-Frenkel effect have also been considered.

Poole-Frenkel Conduction

The resistance versus temperature data for a 5-layer SWCNT-S network shown in Figure 8.20 reveal that, at low temperatures, the conductivity is dependent on the applied electric field. Previous work has suggested that Poole-Frenkel conduction provides a good explanation for the conductivity of unsorted SWCNT networks deposited by electrostatic layer-by-layer deposition [12]. Therefore, Poole-Frenkel conduction should also be considered as a possible mechanism for conduction in sorted SWCNT-S networks. This is a bulk-limited process that operates at high electric fields ($>10^6$ V/m) in which the conduction is determined by energy barriers surrounding charged traps (Section 4.2.4). The current versus voltage dependence is given by

$$I \propto V exp\left(-\frac{E_d - \beta_{PF} V^{\frac{1}{2}}}{kT}\right) \tag{8.2}$$

where E_d is the barrier height and β_{PF} is the Poole-Frenkel constant, given by

$$\beta_{PF} = \left(\frac{e^3}{\pi \epsilon_0 \epsilon_r}\right)^{\frac{1}{2}} \tag{8.3}$$

where ϵ_0 is the permittivity of free space and ϵ_r is the relative permittivity of the medium.

Figure 8.22 shows the previous data plotted to reveal Poole-Frenkel conductivity of the form $ln(I/V)$ versus $V^{1/2}$. This provides a good fit to the data at temperatures below 150 K and at applied voltages of greater than 0.25 V (corresponding to an electric field of 1.7×10^6 V/m). This dependence on the field at lower temperatures supports the observation made from Figure 8.19 of an increasing nonlinearity in the current versus voltage response at lower temperatures.

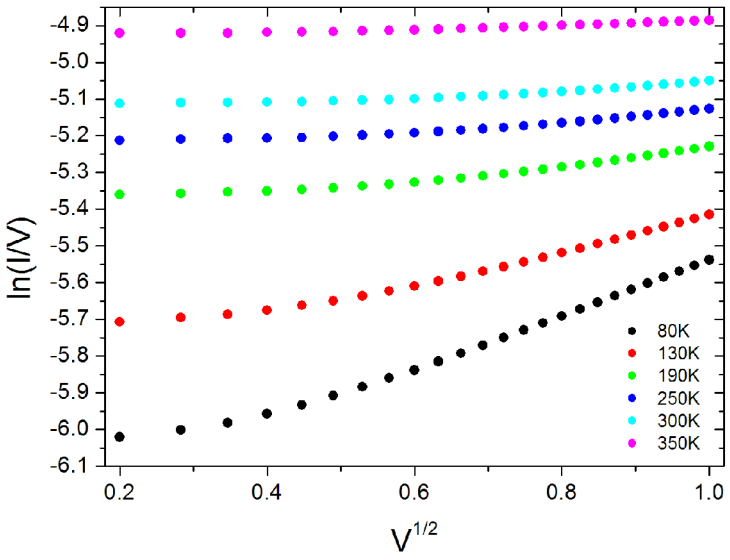

Figure 8.22: *Poole-Frenkel voltage dependance at fixed temperatures for the same data as presented in Figure 8.19.*

If the conductivity is assumed to be determined by the Poole-Frenkel process and equations 8.2 and 8.3 are used, a figure for the relative permittivity was calculated to be 984 at 80 K. This is significantly higher than values reported in previous work of between 6 and 22 [15]. Ellipsometry data for similarly prepared networks (Section 7.3.2) revealed much smaller permittivities, in-line with reported values. However, the permittivity extracted from the Poole-Frenkel fitting is consistent with reports in the literature of composite nanotube-polymer networks having very high dielectric

constants, with values up to 9000 at low frequencies [16, 17]. This is accounted for by the nanotubes being in very close proximity to each other, and close to the percolation threshold but remaining insulated by thin regions of polymer within the film. The film can then be regarded as a microcapacitor network leading to the high values of permittivity as a result of the build up of charge at the interfaces. It is likely that the SWCNT-S thin networks deposited on an insulating (glass) substrate behave in a similar manner with large permittivity values recorded at very low frequencies (or in this case with DC current).

Across much larger electrode gaps (2 mm), the current versus voltage curves show a linear response over the entire temperature range as shown in Figure 8.23. The main difference with the larger electrode gaps being that the electric field strength is orders of magnitude smaller than that of the submicron electrode gaps. The Poole-Frenkel effect involves the lowering of a potential barrier under the influence of an electric field, with these larger electrode gaps there is insufficient energy to lower the barrier.

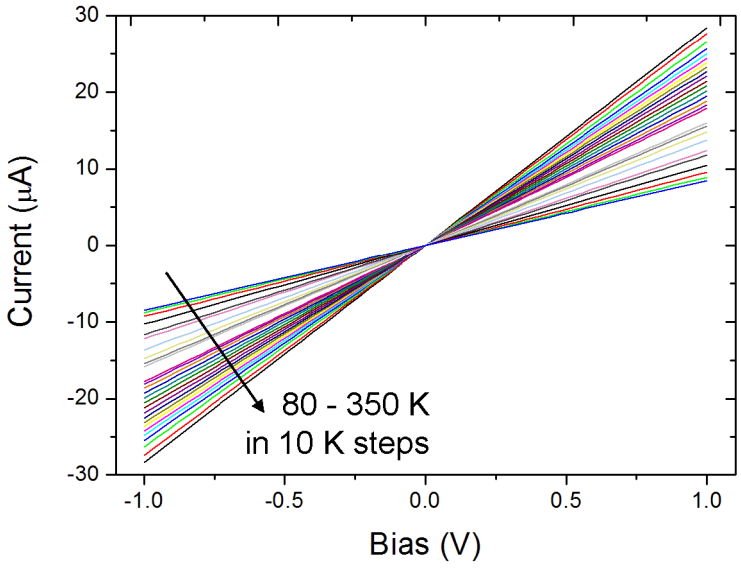

Figure 8.23: *Current versus voltage plots for a 5-layer SWCNT-S LB network at varying temperatures on palladium electrodes with a spacing of 2 mm.*

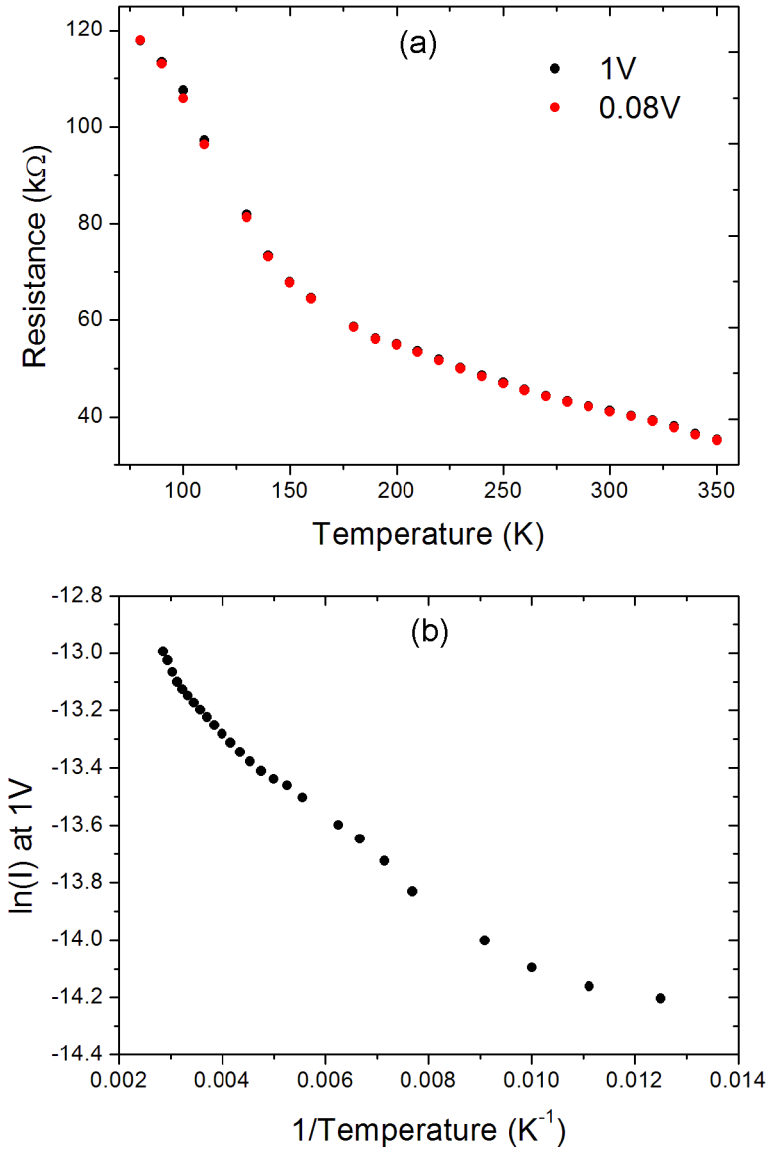

Figure 8.24: *Resistance versus temperature (a) and Arrhenius plot (b) for the same data as presented in Figure 8.23.*

Figure 8.24(a) shows the resistance versus temperature response for the same data at two different applied voltages (1 V and 0.08 V). No voltage dependence is evident for the resistance, in contrast to the results obtained with submicron electrode separations, where it was suggested that Poole-Frenkel conductivity was dominant. An Arrhenius plot for the same data is shown in Figure 8.24(b), the activation energies range from 3.7 meV to 34.6 meV, similar to those from the submicron spaced electrodes (Figure 8.21).

8.4.3 Other Conductivity Models

Although Poole-Frenkel conduction showed the best fit to the experimental data, other fits were also investigated for the semiconducting SWCNTs as outlined in the following section. Tunnelling was dismissed as a dominant mechanism. A much larger temperature dependence of conductivity was observed than one would expect from Equation 4.3, if tunnelling was dominating conductivity.

Schottky Emission

The current versus voltage dependence for conductivity dominated by the Schottky effect (Section 4.2.3) can be written as

$$I \propto AT^2 exp\left(-\frac{E}{kT}\right) = AT^2 exp\left(-\frac{E_0 - \beta_S V^{\frac{1}{2}}}{kT}\right), \tag{8.4}$$

where A is the Richardson coefficient, E is the Schottky barrier height, E_0 is the barrier height at zero field, k is the Boltzmann constant, T is the temperature and β_S is the Schottky coefficient. The following relationships can be tested with experimental data to investigate whether or not Schottky conduction is a significant process:

(a) Voltage dependence

$$ln\left[\frac{I}{T^2}\right] \propto V^{\frac{1}{2}} \quad \textbf{or} \quad ln[I] \propto V^{\frac{1}{2}} \text{ (at fixed temperature).} \tag{8.5}$$

(b) Temperature dependence

$$ln\left[\frac{I}{T^2}\right] \propto \frac{1}{kT} \text{ (at constant voltage).} \tag{8.6}$$

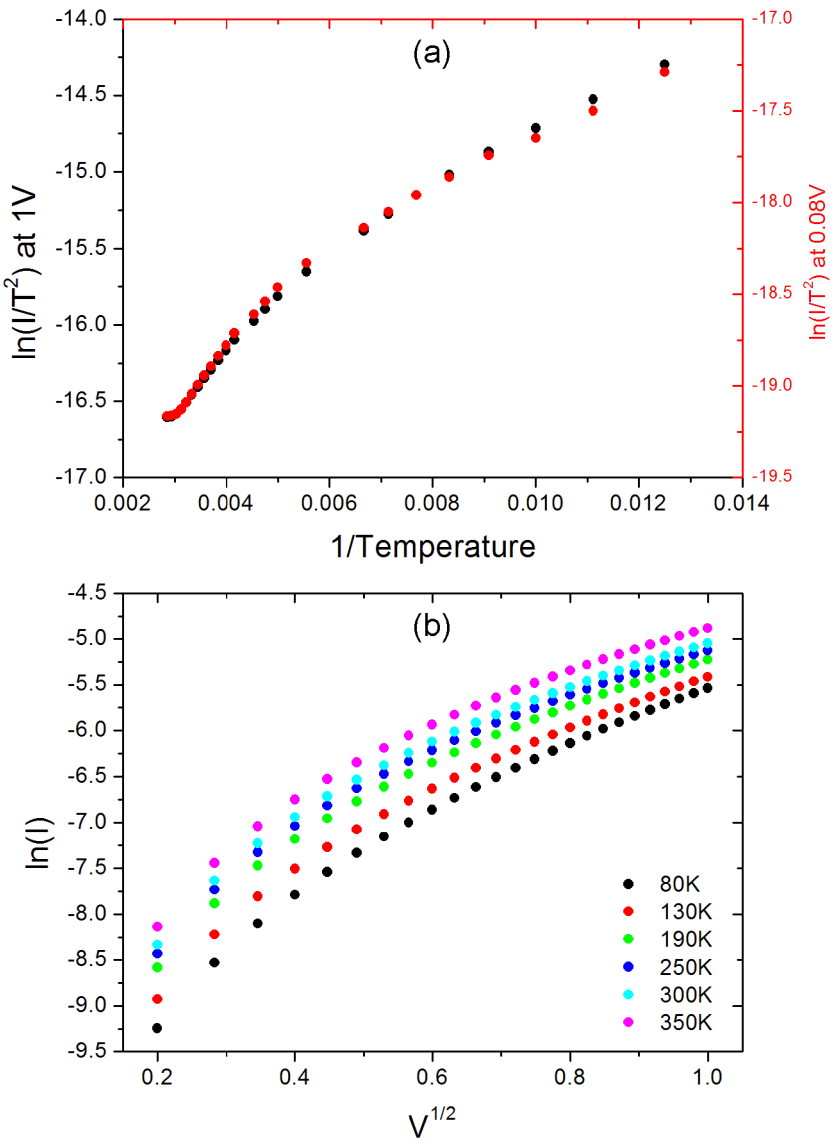

Figure 8.25: *Schottky voltage dependence (a) and temperature dependence (b) for a 5-layer SWCNT-S network deposited on submicrometer palladium electrodes.*

Figure 8.25(a) shows the temperature dependence for Schottky emission at a fixed voltage, (b) shows the same data plotted to reveal the voltage dependence of Schottky emission at fixed temperatures. Neither graph shows a good fit to the data, thus Schottky emission was discounted as a dominant transport mechanism in the SWCNT-S networks.

Variable Range Hopping

Another theory to explain the conductivity in random networks of carbon nanotubes is variable range hopping (VRH). In this conduction mechanism, conductivity across networks is dominated by tube interactions rather than the nature of the individual nanotubes. Charges will "hop" via a tunneling mechanism between nanotubes present in bundles within the network facilitating conduction. Variable ranging hopping has been reported as a possible method of electrical conduction in SWCNT networks [13, 18].

Variable range hopping is given by

$$G(T) = G_0 exp\left[-\left(\frac{T_0}{T}\right)^{(\frac{1}{1+d})}\right] \tag{8.7}$$

where $G(T)$ is the conductance at a given temperature, T, G_0 is the conductance at a set temperature, T_0 and d is the number of dimensions.

If logarithms are taken, the temperature dependence of conductivity can be found

$$ln(G) \propto T^{\frac{1}{1+d}} \tag{8.8}$$

where G is the conductance, T is the temperature and d is the number of dimensions. Figure 8.26 shows the data for a 5-layer SWCNT-S network with electrodes of (a) 220 nm and (b) 2 mm spacing plotted to reveal VRH conduction, of the form $ln(I)$ versus $T^{-1/3}$ for VRH in 2 dimensions. For the narrow channel case (a), there is no clear fit to the data to support variable range hopping. Although there is a relatively linear relationship in the mid part of the data, this quickly diverges from linearity at the extremes of temperature. One would not expect VRH to be

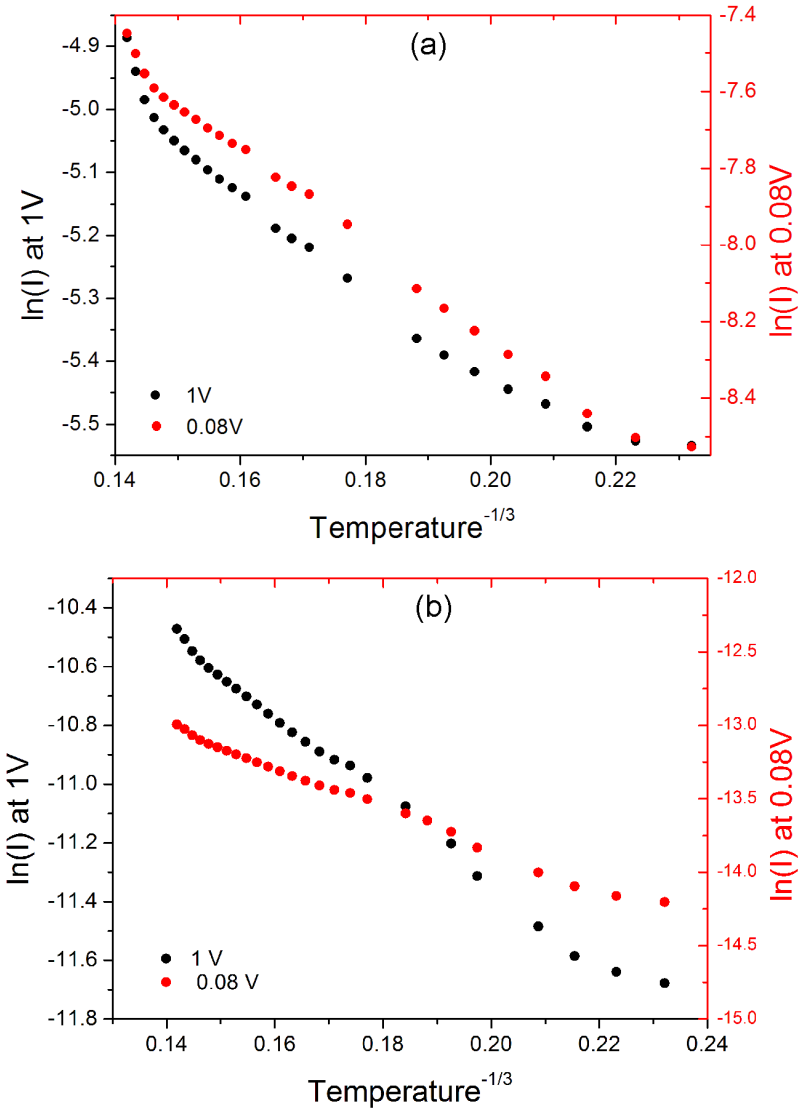

Figure 8.26: *Ln(I) versus temperature$^{-1/3}$ plot for variable range hopping in a 5-layer SWCNT-S network with electrodes of (a) 220 nm and (b) 2 mm spacing.*

the dominant mechanism in networks with such a narrow electrode gap since the nanotubes themselves are approximately 1 µm (significantly longer than the channel) in length there should be little hopping from tube to tube between the electrodes. When the same network is measured over a larger gap (b) of 2 mm there is a slightly more linear fit, with less divergence at the temperature extremes. Although this would be the expected behaviour in a larger scale network of SWCNT-S, the data do not show a suitable fit to support the VRH mechanism so it has been ruled out as a dominant mechanism for this work.

8.5 Conclusions

A good metal to nanotube contact is required for reliable electrical measurements. A series of metals were therefore explored, with palladium and gold showing good Ohmic contacts. Aluminium proved to be the least reliable material. Measurements over different electrode separations revealed a current that approximately scaled with electrode separation, thus ruling out contact effects dominating the conductivity. Thermal annealing further improved contact formation by cleaning the surface of any residual material present in the nanotube solutions. An optimum anneal time of 30 min was chosen as this yielded the largest gain in conductivity for the amount of time. Various conductivity mechanisms were investigated, including variable range hopping, Poole-Frenkel conduction and Schottky emission. The Poole-Frenkel effect provided the best fit to the experimental data as the dominant conduction mechanism for high electric fields ($>10^6$ V/m) and explains the observation of increasing nonlinear current versus voltage responses as the temperature was reduced. The metallic nanotubes exhibited a metallic temperature dependence as expected, with a temperature coefficient of resistance of 0.001/K.

References

[1] D. R. Lide, *CRC Handbook of Chemistry and Physics, 89th edition.* CRC Press, 2008.

[2] L. Hu, D. S. Hecht, and G. Grüner, "Carbon nanotube thin films: Fabrication, properties and applications," *Chem. Rev.*, vol. 110, no. 10, pp. 5790–5844, 2010.

[3] D. Mann, A. Javey, J. Kong, Q. Wang, and H. Dai, "Ballistic transport in metallic nanotubes with reliable Pd Ohmic contacts," *Nano Lett.*, vol. 3, no. 11, pp. 1541–1544, 2003.

[4] Z. Chen, J. Appenzeller, J. Knoch, Y. Lin, and P. Avouris, "The role of metal-nanotube contact in the performance of carbon nanotube field-effect transistors," *Nano Lett.*, vol. 5, no. 7, pp. 1497–1502, 2005.

[5] Y. Woo, G. S. Duesberg, and S. Roth, "Reduced contact resistance between an individual single-walled carbon nanotube and a metal electrode by a local point annealing," *Nanotechnology*, vol. 18, no. 9, p. 095203, 2007.

[6] Y. Zhang, T. Ichihashi, E. Landree, F. Nihey, and S. Iijima, "Heterostructures of single-walled carbon nanotubes and carbide nanorods," *Science*, vol. 285, pp. 1719–1722, 1999.

[7] J.-O. Lee, C. Park, J.-J. Kim, J. Kim, J. W. Park, and K.-H. Yoo, "Formation of low-resistance Ohmic contacts between carbon nanotube and metal electrodes by a rapid thermal annealing method," *J. Appl. Phys. D*, vol. 33, pp. 1953–1956, 2000.

[8] C. Venet, C. Pearson, A. S. Jombert, M. F. Mabrook, D. A. Zeze, and M. C. Petty, "The morphology and electrical conductivity of single-wall carbon nanotube thin films prepared by the Langmuir-Blodgett technique.," *Colloids and Surfaces A*, vol. 354, pp. 113–117, 2010.

[9] T. Fukao, S. Nakamura, H. Kataura, and M. Shiraishi, "Solution-processed single-walled carbon nanotube transistors with high mobility and large on/off ratio," *Japanese Journal of Applied Physics*, vol. 45, no. 8A, pp. 6524–6527, 2006.

[10] E. Pop, D. A. Mann, K. E. Goodson, and H. Dai, "Electrical and thermal transport in metallic single-wall carbon nanotubes on insulating substrates," *J. Appl. Phys.*, vol. 101, p. 093710, 2007.

[11] V. Skákalová, A. B. Kaiser, Y. S. Woo, and S. Roth, "Electronic transport in carbon nanotubes: From individual nanotubes to thin and thick networks," *Phys. Rev. B*, vol. 74, p. 085403, 2006.

[12] A. S. Jombert, K. S. Coleman, D. Wood, M. C. Petty, and D. A. Zeze, "Poole-Frenkel conduction in single wall nanotube composite films built up by electrostatic layer-by-layer deposition," *J. Appl. Phys.*, vol. 104, p. 094503, 2008.

[13] K. Yanagi, H. Udoguchi, S. Sagitani, Y. Oshima, T. Takenobu, H. Kataura, T. Ishida, K. Matsuda, and Y. Maniwa, "Transport mechanisms in metallic and semiconducting single-wall carbon nanotube networks," *ACS Nano*, vol. 4, no. 7, pp. 4027–4032, 2010.

[14] C. Morgan, Z. Alemipour, and M. Baxendale, "Variable range hopping in oxygen-exposed single-wall carbon nanotube networks," *Phys. Stat. Sol. (a)*, vol. 205, no. 6, pp. 1394–1398, 2008.

[15] M. K. Massey, C. Pearson, D. A. Zeze, B. Mendis, and M. C. Petty, "The electrical and optical properties of orientated Langmuir-Blodgett films of single-walled carbon nanotubes," *Carbon*, vol. 49, pp. 2424–2430, 2011.

[16] J. K. Yuan, S. H. Yao, Z. M. Dang, A. Sylvestre, M. Genestoux, and J. Bai, "Giant dielectric permittivty nanocomposites: realizing true potential of pristine carbon nanotubes in polyvinylidene fluoride matrix through an enhanced interfacial interaction," *J. Phys. Chem.*, vol. 115, pp. 5515–5521, 2011.

[17] X. Zhao, A. A. Koos, B. T. T. Chu, C. Johnston, N. Grobert, and P. S. Grant, "Spray deposited fluoropolymer/multi-walled carbon nanotube composite films with high dielectric permittivity at low percolation threshold," *Carbon*, vol. 47, pp. 561–569, 2009.

[18] M. Jaiswal, W. Wang, K. A. S. Fernando, Y.-P. Sun, and R. Menon, "Charge transport in transparent single-wall carbon nanotube networks," *Journal of Physics: Condensed Matter*, vol. 19, no. 44, p. 446006, 2007.

Chapter 9

Field Effect Transistor Devices

9.1 Introduction

This chapter will provide an overview of some exploratory work into using nanotubes as the active semiconductor in field effect transistors (FETs). Fabrication of the devices is included in this chapter with a few different electrode layouts discussed. Some FETs are based on organic insulators, others with silicon dioxide as the insulator. Devices with large (>50 µm) source drain separations based on organic dielectrics are presented. Smaller (<1 µm) source drain separations are also presented along with the challenges encountered.

9.2 Field Effect Transistor Device Preparation

9.2.1 Long Channel Devices (>50 µm)

Bottom gate field effect transistors (FETs) were built up on borosilicate slide glass using standard techniques. A gate was formed by evaporating ∼30 nm of aluminium through a shadow mask (Figure 9.1(a)) on to a glass slide, which had been cleaned following the process explained in Section 5.2. Poly(methyl methacrylate) (PMMA), prepared in anisole solution to a concentration of 4.8 wt%, was then spin coated to a thickness of 150 nm following a previously described method to act as the dielectric layer[1]. An initial spin speed of 500 rpm for 10 s was used to spread the solution, then a speed of 3000 rpm for 50 s was used to reduce the thickness of the film. The substrate was then heated at 110 °C for 60 min. Gold source and drain electrodes were evaporated though a shadow mask (Figure 9.1(b)) to a thickness of ∼50 nm.

Figure 9.1: *Shadow masks used for evaporating (a) aluminium gate and (b) gold source and drain electrodes*

Different source drain separations and widths were used to allow for measurements of different channel dimensions. Table 9.1 shows a summary of the channel dimensions of the shadow mask.

Channel length (µm)	Channel width (mm)	Channel length (µm)	Channel width (mm)
200	4	50	4
200	2	50	2
100	2	50	1
100	1	50	0.5

Table 9.1: *Table showing channel dimensions of the shadow mask used for source and drain evaporations*

Single-walled semiconducting nanotubes were deposited by Langmuir-Blodgett deposition either directly on top of the dielectric (Figure 9.2(a)), or on top of the source drain electrodes (Figure 9.2(b)) to form the active layer of the device.

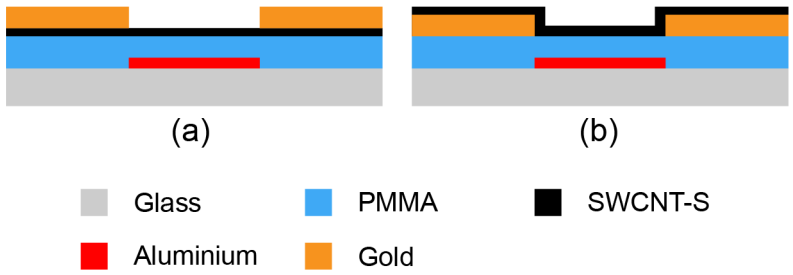

Figure 9.2: *Cross section of the FET structure, showing (a) nanotubes directly on top of the dielectric and (b) nanotubes on top of the source drain electrodes*

9.2.2 Short Channel Devices (<1 µm)

Field effect transistors devices were also built up on silicon substrates with submicron source drain separations. Thermally grown silicon dioxide on highly doped silicon was used as the gate dielectric, with the silicon substrate acting as a common gate electrode. Figure 9.3 shows two different device structures that were used: one with a uniform thin oxide and a second with a patterned thick oxide in an attempt to reduce leakage (see Section 9.3 for further discussion). The source and drain electrodes were fabricated in a similar manner to the submicron electrodes described in Section 5.5.2. Aluminium was used as the electrode material for the thin oxide

devices with aluminium and gold being used for the thick oxide devices.

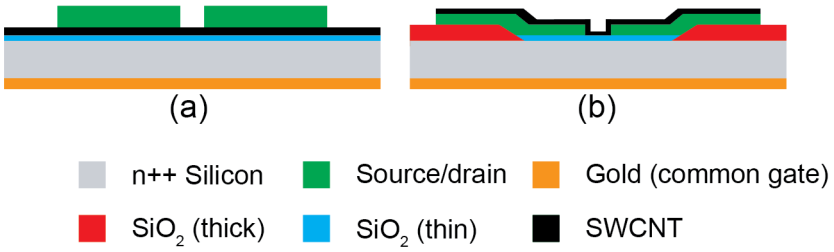

Figure 9.3: *Cross section diagram showing the two sub micron channel length FETs with (a) having a uniform thin oxide and (b) having a patterned thick oxide.*

9.3 Short Channel Silicon Based Devices

Short channel devices were fabricated with source-drain separations of only a few hundred nanometres as described in Section 9.2.2. Some of the more successful CNT FET devices reported in the literature are fabricated with single nanotubes or only small bundles of nanotubes spanning the gap rather than random interconnected networks of nanotubes between larger channel lengths (>5 µm) [2, 3, 4]. These devices were built up on silicon/silicon dioxide wafers to aid in fabrication since the etching chemicals involved in producing the electrodes were not compatible with the PMMA dielectric. Two variations on the electrode structure were investigated, one with a uniform thin oxide (100 nm) over the wafer and the second with a patterned thicker oxide (200 nm) over the majority of the substrate with thin regions where the source drain electrodes were patterned.

Thin Oxide

All devices showed large leakage, so electrical characterisation was not possible. The large leakage was attributed to defects in the oxide, allowing nanotubes to

short through to the gate. Although the devices showed poor characteristics, SEM imaging revealed uniform films of SWCNTs deposited by LB over large areas of the substrate as shown in Figure 9.4. The channel is in the centre of the image (approximately 500 nm in length), with aluminium source-drain electrodes either side deposited on top of the carbon nanotubes.

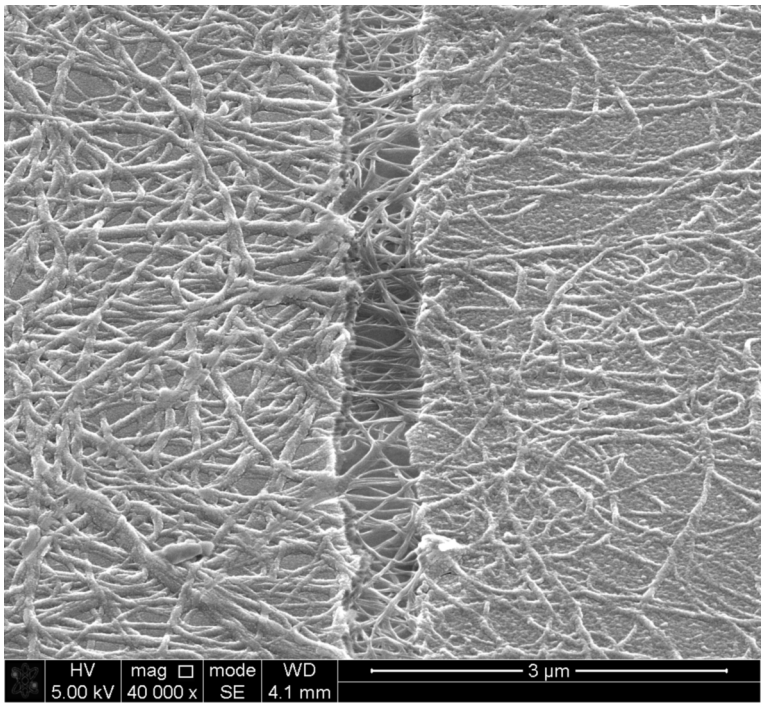

Figure 9.4: *SEM image of a transistor fabricated on silicon with a 7-layer SWCNT-S LB film below aluminium electrodes.*

Patterned Thick Oxide

As discussed in the previous section, the thin silicon dioxide insulating layer contained defects resulting in high leakage currents. This made recording any meaningful measurements impossible. To alleviate this problem, a thicker oxide was grown on the silicon and then patterned to define regions where a thin oxide would be grown. By patterning the thin regions of oxide, the chance of pinhole defects causing shorts was reduced. The conducting channel between the source-drain electrodes was positioned so it lay over this thin oxide region. A detailed

description of this process can be found in the experimental methods section (Section 9.2).

Multiple devices were fabricated on each 4 inch silicon wafer and were cut down to a suitable size for LB deposition. Figure 9.5 shows the layout of devices on a substrate used for LB deposition. The source drain current is shown for each device at a voltage of 2.5 V with a gate voltage of 0 V. As can be seen the film of SWCNT-S covers the eight devices to the right of the figure and these show varying levels of conductivity reflecting the random nature of the nanotube film.

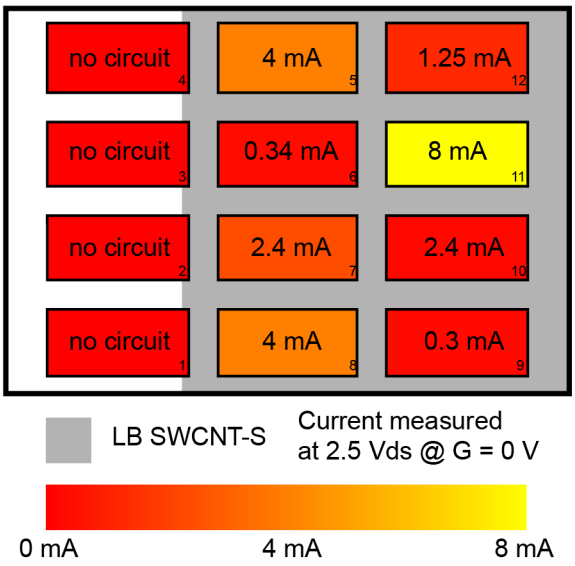

Figure 9.5: *Diagram showing the source drain currents of multiple devices on a substrate with a 7-layer SWCNT-S LB film deposited directly on the SiO_2.*

The output characteristics are shown in Figure 9.6 for one of the devices from Figure 9.5. Gate voltages from 0 V to −15 V have been applied with a source-drain voltage from −5 V to 5 V. The response is nonlinear due to aluminium being used as the electrode material (see Section 8.2 for more details on this). As can be seen there is little leakage current through the device, with all curves passing through the origin. There is only a marginal field effect observed with the source drain current reducing by approximately 0.25 mA with a 15 V negatively biased gate. As planned, the leakage current has been reduced compared with the thin oxide devices, however

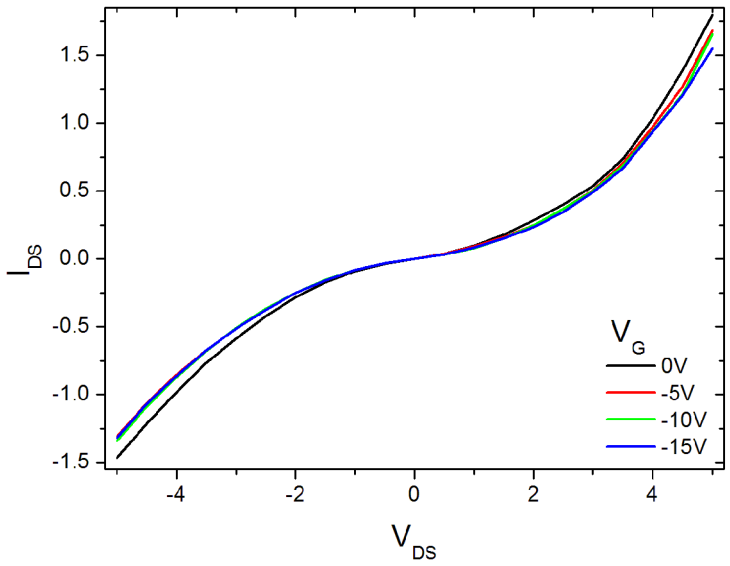

Figure 9.6: *Output characteristics for a SWCNT FET based on the patterned thick oxide structure with a 7-layer LB film of sorted SWCNT-S as the active layer .*

there is still an underlying issue with the devices, firstly with the channel always being 'on' and as a result exhibiting no significant dependence on the gate voltage. It is possible that with the very small channel width, any remaining metallic nanotubes in the sorted semiconducting material are dominating the conductivity and shielding any field dependencies that the semiconducting nanotubes might be exhibiting.

9.4 Top Gated Organic Short Channel Devices

The palladium submicron spaced electrodes on glass were used to fabricate top gated field effect transistor structures using PMMA as the dielectric. SWCNT-S were deposited by the LB method on palladium electrodes followed by a 150 nm thick layer of PMMA to act as the dielectric. An aluminium gate was then evaporated through a shadow mask. Due to the rough nature of the nanotube film, shorting occurred through the dielectric to the gate, rendering all devices unusable.

9.5 Long Channel Organic Based Devices

Using previously proven techniques for pentacene based transistors [1] , structures were built up following the same methods, but with SWCNTs as the active material in the device. An overview of this process is given in Section 9.2.1. Two different types of SWCNT were used, unsorted HiPCO nanotubes and sorted semiconducting nanotubes.

Unsorted HiPCO SWCNT

The first devices tested were fabricated with unsorted HiPCO SWCNT-U as the active layer in the device. Unsorted SWCNTs were deposited on top of the gold source-drain electrodes to a thickness of 7 LB layers. Several devices were tested with a mixture of results, some showing leakage and some showing little or no conductivity between the source-drain electrodes. Figure 9.7 shows the typical output characteristics of a 'good' device with a plot of the source-drain current

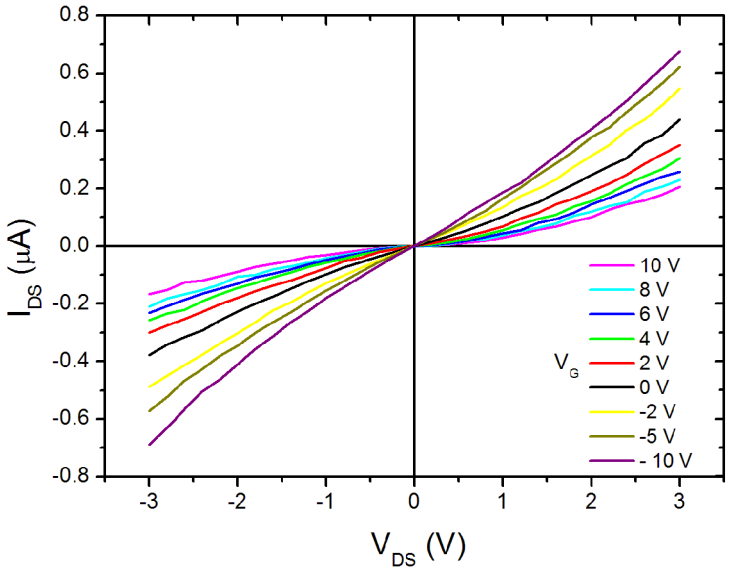

Figure 9.7: *Output characteristics for a SWCNT FET with a 5-layer LB film of unsorted SWCNT-U as the active layer.*

at different values of gate bias. All of the curves pass through the origin signifying very low leakage currents (not observable on this data scale). The device is turned on at zero gate-source voltage, a positive gate voltage reduces the current through the device. As the gate bias is increased to more negative values, this increases the conductivity between the source and drain. This is typical for depletion mode p-type transistor behaviour. P-type behaviour is common for CNT FET devices in air [5].

The field effect mobility, μ, was calculated in the linear region of the transistor using Equation 4.15. An estimated gate capacitance was used based on devices fabricated following the same techniques [6]. The value of μ was evaluated using the gradient from the plot of I_{DS} versus V_{DS}, and was found to be $\sim 0.3\,\mathrm{cm}^2/\mathrm{Vs}$. This is low compared to the majority of reported CNT FET mobilities, a selection of which are given in Table 2.1, reflecting the non-optimised nature of the devices.

The drain-source current versus gate-source voltage transfer characteristic at a fixed source-drain voltage of 1 V is shown in Figure 9.8. The modulation in drain-source

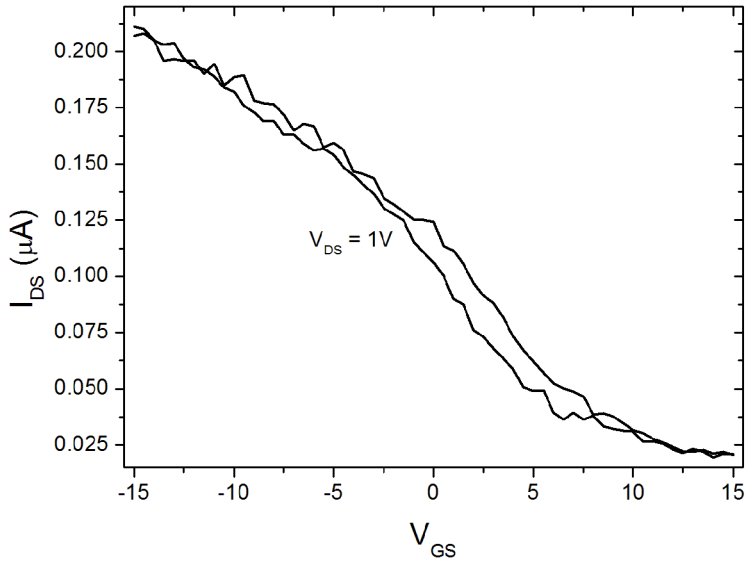

Figure 9.8: *Transfer characteristic for a SWCNT FET with a 5-layer LB film of unsorted SWCNT-U as the active layer.*

current achieved is relatively low. With the gate voltage at its most positive (15 V), 0.025 µA flows through the channel. At its most negative (−15 V) the current increases to 0.2 µA, showing an on/off ratio of around 8. Again, this is lower than the majority of reported devices (Table 2.1).

SWCNT-S

In an attempt to improve the FET characteristics, in particular improving the on/off ratio, sorted semiconducting nanotubes were used as the active layer in devices fabricated in the same manner to the previous section. It is noted in the literature, that the presence of metallic nanotubes can severely reduce the on/off ratio [7, 8]. Nanotube FETs fabricated with sorted material exhibit greatly improved on/off ratios and mobilities [2, 9, 10]. Figure 9.9 shows the output characteristics for an FET with 2 LB-layers of sorted SWCNT-S as the active layer. Despite being 98 % pure semiconducting nanotubes, the output characteristics of the FET, if anything, are worse than the previous devices fabricated with unsorted SWCNT, showing

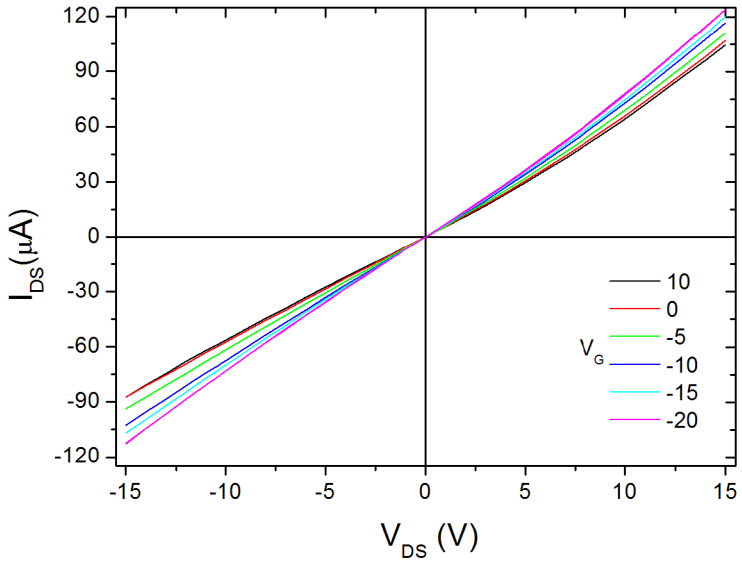

Figure 9.9: *Output characteristics for a SWCNT FET with a 2-layer LB film of sorted SWCNT-S as the active layer.*

even less field effect. The devices do show greater resilience to applied voltage, with 15 V showing no sign of breakdown between the source-drain electrodes. This is attributed to improved deposition with the SWCNT-S forming much more reliable and consistent films compared with the earlier work with unsorted nanotubes. A result of this improved deposition is significantly higher currents, including a much higher 'off' current, possibly masking any field effect induced by the gate. To counteract this problem and to attempt to reduce any remaining metallic percolation through the network (noted by others as an undesirable feature for successful FET fabrication [11]) just 2 LB layers were transferred, compared with 5 for the unsorted SWCNT devices. Despite this, the currents passing through the device were significantly higher by a factor of approximately 30.

9.6 Conclusions

Some exploratory work into the use of LB films of SWCNT as the active layer in field effect transistors has been presented in this chapter. Leakage dominated devices based on silicon with a thin (100 nm) silicon dioxide dielectric layer. This was attributed to pin-hole defects in the oxide layer. Patterned thick oxide (300 nm) dielectric layers reduced the leakage of devices, but virtually no field effect was observed. The most successful devices were based on a PMMA dielectric, showing a field dependent source-drain current, however high off currents dominated the devices and only small modulation in current was achieved with no saturation being reached. The on/off ratio was approximately 8, and the field effect mobility was $\sim 0.3\,\mathrm{cm}^2/\mathrm{Vs}$ for the most successful device.

References

[1] Y. Yun, C. Pearson, and M. C. Petty, "Pentacene thin film transistors with a poly(methyl methacrylate) gate dielectric: optimization of device performance," *J. Appl. Phys.*, vol. 105, p. 034508, 2009.

[2] M. C. LeMieux, M. Roberts, S. Barman, Y. W. Jin, J. M. Kim, and Z. Bao, "Self-sorted, aligned nanotube networks for thin-film transistors," *Science*, vol. 321, pp. 101–104, 2008.

[3] H. Wang, J. Luo, A. Robertson, Y. Ito, W. Yan, V. Lang, M. Zaka, F. Sch´affel, M. H. R´ummeli, G. A. D. Briggs, and J. H. Warner, "High-performance field effect transistors from solution processed carbon nanotubes," *ACS Nano.*, vol. 4, no. 11, pp. 6659–6664, 2010.

[4] S. Han, J. Chang, A. D. Franklin, A. A. Bol, R. Loesing, D. Guo, G. S. Tulevski, W. Haensch, and Z. Chen, "Wafer scale fabrication of carbon nanotube FETs with embedded poly-gates," *IEEE*, 2010.

[5] S. J. Wind, J. Appenzeller, R. Martel, V. Derycke, and P. Avouris, "Vertical scaling of carbon nanotube field-effect transistors using top gate electrodes," *Appl. Phys. Lett.*, vol. 80, no. 20, pp. 3817–3819, 2002.

[6] N. B. Ukah, J. Granstrom, R. R. S. Gari, G. M. King, and S. Guha, "Low-operating voltage and stable organic field-effect transistors with poly (methyl methacrylate) gate dielectric solution deposited from a high dipole moment solvent," *Appl. Phys. Lett.*, vol. 99, no. 24, p. 243302, 2011.

[7] T. Fukao, S. Nakamura, H. Kataura, and M. Shiraishi, "Solution-processed single-walled carbon nanotube transistors with high mobility and large on/off ratio," *Japanese Journal of Applied Physics*, vol. 45, no. 8A, pp. 6524–6527, 2006.

[8] A. Lin, N. Patil, K. Ryu, A. Badmaev, L. G. D. Arco, C. Zhou, S. Mitra, and H.-S. P. Wong, "Threshold voltage and on-off ratio tuning for multiple-tube carbon nanotubes FETs," *IEEE Trans. on Nanotech.*, vol. 8, no. 1, pp. 4–9, 2009.

[9] M. Engel, J. P. Small, M. Steiner, M. Freitag, A. A. Green, M. C. Hersam, and P. Avouris, "Thin film nanotube transistors based on self-assembled, aligned, semiconducting carbon nanotube arrays," *ACS Nano*, vol. 2, no. 12, pp. 2445–2452, 2008.

[10] C. Wang, J. Zhang, K. Ryu, A. Badmaev, L. G. D. Arco, and C. Zhou, "Wafer-scale fabrication of separated carbon nanotube thin-film transistors for display applications," *Nano Lett.*, vol. 9, no. 12, pp. 4285–4291, 2009.

[11] H. E. Unalan, G. Fanchini, A. Kanwal, A. D. Pasquier, and M. Chhowalla, "Design criteria for transparent single-wall carbon nanotube thin-film transistors," *Nano Lett.*, vol. 6, no. 4, pp. 677–682, 2006.

Chapter 10

Conclusions and Suggestions for Further Work

10.1 Conclusions

The aim of this thesis was to explore the Langmuir-Blodgett technique as a method of forming thin networks of single-walled carbon nanotubes.

Carbon nanotubes are seen as an attractive new material for applications in modern electronics due to their unique electrical, optical and mechanical properties. Before nanotubes can be used in commercial applications, a reliable method of forming thin films must first be developed. Langmuir-Blodgett deposition was chosen as a suitable solution based processing method due to the low temperatures involved and the ability to precisely control the thickness of layers. Despite several reports showing successful LB deposition with SWCNTs, these all included the use of surfactants, polymers or fatty acids to aid in floating layer formation. This work primarily explored pure nanotube suspensions in organic solvents. By not including additional materials, it was hoped that the remarkable electronic properties of the nanotubes would be preserved following deposition.

Various parameters and their effect on LB deposition were investigated during experimentation. First, the effect of annealing unsorted nanotubes during purification made large changes in the structure of floating layer versus area isotherms. Annealed nanotubes showed significantly more structure in the isotherms with clearer transitions between phases on the water and improved stability at higher surface pressures. Improved deposition was also observed with the annealed variants. Both of these observations were attributed to the addition of carboxylic (COOH) groups to the surface of the nanotubes during the annealing process. The introduction of such a polar group aids in formation of the LB layers. Similarly, when unsorted nanotubes were oxidised using HNO_3, improved isotherms were also observed. Again, this was thought to be due to the presence of acid groups on the nanotube surface. Unsorted nanotubes when deposited in the presence of an AC electric field showed preferential deposition to the electrodes.

Secondly, the LB experimental work moved to using sorted metallic and semiconducting nanotubes. By varying the amount of starting material, different regions of the isotherm were observed. By piecing together these regions a generic isotherm was obtained for SWCNT on a pure water subphase showing the typical regions associated with Langmuir isotherms; gaseous, expanded and condensed regions. Transfer to solid substrates proved challenging from a pure water subphase despite the structured isotherms. Methanol was added to the water subphase in low concentrations (5 %) to reduce the surface tension of the water subphase. This appeared to aid in floating layer formation, with the isotherms showing sharper phase transitions. Transfer for SWCNT-M remained challenging however, transfer for SWCNT-S was improved.

The morphology and optical properties of LB networks of SWCNTs were explored. Microscopy evidence (AFM, SEM and TEM) showed relatively sparse networks of interconnected bundles when only a few LB layers were transferred. AFM and ellipsometry data suggested an average layer thickness of around 2.5 nm for SWCNT-

S and SWCNT-M material. The actual build up of layers is better thought of as an increase in density (particularly at small numbers of layers) rather than each layer being deposited as a continuous film. A nonlinear increase in optical absorption from 18 to 198 layers agreed with this hypothesis. As gaps were filled in between nanotube bundles, scattering effects became less dominant, reducing the rate of increase in absorption with network thickness. In-plane DC electrical measurements showed a strong correlation to the direction of dipping with overall conductivity. The nanotubes showed preferential alignment along the direction of dipping.

The observation of a surface residue in the sorted semiconducting and metallic nanotubes led to an additional annealing step following LB deposition. This improved the electrical contact to electrodes, by many orders of magnitude in the case of the semiconducting nanotubes. Gold and palladium produced the most reliable Ohmic contacts to the nanotube networks and were used to take the majority of electrical measurements. It was suggested that Poole-Frenkel conduction was the dominant conduction mechanism for thin networks of semiconducting nanotubes at high electric fields ($>10 \times 10^6$ V/m). Thin networks of metallic nanotubes exhibited a typical temperature dependence of conductivity expected for that of a metallic material.

The final chapter, exploring the use of LB networks of SWCNT as the active layer in thin film transistors, yielded interesting results on longer channel length (50 µm) devices. However, short channel length devices (<1 µm) suffered from high leakage due to oxide defects introduced during the fabrication process, making meaningful device characterisation difficult. The best device, a long channel organic insulator based structure with unsorted SWCNT-U as the semiconducting layer gave an on/off ratio of around 8 and a field effect mobility of $\sim 0.3\,\mathrm{cm}^2/\mathrm{Vs}$.

10.2 Suggestions for Further Work

10.2.1 Alignment of Nanotubes using Electric Fields during Langmuir-Blodgett Deposition

Section 6.2.3 showed that nanotubes were attracted to electrodes when subjected to an AC electric field during deposition. Through further experiments, looking at the effect of frequency and amplitude as well as improving the electrode design it is possible that electric fields could further improve the alignment of nanotubes during LB deposition.

10.2.2 Growth of Bio-Material on Nanotube Networks

Thin networks of carbon nanotubes deposited by the Langmuir-Blodgett technique offer an opportunity to study the effect (if any) the growth of cells have when in contact with this relatively new material. The very thin nature of the networks makes electron microscope imaging easy, and should also make distinguishing the biological material from the nanotubes straightforward. The density of the networks as well as overall thickness can be controlled so the effect of just a few bundles can be observed as well as a multiple layer continuous film. Some LB SWCNT networks have been prepared and initial cell growth experiments have been performed.

10.2.3 Novel Computation

Alternatives to conventional digital electronics are of great interest with the expectation that the limits of miniaturisation in digital circuitry could soon be reached. Carbon nanotubes deposited on micro-electrode arrays could then be

trained using various electrical stimuli applied using an evolutionary algorithm to generate the desired response from a circuit. This could be an approximation of a mathematical function or could replicate the behaviour of conventional digital circuits (AND, OR, NOT gates etc). By training a disordered material to behave in a set way it is hoped that a computational device could be made without the need to reproduce individual components. The interesting electrical properties studied on Langmuir-Blodgett networks of single walled carbon nanotubes in this thesis suggest they would make a good starting point in researching these novel computational properties.

This work is being undertaken on an EU funded project, NAnoSCale Engineering for Novel Computation using Evolution (NASCENCE).

Publications

- **M. K. Massey**, C. Pearson, D. A. Zeze, B. Mendis, and M. C. Petty, "The electrical and optical properties of orientated Langmuir-Blodgett films of single-walled carbon nanotubes," *Carbon*, vol. 49, pp. 2424–2430, 2011.

- **M. K. Massey**, M. C. Rosamond, C. Pearson, D. A. Zeze, and M. C. Petty, "Electrical behavior of Langmuir-Blodgett networks of sorted metallic and semiconducting single-walled carbon nanotubes," *Langmuir*, vol. 28, no. 43, pp. 15385–15391, 2012.

Conferences Attended

- **SET For Britain**, "Carbon Nanotube Thin Film Conductors" (Poster) *London*, March 2010

- **ICOE 2010**, "Carbon Nanotube Thin Film Conductors" (Poster) *Paris*, June 2010

- **ECOF 12**, "Langmuir-Blodgett Films of Carbon Nanotubes" (Poster) *Sheffield*, July 2011

- **MRS Spring Meeting**, "Conductivity and Field Effect in Langmuir-Blodgett Networks of Single-Walled Carbon Nanotubes" (Poster) *San Francisco*, April 2012